NONLINEAR ULTRASOUND FOR RADIATION DAMAGE DETECTION

A Thesis
Presented to
The Academic Faculty

by

Kathryn H. Matlack

In Partial Fulfillment
of the Requirements for the Degree
Doctor of Philosophy in the
G.W. Woodruff School of Mechanical Engineering

Georgia Institute of Technology
May 2014

NONLINEAR ULTRASOUND FOR RADIATION DAMAGE DETECTION

Approved by:

Professor Laurence J. Jacobs, Advisor
G.W. Woodruff School of Mechanical Engineering
Georgia Institute of Technology

Professor David L. McDowell
G.W. Woodruff School of Mechanical Engineering
Georgia Institute of Technology

Professor Jianmin Qu
Department of Civil and Environmental Engineering
Northwestern University

Professor Chaitanya Deo
G.W. Woodruff School of Mechanical Engineering
Georgia Institute of Technology

Dr. Jin-Yeon Kim
School of Civil and Environmental Engineering
Georgia Institute of Technology

Dr. James J. Wall
Nuclear Sector
Electric Power Research Institute

Date Approved: March 26, 2014

ACKNOWLEDGEMENTS

Throughout my Ph.D., I have been lucky enough to have the support of three amazing advisors – Prof. Laurence Jacobs, Prof. Jianmin Qu, and Dr. Jin-Yeon Kim – and one adoptive advisor, Dr. James Wall. While this many advisors made some paper revisions a bit complicated, I really cannot express to you how much I appreciate all of your support and guidance over the past few years, and the success of my Ph.D. could not have happened without all of you.

Larry Jacobs – my sincerest thanks to you for all of your support, advice, and for making my PhD as wonderful of an experience as it could be. Thank you for always helping me to see the bigger picture, caring for my well-being, and giving me confidence in my work and myself. I hope to give my own future students the same support and guidance. Thank you to Jianmin Qu for your guidance throughout my PhD, particularly with your advice to open a new area of research with my thesis, and all your help with the modelling portions of this thesis. Though we did not work in close proximity, your advice and support was nonetheless incredibly valuable and greatly appreciated. Thank you to Jin-Yeon Kim for your invaluable advice and help with experiments, enlightening discussions, and with anything and everything else around the lab. I learned so much from you during my Ph.D., and I would not be the diligent researcher I am today without your guidance. Thank you to Joe Wall for getting me connected to the right people at the right times to make the experiments in this thesis happen, and for your advice tying this work to industry needs. Thanks for being an entertaining travel partner, and for not getting us into a car accident in Dresden.

I would like to thank Prof. David McDowell and Prof. Chaitanya Deo for serving

on my Ph.D. committee. Your time and input with regards to this thesis (particularly Prof. Deo's words of advice getting me started in the field of radiation damage, and Prof. McDowell's guidance with materials modelling) is greatly appreciated.

The GW Woodruff School of ME at Georgia Tech has truly provided a collaborative and supportive environment for me to develop as a researcher and person. I would especially like to thank Srinivas Garimella for all his advice getting and keeping me on the right track, Christine Valle for her honest and open mentorship, Preet Singh for his help with the stress corrosion cracking project, and all the other faculty who have kept their doors open to me over the years.

I would like to thank the following funding sources for their financial support of this research - the National Science Foundation Graduate Research Fellowship Program, the Department of Engery Office of Nuclear Energy's Nuclear Energy University Programs, and the Electric Power Research Institute. I would also like to thank the PEO Scholars Award foundation, as well as the Innovations in Fuel Cycle Research Awards Program for their financial support.

I would like to thank the staff at HZDR and ORNL for running the experiments on the irradiated samples. In particular, thank you to Hans-Werner Vierhig for setting up these experiments at HZDR, and to Mikhail Sokolov for his efforts setting up the experiments at ORNL.

It has been a fantastic experience working with all of the students in our lab over the past few years. Thank you to the many "generations of Germans" and all the other students who have made the lab an enjoyable place to work - from doughnut Wednesdays, to QNDE trips, to nights at Antico, all of you have been such a pleasure to get to know and work with. I would in particular like to thank Sebastian Thiele for his work and insightful conversations pertaining to the surrogate samples, as well as Harrison Bradley for his work with experiments for the surrogate samples. Thank you to the current members of the lab (Gun Kim, David Torello, Harrison Bradley,

Anne Romer, Daniel Marino, Florian Morlock, Mehdi Rashidi, Maggie Smith, and Chiwon In), for putting up with me while writing this thesis.

Thank you to all my friends here at GT, for keeping me sane and happy through every step of this journey. Thanks to David Torello for being there for me through it all. Thank you to Huy Tran for being my constant support, for your patience and understanding throughout this thesis, and always making me smile. Last but absolutely not least, I would like to thank my family, the Matlack clan - Mom, Dad, Megan, David, and Joseph - for your endless love and support. You are the ones who got me to where I am today, and have instilled in me that I can accomplish anything I set my mind to. Thank you for always believing in me, and supporting me in all of my crazy dreams and endeavors.

TABLE OF CONTENTS

ACKNOWLEDGEMENTS . . . . . **iii**

LIST OF TABLES . . . . . **x**

LIST OF FIGURES . . . . . **xi**

LIST OF SYMBOLS AND ABBREVIATIONS . . . . . **xv**

SUMMARY . . . . . **xx**

I INTRODUCTION **1**

1.1 Motivation and Objectives 1

1.2 Structure of Thesis 4

II REVIEW OF SECOND HARMONIC GENERATION **6**

2.1 Overview 6

2.2 Derivation of the Nonlinearity Parameter 7

2.2.1 Attenuation Effects 8

2.3 Microstructural Contributions to β 9

2.3.1 Dislocation pinning 10

2.3.2 Precipitate-pinned dislocations 13

2.3.3 Vacancy contribution 15

2.4 Current Detection Capabilities 16

2.4.1 Fatigue- and dislocation-based monitoring 17

2.4.2 Thermal Aging Monitoring 18

2.5 Summary 21

III RADIATION DAMAGE IN RPV STEEL **22**

3.1 Chapter Overview 22

3.2 Background: Nuclear Reactors 22

3.2.1 Current NDE and surveillance methods 24

3.2.2 Planned life extension 25

3.3 Radiation-Enhanced Diffusion . . . 25
3.4 Microstructural Changes . . . 26
3.4.1 Copper-Rich Precipitates . . . 28
3.4.2 Matrix Features . . . 29
3.4.3 Manganese-Nickel Precipitates . . . 30
3.4.4 Phosphorous Phases and Segregation . . . 30
3.5 Macroscopic Damage . . . 31
3.5.1 Model for Yield Stress Increase . . . 33
3.6 Post-Irradiation Annealing . . . 34
3.7 Re-Irradiation After PIA . . . 36
3.8 Proposed NDE Techniques for Radiation Damage . . . 37
3.9 Summary . . . 39
IV ANALYTICAL MODEL DEVELOPMENT . . . 42
4.1 Overview . . . 42
4.2 Interstitial-type Dislocation Loops . . . 42
4.3 Distribution of Precipitate Size . . . 46
4.3.1 Model Development . . . 46
4.3.2 Numerical Study of Precipitate Distribution . . . 48
4.4 Intersection of Dislocation Pinning Models . . . 49
4.5 Dislocation-interstitial row interactions . . . 51
4.5.1 Derivation of Displacement . . . 52
4.5.2 Lattice Contribution to the Second Harmonic Wave . . . 58
4.5.3 Solution for Second Harmonic Wave Amplitude . . . 58
4.5.4 Solution for the Acoustic Nonlinearity Parameter . . . 60
4.6 Model Comparisons . . . 61
4.6.1 Dislocation-interstitial row versus pinned dislocations . . . 61
4.6.2 Dislocation-interstitial row versus precipitate-pinned dislocations . . . 63
4.6.3 Vacancies versus precipitates . . . 66

4.6.4 Two-Feature Pinning Model 67
4.7 Summary 69
V EXPERIMENTAL METHODS 70
5.1 Overview 70
5.1.1 Longitudinal Waves 70
5.1.2 Guided Waves 72
5.2 Longitudinal Measurements 73
5.2.1 Experimental Set-up 73
5.2.2 Measurement Fixture 75
5.2.3 Post-Processing 78
5.3 Air-Coupled Detection: Rayleigh Wave Measurements 81
5.4 Complementary measurements 83
5.4.1 Vickers Microhardness 83
5.4.2 Thermo-electric Power 84
VI SURROGATE MATERIAL 86
6.1 Overview and Purpose 86
6.2 17-4PH Stainless Steel 87
6.2.1 Background 87
6.2.2 17-4PH Specimen Preparation 89
6.2.3 Material Characterizations 90
6.2.4 Nonlinear Ultrasonic Measurement Results 95
6.3 Discussions 99
6.3.1 Differences between Rayleigh and longitudinal measurements 99
6.3.2 Expected Trends with Nonlinearity 100
6.3.3 Interpretation of Rayleigh wave results 101
6.4 Summary 102
VII EXPERIMENTAL RESULTS: IRRADIATED MATERIAL . . . 103
7.1 Overview 103

7.2 Material Samples . . . 103
7.3 Nonlinear Ultrasonic Results . . . 105
7.3.1 Determination of β_0 for JRQ Heat 1 . . . 111
7.4 Previous Material Characterizations . . . 113
7.5 Neutron Diffraction Measurements . . . 115
7.5.1 Background . . . 115
7.5.2 NPDF Experiments and Results . . . 116
7.6 Summary . . . 118
VIII DISCUSSIONS . . . 119
8.1 Precipitate Contribution . . . 119
8.2 Effects of Neutron Flux . . . 122
8.3 Effects of Composition . . . 123
8.4 Effects of Irradiation Temperature . . . 124
8.5 Effects of Phosphorous in JRQ on $\Delta\beta$ . . . 125
8.6 Post-irradiation Annealing . . . 127
8.7 Re-irradiation Effects . . . 128
8.8 Implications of Surrogate Material on Irradiation Detection . . . 130
8.9 Implications on Monitoring Radiation-Induced Embrittlement . . . 132
IX CONCLUSIONS AND FUTURE OUTLOOK . . . 135
9.1 Summary of Results . . . 135
9.2 Recommendations for Future Work . . . 137
9.3 Significance and Impact . . . 139
APPENDIX A — DIFFRACTION CORRECTION . . . 141
APPENDIX B — SOURCES OF MEASUREMENT VARIATION 144
APPENDIX C — LINEAR ULTRASONIC MEASUREMENTS . 149
REFERENCES . . . 154

LIST OF TABLES

1 Chemical composition of as-received 17-4PH stainless steel. 89

2 Sample designations and aging conditions for 17-4PH Charpy samples. 91

3 Normalized measured β for gas/water quenched and air-cooled samples, using Rayleigh waves. 98

4 Change in β measured in 17-4PH Charpy samples over thermal aging, relative to as-is state. 98

5 Chemical composition (wt.%) of JRQ and JFL materials. 104

6 Conditions for samples undergoing irradiation, post-irradiation annealing, re-irradiation, and re-annealing. Neutron fluence and flux levels are all in terms of neutron energies of E > 1 MeV. 106

7 Change in β due to increased neutron fluence and annealing of JRQ for $T_i = 290°C$. 107

8 Change in β/β_0 due to increased neutron fluence of JRQ and JFL for $T_i = 255°C$. 108

9 Measured β in all irradiated sample sets. 112

10 Measured material properties of samples for NLU, based on previous material characterizations. Neutron fluence levels are in terms of neutron energies of E > 1 MeV (from Zurbuchen et al. 2009, Nanstad et. al 2004, and Nanstad et al. 2005). 114

11 Results of previous SANS measurements of precipitate volume fraction and average radius, and calculated number densities, for JRQ and JFL irradiated at 255°C (from Ulbricht et al. 2005). 115

12 Results of previous APT measurements of *estimated* precipitate number densities and average radius, for some of the JRQ samples irradiated at 290°C (from Miller et al. 2006). 115

13 Diffraction correction (linear and nonlinear diffraction) for JRQ $T_i = 290°C$ samples. 142

14 Diffraction correction (linear and nonlinear diffraction) for JRQ and JFL $T_i = 255°C$ samples. 143

LIST OF FIGURES

1 (a) Diagram showing geometry of bowed dislocation segment of length $2L$ between two pinning points and under an applied shear stress τ, in terms of radius of curvature r and angle θ. (b) Diagram showing movement of dislocation segment with superimposed ultrasonic stress on top of initial stress τ. 11

2 (a) Diagram of precipitate with radius r_p embedded in a matrix with natural radius of r_a, and (b) diagram of a dislocation bending around a distribution of precipitates, with spacing of L. 13

3 Diagram of a pressurized water reactor, illustrating reactor pressure vessel on the left-hand side. 23

4 Pictorial representation of the change in Charpy-V transition temperature (ΔT_{41}) and upper shelf energy (ΔUSE) of irradiated RPV steel compared to the unirradiated state. 32

5 Inclusion embedded in a matrix. 43

6 Distribution of precipitates assuming a Gaussian distribution and using volume fraction and average radius values (from Ulbricht et. al 2005). 48

7 Change in β due to precipitate-pinned dislocations, calculated using average radius values and using a distribution of precipitate sizes. . . 49

8 Diagrams of row of interstitial atoms at edge of half–plane of edge dislocation, illustrating movement of the dislocation along the slip plane given some applied shear stress (based off of diagram on pg. 209 in Bacon and Hull, *Introduction to Dislocations*). 51

9 (a) Diagram in x-y plane of row of interstitial atoms at edge of half–plane of edge dislocation, and (b) diagram in x-y plane showing dislocation movement trapped by interstitial row. 52

10 Geometry of dislocation motion along slip plane in a volume of a crystal. 55

11 Relative strength of β_{di} and β_{ppd} over increasing number density of precipitates 65

12 Relative strength of β_{di} and β_{ppd} over increasing values of ζ, the fraction of trapped dislocations. 65

13 Two-feature pinning model: diagram of dislocation pinning by two different microstructural features, precipitates and vacancies. 67

14 Schematics of experimental set-ups for longitudinal SHG measurements of the acoustic nonlinearity parameter (from Matlack et al. *JAP* 2012, and Matlack et al. *JNM* 2014). 74

15 (a) Representative time signal as measured by the receiving transducer in the longitudinal measurements, and (b) the corresponding Hann-windows time signal. Data is taken from one of the irradiated-annealed-re-irradiated samples (see Chapter 7). 75

16 (a) Representative FFT of time signal shown in Figure 15, and (b) an example of the measurement data for first and second harmonic amplitudes, where the slope of the linear fit of the data is the relative acoustic nonlinearity parameter β'. 76

17 (a) Schematic and (b) photo of fixture designed for longitudinal wave measurements of the acoustic nonlinearity parameter. 77

18 Linear diffraction correction for increasing wave propagation distance for three separate frequencies. 80

19 Linear diffraction correction for increasing wave propagation distances corresponding to sample thickness of the measured Charpy irradiated RPV steel samples at $T_i = 290°C$ (left) and $T_i = 255°C$ (right), for three separate frequencies. 80

20 Nonlinear diffraction correction for increasing wave propagation distance for three separate excitation frequencies (first harmonic frequencies are labelled in the plot). 81

21 Nonlinear diffraction correction for increasing wave propagation distances corresponding to sample thickness of the measured Charpy irradiated RPV steel samples at (a) $T_i = 290°C$ and (b) $T_i = 255°C$, for three separate excitation (first harmonic) frequencies. 82

22 Schematic of experimental set-up for Rayleigh wave measurements of β using wedge generation and an air-coupled receiver. 83

23 Representative measurement (average of three separate measurements) of β using Rayleigh waves and air-coupled detection – the slope of the linear fit between the measured ratio A_2/A_1^2 over propagation distance x is proportional to β. 84

24 Measured Vickers hardness for 17-4PH Charpy and bar heat treated samples, for gas quenched and air cooled initial state. Note that "GQ" is used for water quenched samples in bar form, since microstructure due to gas vs. water quench is expected to be comparable. 91

25 Measured thermo-electric power (TEP) for 17-4PH Charpy and bar heat treated samples, in the gas/water quenched and air cooled initial state. Note that "GQ" is used for water quenched samples in bar form, since microstructure due to gas vs. water quench is expected to be comparable. 92

26 TEM image for 17-4PH as-received (air cooled condition). No evidence of precipitation can be seen, and grains contain a very high dislocation density, as indicated by the darker regions on the image. 93

27 TEM images for 17-4PH sample aged at 400°C for 1 hour (AC-1). Arrows indicate some isolated precipitates in the image on the right. . 94

28 TEM image for 17-4PH sample aged at 400°C for 6 hours (AC-6). The contrast indicates there is still a high density of dislocations, which is likely masking the ability to image the precipitates. 94

29 APT atom maps of Cu, Cr, and Ni (from top image to bottom) from sample 17-4PH AC-6. 96

30 Normalized measured β with Rayleigh waves and air-coupled detection for 17-4PH thermally aged material at 400°C in (a) air cooled state, and (b) water quenched compared to air cooled state. Each data point represents an average over three separate measurements. 97

31 Measurements of β using longitudinal waves for (a) gas quenched and (b) air cooled thermally aged 17-4PH Charpy samples. 97

32 Normalized measured β with Rayleigh waves plotted against $1/H_v^{2/3}$, after Equation 123. 102

33 Results of measured β for irradiated, annealed, re-irradiated, and re-annealed JRQ steel, over increasing neutron fluence at $T_i = 290$°C. and showing effects of annealing. Data points represent measurements on the first Charpy half at location 1 (◆) and location 2 (▲), and on the second Charpy half at location 1 (■) and location 2 (✕). 107

34 Dependence of β on neutron fluence for JRQ and JFL steel irradiated at $T_i = 255$°C. 108

35 Influence of increasing neutron fluence (E > 1 MeV) on β , for JRQ and JFL at $T_i = 255$°C and 290°C. Each dataset is normalized to the measured β in the unirradiated state, β_0. JRQ samples irradiated at 290°C to 0.5×10^{19} and 1.7×10^{19} n/cm^2 received an intermediate anneal at 50% target fluence. 110

36 Representative time signal of a 3.3 MHz propagated wave through the 5mm-thick unirradiated JRQ heat 1 sample. The red points represent the bounds for the section of the signal extracted for the FFT. 113

37 (a) Williamson-Hall plot for medium and high dose JRQ samples and silicon standard, and (b) all samples. Labels indicate hkl lattice planes. 117

38 Predicted trend of $\Delta\beta$ (normalized by β_{max}) as a function of number density of precipitates, normalized by N_{cr}, assuming trend is dominated by precipitate-pinned dislocations (i.e. second term in Equation 61). . 121

39 Predicted $\Delta\beta$ using SANS inputs of precipitate volume fractions and average radius for JRQ and JFL samples irradiated at 255°C, using only precipitate pinned dislocation model. $\Delta\beta$ is normalized by the predicted β for JRQ irradiated to 0.7×10^{19} n/cm^2, and note this low neutron fluence sample (and the corresponding one of JFL material) was not available for NLU measurements. 122

40 Dependence of β on annealed microstructure for unirradiated JRQ and irradiated JRQ ($T_i = 290$°C). 128

41 Laser confocal microscope images of (a) the as-is Charpy sample surface, and (b) polished surface to 150 grit polish paper. 145

42 Laser confocal microscope images of the (a) polished surface to 240 grit polish paper, and (b) polished surface to 400 grit polish paper. . 146

43 (a) Dependence of β on surface roughness for JRQ and JFL unirradiated samples, and (b) normalized β for unirradiated samples (polished to 600 grit) and after polish to 2000 grit. 146

44 Example time signal of the two successive reflections used for the longitudinal wave velocity measurements. 151

45 Measurements of attenuation coefficient over frequency range for (a) JRQ, and (b) JFL, for unirradiated and irradiated samples. 152

46 Longitudinal wave velocity measured in JRQ and JFL unirradiated and irradiated samples. 152

LIST OF SYMBOLS AND ABBREVIATIONS

α	Fraction of precipitate–pinned dislocation segments
α_1	Attenuation coefficient of 1st harmonic wave
α_2	Attenuation coefficient of 2nd harmonic wave
β	Acoustic nonlinearity parameter
β'	Relative acoustic nonlinearity parameter
β_{di}	Nonlinearity due to dislocation-interstitial interactions
β_{pd}	Nonlinearity due to pinned dislocations
β_{ppd}	Nonlinearity due to precipitate-pinned dislocations
β_v	Nonlinearity due to vacancy-pinned dislocations
δ	Misfit parameter
γ	Plastic strain
κ	Wavenumber
Λ	Dislocation density
Ω	Conversion factor from shear-longitudinal strain
ω	Radial frequency
Ω_v	Volume per atom of interstitials segregated to dislocations
ρ	Density
σ	Longitudinal stress

σ_p	Local misfit stress due to a precipitate
σ_v	Local misfit stress due to a vacancy
σ_y	Yield stress
τ	Shear stress
ζ	Fraction of dislocations trapped by interstitial rows
A_1	First harmonic wave amplitude
A_2	Second harmonic wave amplitude
B	Precipitate configurational entropy
b	Burgers vector
B_p	Bulk modulus of precipitate
D	Diffraction correction
f	Frequency
f_v	Volume fraction
G	Shear modulus
H_v	Vickers hardness
L	Dislocation loop length
N	Number density of defect
$N_{cr,2}$	Critical number density of precipitates for $\beta_{di} = \beta_{ppd}$
N_{cr}	Critical number density of precipitates for all dislocations to be pinned by precipitates

R	Resolving shear factor
r	Radius of defect
T_i	Irradiation temperature
u	Particle displacement
x	Material coordinate
AC	Air-cooled
APT	Atom probe tomography
BN	Barkenhousen noise
BWR	Boiling water reactor
CRP	Copper-rich precipitate
DBTT	Ductile to brittle transition temperature
dpa	Displacements per atom
EDM	Electrical discharge machining
FEG-TEM	Field emission gun transmission electron microscopy
FFT	Fast Fourier transform
FWHM	Full-width at half maximum
GQ	Gas quenched
h	Hours
I	Irradiated
IA	Irradiated, annealed

IAR	Irradiated, annealed, re-irradiated
IARA	Irradiated, annealed, re-irradiated, annealed
JFL	ASTM A508 Class 1 reactor pressure vessel material
JRQ	ASTM A533 Class 1 reactor pressure vessel material
MNP	Manganese-nickel precipitate
NDE	Nondestructive evaluation
NLU	Nonlinear ultrasound
NPDF	Neutron powder diffractometer
PAS	Positron annihilation spectroscopy
PH	Precipitate hardened
PIA	Post-irradiation annealing
PTS	Pressurized thermal shock
PWR	Pressurized water reactor
RED	Radiation-enhanced diffusion
RPV	Reactor pressure vessel
SANS	Small-angle neutron scattering
SHG	Second harmonic generation
SMF	Stable matrix feature
TEM	Transmission electron microscopy
TEP	Thermo-electric power

U	Unirradiated
UMD	Unstable matrix defect
WQ	Water quenched

SUMMARY

Radiation damage occurs in reactor pressure vessel (RPV) steel, causing microstructural changes such as point defect clusters, interstitial loops, vacancy-solute clusters, and precipitates, that cause material embrittlement. Radiation damage is a crucial concern in the nuclear industry since many nuclear plants throughout the US are entering the first period of life extension and older plants are currently undergoing assessment of technical basis to operate beyond 60 years. The result of extended operation is that the RPV and other components will be exposed to higher levels of neutron radiation than they were originally designed to withstand. There is currently no nondestructive evaluation technique that can unambiguously assess the amount of radiation damage in RPV steels.

Nonlinear ultrasound (NLU) is a nondestructive evaluation technique that is sensitive to microstructural features such as dislocations, precipitates, and their interactions in metallic materials. The physical effect monitored by NLU is the generation of higher harmonic frequencies in an initially monochromatic ultrasonic wave, arising from the interaction of the ultrasonic wave with microstructural features. This effect is quantified with the measurable acoustic nonlinearity parameter, β. In this work, nonlinear ultrasound is used to characterize radiation damage in reactor pressure vessel steels over a range of fluence levels, irradiation temperatures, and material composition. Experimental results are presented and interpreted with newly developed analytical models that combine different irradiation-induced microstructural contributions to the acoustic nonlinearity parameter.

CHAPTER I

INTRODUCTION

1.1 Motivation and Objectives

Nonlinear ultrasonic methods have the powerful ability to characterize microstructural features in materials. Compared to more conventional linear ultrasonic methods that can detect cracks or features on the order of the wavelength of the ultrasonic wave, nonlinear methods are sensitive to microstructural features that are orders of magnitude smaller than the wavelength. These methods were first reported on back in the 1960s, with a series of papers by Breazeale, Thompson, and Ford [1, 2], and another series by Hikata, Chick, Elbaum, and Sewell [3, 4]. These methods have received significant focus and attention in the literature in recent decades, as the reliability and integrity of structural components becomes increasingly important to ensure safe operation of critical structures in, for example, the energy, transportation, and aviation industry.

A variety of nonlinear ultrasonic techniques have been explored throughout the literature to monitor changes in material properties before macroscopic cracking and damage. The nonlinear ultrasonic technique of second harmonic generation is one of the most well-known ultrasonic techniques with the ability to monitor microstructural changes in metallic materials. A major advantage is its relatively simple instrumentation requirement. The physical mechanism of this is as follows: as a sinusoidal ultrasonic wave propagates through a material, the interaction of this wave with microstructural features generates a second harmonic wave. This effect is quantified with the measured acoustic nonlinearity parameter, β. In this work, the second harmonic generation technique is used to monitor radiation damage in low-alloy steels

(steels containing up to only a few percent of alloying elements), to investigate the feasibility of using this nondestructive evaluation technique to address the pressing issue of aging structural components in nuclear power plants.

As a near-zero carbon emission energy source, nuclear power is and will continue to be an important part of the energy portfolio in the US. Many nuclear plants throughout the US are entering the first period of life extension and older plants are currently undergoing assessment of technical basis to operate beyond 60 years. The result of extended operation is that the RPV and other components will be exposed to higher levels of neutron radiation than they were originally designed to withstand – since nuclear reactors were intended for only 40 years of operation, these structures will be exposed to the radioactive environment for a longer time. So, radiation damage in the reactor pressure vessel (RPV) is a crucial current concern in the nuclear industry. Radiation damage produces microstructural features such as point defect clusters, changes in dislocation densities, and precipitates that cause embrittlement and a decrease in the ductility of the material. There is currently no nondestructive evaluation technique to unambiguously assess the amount of radiation damage in RPV steels. The development of such a technique would enable the assessment of the integrity of the vessel, allowing operators to determine if reactors can continue to operate safely, and would directly support the nuclear industry Long Term Operation and US Department of Energy Light Water Reactor Sustainability initiatives. This thesis provides evidence of a nondestructive evaluation method that has potential to address these issues.

In this thesis, the nonlinear ultrasonic technique of second harmonic generation is used to characterize radiation damage in reactor pressure vessel steels over a range of fluence levels, irradiation temperatures, and material composition. Experimental results are presented and interpreted with newly developed analytical models that

combine different irradiation-induced microstructural contributions to the nonlinearity parameter. The specific objectives are as follows.

Objective 1: Determine if the nonlinear ultrasonic technique of second harmonic generation is sensitive to radiation-induced microstructural changes in reactor pressure vessel steel material.

To address this objective, nonlinear ultrasonic measurements were made on irradiated RPV steel samples with different levels of neutron fluence, different irradiation temperatures, and different material composition. Specifically, two separate RPV steel materials were investigated at increasing levels of neutron fluence, comparable to neutron fluence levels of an RPV in operation for 40-60 years. Two separate irradiation temperatures were investigated, as well as the effects of post-irradiation annealing and re-irradiation, in terms of the influence on the acoustic nonlinearity parameter β. Results show that the acoustic nonlinearity parameter, β, is dependent on these irradiation parameters (fluence, temperature, material composition), and thus β shows sensitivity to the radiation-induced microstructural changes. A surrogate sample set of thermally aged material, which is known to produce copper precipitates during thermal aging, was used to isolate the precipitate contribution to the acoustic nonlinearity parameter. Measurements of β with both longitudinal and Rayleigh waves were made in these surrogate samples to relate changes in β to precipitate-pinned dislocations.

Objective 2: Investigate the relationship between the acoustic nonlinearity parameter and microstructural changes that take place throughout radiation damage.

To address this objective, models for pinned dislocations, precipitate-pinned dislocations, and vacancy contributions to changes in the magnitude of β were expanded

on and compared to determine relative contributions of these features to changes in β. A preliminary analytical model was developed to investigate how the presence of interstitial loops changes the magnitude of β, and it is shown that even if these features were present in large number density, the influence on β is insignificant compared to current measurement sensitivity. A new analytical model was developed that determines the change in magnitude of β due to dislocations trapped by interstitial rows, which has been reported to occur in radiation damage in RPV steels. It is shown that depending on the precipitate number density, different models dominate the nonlinear response, and different microstructural features are the dominant mechanism of acoustic nonlinearity. Neutron diffraction measurements were made on irradiated RPV steel samples to measure dislocation density. The results for measured dislocation density are inconclusive, since changes in dislocation density are at the resolution limit of the instrumentation.

1.2 Structure of Thesis

This dissertation is organized as follows. The first chapter provides an introduction to the problem of using nonlinear ultrasonic techniques to monitor radiation damage, and provides the main objectives of this work and how they were addressed. Chapter 2 provides a background to the nonlinear ultrasonic method of second harmonic generation, the theoretical background of these measurement techniques and microstructural contributions to acoustic nonlinearity, and a comprehensive summary of current detection capabilities. Chapter 3 focuses on radiation damage in low-alloy steel, in terms of microstructural features and corresponding changes in macroscopic material properties. Chapter 4 describes the analytical models derived in this work, focusing on the effect of microstructural features present in radiation damage on the change in magnitude of the acoustic nonlinearity parameter. Chapter 5 discusses the experimental methods for the nonlinear ultrasonic measurements presented in this

work, in terms of using both longitudinal and Rayleigh waves. Chapter 6 presents experimental and modelling work on the surrogate material that approximates radiation damage with thermal aging. Chapter 7 presents the experimental results on the irradiated material, exploring effects of different irradiation parameters such as neutron fluence, temperature, and material composition. Chapter 8 provides a discussion and interpretation of these results, in terms of previous microstructural characterizations and models for microstructural evolution of irradiated low-alloy steel, and in terms of the analytical models developed in Chapter 4. The final chapter provides a conclusion and summary of the major results and contributions of this dissertation, and provides recommendations for future work in this area.

CHAPTER II

REVIEW OF SECOND HARMONIC GENERATION

2.1 Overview

Nonlinear ultrasonic (NLU) nondestructive evaluation (NDE) methods have the potential to characterize material damage prior to macroscopic damage such as crack initiation. These methods are based on the phenomenon that when a pure sinusoidal ultrasonic wave propagates through a nonlinear medium, higher harmonic wave components are produced, including a second harmonic wave. Metallic materials are weakly nonlinear, whereas granular materials can be highly nonlinear. Physically, there is an energy transfer from the propagating wave (i.e. the first harmonic wave) to the second harmonic wave. This phenomena is referred to as second harmonic generation (SHG), and can be quantified by the acoustic nonlinearity parameter, β. The amplitude of the second harmonic wave, and thus the magnitude of the acoustic nonlinearity parameter, depends on the crystalline structure of the material [5], as well as defect structures present in the material microstructure, e.g. [3,6–8]. For example, dislocations and precipitates produce local atomic strain fields due to their geometric incompatibility with the existing crystal structure. Strain fields are a strong nonlinear function of the geometric parameters and therefore, when perturbed by ultrasonic waves, dislocations and precipitates act as a localized source of nonlinear body forces that generate the higher harmonics in an initially monochromatic ultrasonic signal. This has important implications in the area of nondestructive evaluation of materials and structural components: since SHG techniques can detect microstructural changes, they can detect changes well before macroscopic damage and component failure. This chapter discusses the theory of SHG, how the magnitude of the acoustic

nonlinearity parameter depends on different defect structures in metallic materials, with a focus on relevant defect structures present in irradiated steel material (the reader is referred to Chapter 3 for further details). The chapter concludes with an extensive overview of current NDE applications utilizing NLU and SHG techniques.

2.2 Derivation of the Nonlinearity Parameter

Consider wave propagation through an isotropic medium with a quadratic nonlinearity. The equation of motion, simplified to one-dimension is:

$$\rho \frac{\partial^2 u}{\partial t^2} = \frac{\partial \sigma_{xx}}{\partial x} \tag{1}$$

where ρ is the density, u is the particle displacement, σ_{xx} is the normal stress in the x-direction, x_1 is the material coordinate, and t is time. The constitutive equation for a quadratic nonlinearity is given as

$$\sigma_{xx} = E_1 \left(\frac{\partial u}{\partial x} \right) + \frac{1}{2} E_2 \left(\frac{\partial u}{\partial x} \right)^2 + ... \tag{2}$$

where E_1 and E_2 are the appropriate second- and third-order elastic constants. The nonlinear wave equation can thus be derived as

$$\frac{\partial^2 u}{\partial t^2} = c^2 \left[1 - \beta \frac{\partial u}{\partial x} \right] \frac{\partial^2 u}{\partial x^2} \tag{3}$$

where β is the nonlinearity parameter and is a function of second- and third-order elastic constants of the material. For a material in its virgin state, β is equivalent to:

$$\beta = -\frac{E_2}{E_1} = -\left(\frac{3C_{11} + C_{111}}{\sigma_1 + C_{11}} \right) \tag{4}$$

where C_{11} and C_{111} are the second- and third-order Brugger elastic constants, respectively, written in Voigt notation. The second relation in Equation 4 assumes wave propagation in the (100) direction, and is also an exact solution for isotropic materials. The time harmonic solution to Equation 3, assuming plane wave propagation, has the form:

$$u = A_1 \sin(\kappa x - \omega t) + A_2 \sin(2\kappa x - 2\omega t) + ... \tag{5}$$

where $\omega = 2\pi f$ is the radial frequency of the wave at frequency f, $\kappa = \omega/c$ is the wavenumber of the propagating wave, A_1 is the amplitude of the first harmonic wave, and A_2 is the amplitude of the second harmonic wave, which, in the absence of attenuation, diffraction, scattering, etc. and assuming plane wave propagation, has been shown to be:

$$A_2 = \frac{\beta A_1^2 x \kappa^2}{8} \tag{6}$$

By simply rearranging this equation, the nonlinearity parameter can be expressed in terms of acoustic quantities, i.e.:

$$\beta = \frac{8A_2}{A_1^2 x \kappa^2} \tag{7}$$

When written in this form, β is generally referred to as the acoustic nonlinearity parameter. Thus by measuring the second harmonic wave amplitude, along with the first harmonic amplitude, wavenumber, and propagation distance, one can determine the acoustic nonlinearity parameter, β. This derivation can be expanded to three dimensions [9], and has been derived for Rayleigh waves [10] and Lamb waves [11]. The same general form of A_2 has been shown for Rayleigh waves and Lamb waves, in terms of dependence on propagation distance, wavenumber, and first harmonic wave.

Note that the energy transfer from the first to second harmonic wave in SHG is very small compared to the energy of the propagating first harmonic wave, such that the decrease in A_1 due to the energy transfer is insignificant for small propagation distances. Further, the amplitude A_2 is orders of magnitude smaller than A_1, which will be shown experimentally. All propagation distances considered in this work are small enough such that the energy loss of A_1 is negligible compared to the total energy of the propagating first harmonic wave.

2.2.1 Attenuation Effects

For real materials and finite propagation distances, attenuation (dissipation, scattering, diffraction) will further decrease the amplitudes of the first and second harmonic

waves with increasing propagation distance. The first harmonic wave is known to attenuate by:

$$A_1 = (A_1)_0 \, e^{-\alpha_1 x} \tag{8}$$

where α_1 is the attenuation coefficient at the first harmonic frequency ω_1, and $(A_1)_0$ is the amplitude of the first harmonic wave at $x = 0$. The attenuation dependence of the second harmonic wave can be found by considering that the second harmonic wave will grow with propagation distance due to the nonlinear interaction described above, and will also decrease due to attenuation effects, independent of the cumulative growth effect. Thus, the change in amplitude of the second harmonic wave with propagation distance can be expressed as [12]:

$$\frac{\mathrm{d}A_2}{\mathrm{d}x} = \left(\frac{\mathrm{d}A_2}{\mathrm{d}x}\right)_{SHG} - \left(\frac{\mathrm{d}A_2}{\mathrm{d}x}\right)_{atten} = \frac{1}{8}\beta A_1^2 \kappa^2 - \alpha_2 A_2 \tag{9}$$

where α_2 is the attenuation coefficient at the second harmonic frequency. This first order differential equation can be solved [12] assuming the amplitude of the second harmonic wave is zero at $x = 0$ (i.e. the second harmonic wave is only generated by the nonlinear interaction of the first harmonic wave with the material). The full expression for the second harmonic amplitude including attenuation effects is thus given by [12]:

$$A_2 = \frac{1}{8}\beta\kappa^2 \, (A_1)_0^2 \left[\frac{\exp(-2\alpha_1 x) - \exp(-\alpha_2 x)}{\alpha_2 - 2\alpha_1}\right] \tag{10}$$

So, the expression for the acoustic nonlinearity parameter when attenuation effects are non-negligible, β_{atten}, is given as:

$$\beta_{atten} = \beta \frac{x\,(\alpha_2 - 2\alpha_1)}{1 - \exp\left[-x\,(\alpha_2 - 2\alpha_1)\right]} \tag{11}$$

Note that attenuation effects are negligible when $x\,(\alpha_2 - 2\alpha_1) \ll 1$.

2.3 Microstructural Contributions to β

The parameter β depends on the crystalline structure of the material, and also on localized strain present in the material. This strain arises from microstructural features

such as dislocations and precipitates. This section provides a comprehensive review of different microstructural contributions to the magnitude of the acoustic nonlinearity parameter, which are relevant to radiation damage in RPV steel materials at relevant levels of neutron fluence. Theoretical derivations of contributions of dislocation pinning [3, 12], precipitate-pinned dislocations [7, 12–14], and vacancy contributions will be reviewed [15]. Note that significant work has focused on how dislocation dipoles give rise to a change in acoustic nonlinearity, see e.g. [8], but since these dislocation structures have not at all been shown to form during radiation damage, dislocation dipole contribution to nonlinearity will not be discussed here.

2.3.1 Dislocation pinning

The derivation of the effect of dislocation pinning on the magnitude of the acoustic nonlinearity parameter is based off of work by Hikata and expanded on later by Cantrell [3,12]. The derivation is presented in full, but the interested reader is referred to the literature for more in-depth detail [3, 12].

Consider a dislocation line segment pinned between two points, a distance $2L$ apart. These pinning points can be grain boundaries, other dislocations, or point defects in the material. Assume a small but non-zero longitudinal stress, σ, with shear component τ such that $\tau = R\sigma$ where R is the resolving shear factor, is then applied to this dislocation segment such that it bows out between the two pinning points. This geometry is depicted in Figure 1a, where the radius of curvature, r, of the bowed segment and angle θ are annotated. Note that this stress can be thought of as either an internal residual stress or externally applied stress, but it is small enough such that the dislocation segment does not break away from the pinning points. Assuming the dislocation density is small enough such that bowed dislocations act independently of each other, the line tension, T, of this dislocation segment due to the applied stress is $T = \mu b^2$ where b is the Burgers vector and μ is the shear modulus,

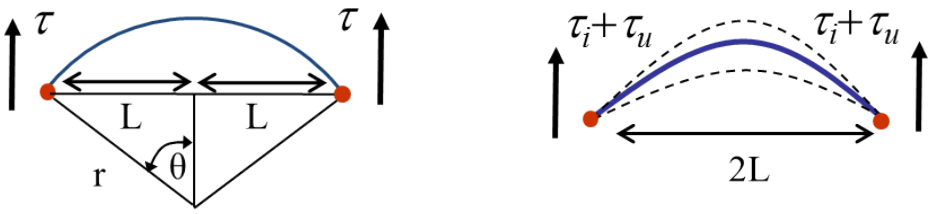

(a) (b)

Figure 1: (a) Diagram showing geometry of bowed dislocation segment of length $2L$ between two pinning points and under an applied shear stress τ, in terms of radius of curvature r and angle θ. (b) Diagram showing movement of dislocation segment with superimposed ultrasonic stress on top of initial stress τ.

such that shear stress can be expressed as [3]:

$$\tau = \frac{T}{rb} = \frac{\mu b}{2r} \tag{12}$$

The corresponding shear strain due to a distribution of bowed dislocations with density Λ is given as:

$$\gamma = \frac{\Lambda b}{2L} S \tag{13}$$

where S is the area swept out by the pinned dislocation under the applied stress, which is approximated as:

$$S = r^2 \left(\theta - \frac{1}{2} \sin 2\theta \right) \tag{14}$$

By approximating the angle $\theta = \sin^{-1}(L/r)$, this expression can be expanded in a power series of θ up to the fifth power, where $\theta = \sin^{-1} L/r$ and assuming L/r is small. The resulting expression relating shear stress and strain is given as:

$$\gamma = \frac{2}{3} \left(\frac{\Lambda L^2}{\mu} \right) \tau + \frac{4}{5} \left(\frac{\Lambda L^4}{\mu^3 b^2} \right) \tau^3 \tag{15}$$

The total strain in the material can be written as a summation of the lattice strain plus the strain due to the dislocation motion, i.e.

$$\epsilon = \epsilon_l + \Omega\gamma \tag{16}$$

where Ω is the conversion factor between shear and longitudinal strain. Assuming the same form of the stress-strain relation as in Equation 2 for the internal stress, the resulting stress-strain relationship due to the total strain in the material is:

$$\epsilon = \left(\frac{1}{E_1} + \frac{2\Omega\Lambda L^2 R}{3\mu}\right)\sigma + \frac{E_2}{E_1^3}\sigma^2 + \frac{4\Omega\Lambda L^4 R^3}{5\mu^3 b^2}\sigma^3 \tag{17}$$

Now consider a small ultrasonic stress $\Delta\sigma$ superimposed on the internal stress σ, causing a small additional strain $\Delta\epsilon$, the relation of which can be written as:

$$\Delta\sigma = \frac{\partial\sigma}{\partial\epsilon}\Delta\epsilon + \frac{1}{2}\frac{\partial^2\sigma}{\partial\epsilon^2}(\Delta\epsilon)^2 \tag{18}$$

which, from Equation 17, is equivalent to:

$$\Delta\sigma = \left[\frac{1}{E_1} + \frac{2\Omega\Lambda L^2 R}{3\mu}\right]^{-1}\Delta\epsilon - \left(\frac{E_2}{E_1^3} - \frac{24\Omega\Lambda L^4 R^3}{5\mu^3 b^2}\sigma_1\right)\left(\frac{1}{E_1} + \frac{2\Omega\Lambda L^2 R}{3\mu}\right)^{-3}(\Delta\epsilon)^2 \tag{19}$$

The nonlinearity parameter can be found by comparing the form of Equation 19 to Equation 2, and noting that the nonlinearity parameter is the negative ratio of the coefficients of the two terms, i.e. the first relation in Equation 4. Thus, the total nonlinearity parameter, β_{tot}, is given by:

$$\beta_{tot} = \left(-\frac{E_2}{E_1^3} + \frac{24\Omega\Lambda L^4 R^3}{5\mu^3 b^2}\sigma_1\right)\left(\frac{1}{E_1} + \frac{2\Omega\Lambda L^2 R}{3\mu}\right)^{-2} \tag{20}$$

To a good approximation for most materials, the term $2\Omega\Lambda L^2 R/(3\mu)$ is small compared to $1/E_1$, such that the total nonlinearity parameter can be written as:

$$\beta_{tot} = -\frac{E_2}{E_1} + \frac{24}{5}\frac{\Omega\Lambda L^4 R^3 C_{11}^2}{G^3 b^2}\sigma_1 \quad . \tag{21}$$

The first term is equivalent to the lattice contribution of the nonlinearity parameter, i.e. $\beta_l = -E_2/E_1$, so the change in nonlinearity parameter due to dislocation pinning can be written as:

$$\Delta\beta_{pd} = \frac{24}{5}\frac{\Omega\Lambda L^4 R^3 C_{11}^2}{G^3 b^2}\sigma_1 \tag{22}$$

It should be specifically noted that the internal stress σ_1 in this analysis is assumed to be much smaller than the yield stress of the material, such that dislocation

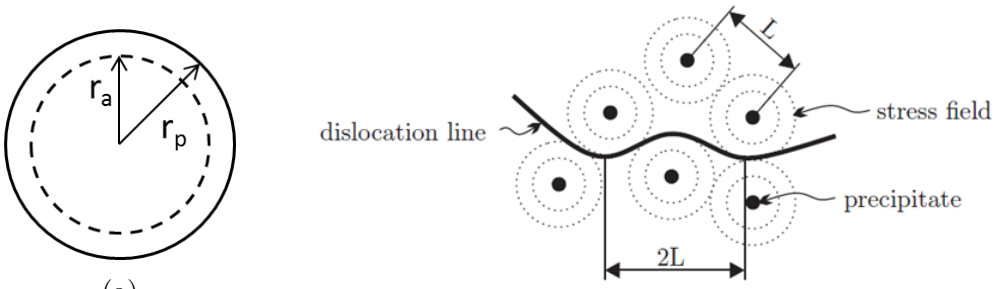

(a) (b)

Figure 2: (a) Diagram of precipitate with radius r_p embedded in a matrix with natural radius of r_a, and (b) diagram of a dislocation bending around a distribution of precipitates, with spacing of L.

displacement is small. The superimposed ultrasonic stress is also assumed to be much smaller than the yield stress. Thus, the "dislocation pinning" effect described here should not be confused with dislocation barriers impeding motion, such as in Orowan strengthening mechanisms.

2.3.2 Precipitate-pinned dislocations

We now consider the effect of a distribution of precipitates on the magnitude of β. Precipitates themselves do not have a significant effect on β [13], but their interaction with dislocations has shown to give rise to a significant change in the magnitude of β [7, 13, 14]. The change in β due to an applied stress σ on a pinned dislocation segment is given by [3], as derived in Section 2.3.1 above. Consider a precipitate with radius r_p embedded in the matrix, with a precipitate-matrix lattice misfit parameter δ such that $r_p = r_a(1+\delta)$, where r_a is the natural radius in the matrix, as depicted in Figure 2a [16]. As in previous work [12], we can approximate this as a spherical precipitate embedded in an isotropic medium, exerting a non-zero internal pressure p_0 on the matrix. The displacement, $u_r(r)$, and stress, $\sigma_{rr}(r)$, solutions in the radial direction at radius $r > r_a$ for this scenario are given in Eringen [17], as

$$u_r(r) = \frac{p_0 r_p^3}{4Gr^2} \quad , \quad \sigma_{rr}(r) = -p_0 \frac{r_p^3}{r^3} \tag{23}$$

Assuming the precipitate and matrix have different elastic properties, the pressure in the precipitate has been shown to be [18]

$$p_0 = 4G\delta \left[\frac{3B_p}{3B_p + 4G}\right] \frac{r_p^3}{r^3} \tag{24}$$

where B_p is the bulk modulus of the precipitate. The stress in the matrix at radius r due to this embedded precipitate can then be written as [14]:

$$\sigma_{rr}(r) = -4G\delta \left[\frac{3B_p}{3B_p + 4G}\right] \frac{r_p^3}{r^3} \tag{25}$$

We then assume there is a distribution of these spherical precipitates embedded in a microstructure with dislocations present. The precipitates exert a local stress field as described above in its vicinity. Since a dislocation line is assumed to follow a contour of minimum energy, it is assumed that two precipitates a distance $L/2$ away from each dislocation segment act on the dislocation segment, and contributions from other nearby precipitates are negligible. This scenario is depicted in Figure 2b. Thus, the stress is evaluated at $r = L/2$ [13], and the expression for average stress on a dislocation segment due to precipitates from Equation (22) becomes [14]:

$$|\sigma| = 2|\sigma_{rr}| = 64G|\delta| \left[\frac{3B_p}{3B_p + 4G}\right] \frac{\overline{r_p}^3}{L^3} \tag{26}$$

We can then write Equation (22) in terms of precipitate parameters to find the change in the acoustic nonlinearity parameter due to precipitate–pinned dislocations, $\Delta\beta_{ppd}$:

$$\Delta\beta_{ppd} = \frac{1536}{5} \frac{\Omega R^3 C_{11}^2}{G^2 b^2} \left[\frac{3B_p}{3B_p + 4G}\right] \left(|\delta| L \overline{r_p}^3 \Lambda\right) \tag{27}$$

where the terms in parenthesis are parameters that will most likely evolve throughout radiation damage in RPV steels under relevant conditions (i.e. the dislocation and precipitate parameters). The precipitate spacing can be estimated as $L \approx N_p^{-1/3}$, where N_p is the number density of total precipitates. The change in the acoustic nonlinearity parameter expressed in Equation (27) can be written in terms of number

density of precipitates:

$$\Delta\beta_{ppd} \approx 307\frac{\Omega R^3 C_{11}^2}{G^2 b^2}\left[\frac{3B_p}{3B_p+4G}\right]\left(|\delta|\frac{\overline{r_p}^3\Lambda}{N_p^{1/3}}\right) \tag{28}$$

The number density of precipitates is related to the volume fraction of precipitates, f_p, as $f_p = N_p V_p$, where $V_p = 4/3\pi\overline{r_p^3}$ is the average volume of precipitates. The change in acoustic nonlinearity parameter expressed in Equation (27) can also be written in terms of the volume fraction of precipitates:

$$\Delta\beta_{ppd} \approx 495\frac{\Omega R^3 C_{11}^2}{G^2 b^2}\left[\frac{3B_p}{3B_p+4G}\right]\left(|\delta|\frac{\overline{r_p}^3\overline{r_p^3}^{1/3}\Lambda}{f^{1/3}}\right) \tag{29}$$

Note that these results are the same as derived in [14], and based off of other previous work as well [7, 12, 13]. Further, it is useful to reiterate, in simpler terms, the dependence of $\Delta\beta$ on precipitate and dislocation parameters:

$$\Delta\beta \propto \frac{\overline{r_p}^3\Lambda\delta_p}{N_p^{1/3}} \quad and \quad \Delta\beta \propto \frac{\overline{r_p}^3\overline{r_p^3}^{1/3}\Lambda\delta_p}{f^{1/3}} \tag{30}$$

2.3.3 Vacancy contribution

Similarly to precipitates, the stress field surrounding a vacancy and vacancy clusters, σ_v, can interact with the stress field of the dislocation, causing a change in the magnitude of the acoustic nonlinearity parameter [19]:

$$\Delta\beta_v = \frac{24}{5}\frac{\Lambda\Omega R^3 L^4 A_{11}^2}{b^2 G^3}|\sigma_v| \tag{31}$$

To develop an expression for the stress field due to a vacancy or vacancy clusters, first consider the misfit strain due to a vacancy [20]:

$$\epsilon = \frac{(1+\nu)}{3(1-\nu)}\delta_v \tag{32}$$

where ν is Poisson's ratio of the matrix material, and δ_v is the misfit parameter of a vacancy, which is in the range of -0.1 to 0 [20]. The corresponding radial stress at a distance r from the vacancy is

$$\sigma_{rr} = \frac{-4G\epsilon r_v^3}{r^3} \tag{33}$$

where r_v is the radius of the vacancy (typically $r_v \approx b/2$). Similar to the precipitate case, the stress is evaluated at $L/2$ and assuming $\sigma = 2\sigma_{rr}$, Equation 100 becomes, similar to the definition in [19]:

$$\Delta\beta_v = \frac{512}{5}\frac{\Omega\Lambda R^3 C_{11}^2 (1+\nu)\,\delta}{G^2 b^2 (1-\nu)} L r_v^3 \tag{34}$$

The question now remains of how to calculate the loop length L. If the material contains only dislocations and a distribution of vacancies (no precipitates present), then if the loop length can be expressed in terms of the volume fraction of vacancies, i.e. $f_v = (4\pi/3)\,(r_v/L)^3$, and the expression for $\Delta\beta_v$ becomes:

$$\Delta\beta_v \approx 165\frac{\Omega\Lambda R^3 C_{11}^2 (1+\nu)\,\delta}{G^2 b^2 (1-\nu)} \frac{r_v^4}{f_v^{1/3}} \tag{35}$$

2.4 Current Detection Capabilities

There has been significant work in the past few decades aimed at using NLU as an NDE technique for early damage detection, by relating the acoustic nonlinearity parameter to different microstructural features. It has been shown both theoretically and experimentally that metal materials have an inherent nonlinearity that is due to the lattice anharmonicity of the crystal structure [1]. It is known that β depends on crystalline structure, which was shown by calculating β for pure mode propagation for various single-crystals [5]. It has been shown that dislocations and their substructures give rise to increases in β, as well as precipitates and vacancies, as described in Section 2.3. An early example of the dislocation contribution was shown in Hikata et al. [3], where the authors presented a theoretical model to express the dislocation contribution to β in aluminium single crystals, and experimentally measured the change in β at different levels of applied stress. Another early work utilizing second harmonic generation measurements were in copper crystals that were annealed and neutron-irradiated to 3.6×10^{15} n/cm^2 [2]. Note in comparison, the neutron fluence for RPV materials is about $1-3\times10^{19}$ n/cm^2 (E $>$ 1 MeV)after 40 years of operation.

Their results showed a decrease in second harmonic amplitude as well as in measured attenuation due to neutron bombardment, which they postulate was caused by the pinning of dislocations. This section reviews the literature on fatigue- and dislocation-based monitoring, and thermal aging monitoring using SHG.

2.4.1 Fatigue- and dislocation-based monitoring

Due to the strong link between second harmonic generation and dislocation density, a significant amount of work has focused on monitoring fatigue damage with nonlinear ultrasound. Cantrell and Yost [8] presented a theoretical model that derived how dislocation dipoles cause the generation of a second harmonic and thus contribute to β. To prove their model, they measured a monotonic increase in β throughout fatigue in Al-2024 T4, which was in good agreement with their theoretical model. Cantrell further developed a theoretical model to express β due to a combination of lattice anharmonicity, dislocation monopoles, and dislocation dipoles [15].

Other experimental work has used β to monitor fatigue damage with a variety of wave types and in a variety of materials [21–27]. Frouin et al. [24] measured sound velocity, attenuation, and acoustic nonlinearity in fatigued Ti-6Al-4V. Results showed that acoustic nonlinearity measurements of β were more sensitive to fatigue than the linear measurements, since β increased by 180% throughout fatigue life. Kim et al. [25] measured increases in β in nickel superalloys throughout low- and high-cycle fatigue life with longitudinal waves. Herrmann et al. [26] also looked in effects of monotonic and cyclic loading in a nickel superalloy on the acoustic nonlinearity parameter using Rayleigh waves. Results showed an increase in β in both loading types, where the increase was much greater in the initial stages of either fatigue life in cyclic loading or in applied stress in monotonic loading. The trend of measured β was found to be similar using both longitudinal waves [25] and Rayleigh waves [26] in nickel superalloys, indicating the change in acoustic nonlinearity parameter is independent

of wave type used. Pruell et al. [27] measured β using nonlinear Lamb waves in Al-1100-H14 specimens throughout fatigue damage. Results showed an initial sharp increase to about $1.2\beta_0$ then a saturation at higher fatigue cycles. These results are similar in nature and trend to results using longitudinal and Rayleigh waves to measure fatigue damage in other metals [26]. Further, measurements of acoustic nonlinearity parameter have been used to monitor plastic deformation in A36-type steel under quasi-static, monotonic tension, and low cycle fatigue [28].

Previous work has also shown that β is sensitive to cold work, which produces a significant amount of dislocations in the material. For example, Viswanath et al. [29] measured β with longitudinal waves in cold-worked 304 stainless steel. The results showed a positive correlation of β with percent cold work, and also with yield strength and tensile strength. Results were explained in terms of dislocations and dislocation substructures formed during cold rolling. Another example is by Liu et al. [30], where the authors measured β with Rayleigh waves in shot peened aluminum 7075 samples. Results showed an increase in β with peening intensity, which was attributed to cold work and residual stresses in the material's surface. Previous work has also shown an increase in β with increasing carbon content in quenched steel specimens [31], which was attributed to increasing amounts of dislocations with carbon content and interpreted using a pinned-dislocation model, as described below.

2.4.2 Thermal Aging Monitoring

Significant work has considered the effect of microstructural features that evolve throughout thermal aging, such as precipitates, to the acoustic nonlinearity parameter. Yost and Cantrell [32] measured an increase of about 10% in β throughout the heat treatment of Al-2024 from the T4 to T6 temper. They pointed out that the change in β due to fatigue had been shown to be much greater than changes due to

precipitates, but that precipitate structures could greatly affect the dislocation structure and interactions during fatigue. The authors then developed a theoretical model that related changes in β to coherency strains in the matrix [33] in their case, the coherency strains were a result of precipitates in the matrix, as shown in Section 2.3.2. They found β was proportional to the volume fraction of precipitates and the effective misfit of the precipitate in the matrix. Cantrell and Zhang [13] further modified this model to incorporate dislocation and precipitate interactions to describe changes in β. Yet another model was developed to relate both the growth of precipitates and nucleation of precipitates to β [7]. This model was then compared to experimental measurements of β (from [32]) measured over precipitation heat treatment time in aluminum 2024, going from the T4 to T6 temper. Results gave two different values for fit parameters, but both results are consistent with the fact that most precipitates nucleate within the first portion of heat treatment time. Results showed an increase in β after short aging times, then a decrease in β (to below the value in the unaged state) with increasing aging time, and then a second increase in β at even longer aging times.

Measurements of β have been made in a variety of materials subjected to thermal aging. Baby et al. [34] measured the acoustic nonlinearity parameter in a titanium alloy subjected to creep damage (837 K at constant 300 MPa applied stress), which produced an increase of volume fraction of voids in the microstructure. Results showed an increase in β up to about 60% of creep life, followed by a decrease in β, with a maximum of about a 200% increase. They attributed the increase in β to the increase in volume fraction of microvoids, and the decrease in β to an increase in the damage scale caused by coalescence of the microvoids as seen by optical microscopy. Xiang et al. [35] measured β during thermal aging of ferritic Cr-Ni steel. They found β increased by a factor of about 3 during the first 1000 hours, and then decreased to about the initial value of β by the end of the heat treatment cycle (1.6×10^5 hours).

The general trend of β somewhat followed the Vickers hardness of the material at each stage of heat treatment. Increases in β were attributed to an increase in precipitates, and the decrease in β was attributed to the increasing mismatch in phase velocities of the first and second harmonic Lamb wave modes due to initiation of microvoids, though the experimental results show significant scatter.

Hurley et al. [14] measured β in ASTM A710 steel that was heat treated to produce varying amounts of precipitate hardening. Results were compared to inhomogeneous strain. The paper claims a positive correlation is seen, but only results from one sample set was convincing - the results from the second sample set does not show a clear linear trend between β and strain as the authors claim. A modified model from [55] to express the contribute of β from precipitate and dislocation interactions, but experimental results could not be compared to this model since the authors were unable to measure dislocation density. C. S. Kim et al. [36] measured β due to thermal degradation of ferritic 2.25Cr-1Mo steel. Results showed an increase to roughly $1.7\beta_0$ up to about 2000 hours thermal degradation time, and then a saturation of β with further degradation. The authors attribute the change in β to the lattice mismatch in second phase precipitates of M_6C carbides, but this result is not fully convincing. Viswanath et al. [37] measured β in M250 grade maraging steel subjected to thermal aging of varying times. Results show a linear increase in β during the middle stages of heat treatment time, which the authors explain is due to precipitation of Ni_3Ti that causes microstrain. The authors used a prior theoretical model [33] to explain their results. In Ruiz et al. [38], the authors measured β over increasing thermal damage in 2205 duplex stainless steel. Results were related to the increasing formation of the sigma phase over increasing time of thermal aging.

2.5 Summary

This chapter reviewed the concepts, theoretical derivations, and current literature on the nonlinear ultrasonic technique of second harmonic generation. The main points of the chapter are summarized as follows:

- The main concept behind this technique is that a second harmonic wave is generated as an incoming wave interacts with microstructural features in the material, and is characterized by the acoustic nonlinearity parameter, β.
- Dislocation pinning, precipitate-pinned dislocations, and vacancies all affect the magnitude of the acoustic nonlinearity parameter.
- Nonlinear ultrasound has been used extensively for early detection of fatigue damage in a variety of metals (aluminum, steel, and nickel alloys), as well as cold work and shot peening, due to the dislocations and dislocation structures that form.
- Nonlinear ultrasound has been used to detect microstructural changes due to thermal aging in metals due to precipitation phases that form during thermal aging.

CHAPTER III

RADIATION DAMAGE IN RPV STEEL

3.1 Chapter Overview

This chapter gives a broad overview of radiation damage in reactor pressure vessel(RPV) steels. The effects of radiation damage in steel materials is highly dependent on many factors such as specific material composition, neutron fluence, irradiation temperature, and neutron flux. This chapter focuses on effects in different RPV steels under relevant operating conditions. The chapter begins with an overview of nuclear reactor pressure vessels in operation in the US, giving a motivation for developing a nondestructive method of evaluating radiation damage in these structures. Microstructural change in RPV steels due to irradiation and the corresponding macroscopic changes (i.e. mechanical property changes) are then discussed. Finally, microstructural effects due to post-irradiation annealing and re-irradiation are discussed.

3.2 Background: Nuclear Reactors

Nuclear power plants generate roughly 20% of electricity used in the US. They use the heat generated from nuclear fission - energy released from the splitting of atoms - of uranium fuel to generate electricity. The most common nuclear reactor type is the light water reactor (LWR), which is a thermal reactor that uses water for coolant. There are two types of LWRs in operation throughout the US - the pressurized water reactor (PWR) and the boiling water reactor (BWR). In a PWR, water is heated from the fission reaction and kept under pressure so it does not boil. This heated water (in the primary loop) flows into a heat exchanger where heat is transferred to

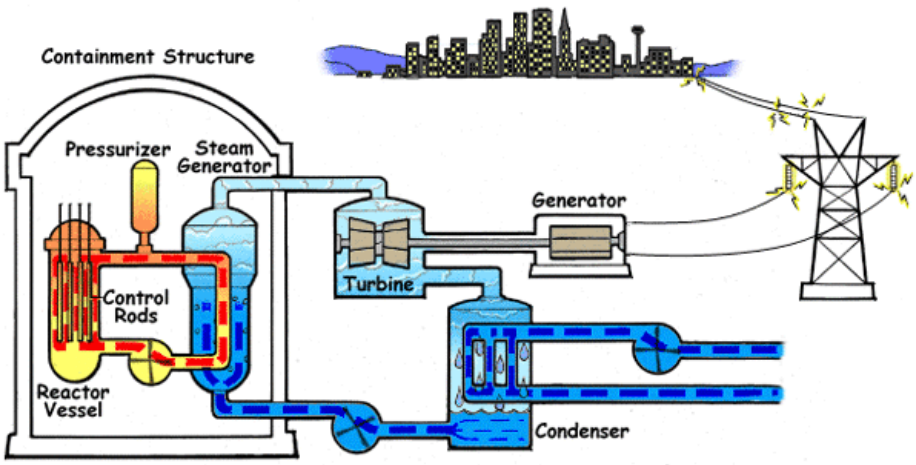

Figure 3: Diagram of a pressurized water reactor, illustrating reactor pressure vessel on the left-hand side.

separate water in the secondary loop through the walls where it evaporates as steam, which is then fed to a turbine that drives a generator connected to the electric grid. All components that contain contaminating material - the reactor pressure vessel, the primary loop components and water, and the steam generator are enclosed in a containment structure made of extremely thick concrete. A diagram of the PWR is shown in Figure 3 [39].

The reactor pressure vessel (RPV) itself is a crucial structure as it contains the reactor core, where the fission reaction takes place. A by-product of fission is neutron radiation, which degrades materials over time. Therefore, the RPV receives significant radiation damage over time, which ultimately causes embrittlement and a reduction in ductility of its components. The RPV is typically made up of 24 cm thick low-alloy steel plates welded together with a stainless steel cladding (about 10 mm thick) on the interior, and the vessel itself is about 4.6 m in diameter, 14 m in height [40]. Reactor pressure vessel steels are low-alloy steels typically composed of Cu(0.05-0.2 wt.%), Mn(0.7-1.6 wt.%), Mo(0.4-0.6 wt.%), Ni(0.2-1.4 wt.%), Si(0.2-0.6 wt.%), and Cr (0.05-0.5 wt.%) [41]. The region closest to the reactor fuel, called the belt-line region, receives the highest amount of neutron radiation and is thus the most critical

part of the RPV in terms of material damage. RPVs typically operate around 290°C and at pressures of about 7 MPa in BWRs and about 14 MPa in PWRs [41].

The common measure of radiation damage is displacements per atom (dpa), which is defined as the average number of times an atom is displaced during irradiation, and depends on the neutron energy spectrum. An analogous convention is fluence (ϕt), which is defined as the neutron flux (ϕ) integrated over time (neutrons/m^2 or n/m^2). The neutron flux (ϕ) is defined as the number of neutrons per unit area per unit time (neutrons/m^2–s). The spectrum of neutron energies must be specified when using units of neutron flux and fluence. At the end of roughly 40 years (typical design lifetime) of operation of a US PWR, the components in an RPV are typically at a fluence of $1 - 3 \times 10^{23}$ n/m^2 for E > 1 MeV, which corresponds to about 0.04-0.05 dpa [41].

3.2.1 Current NDE and surveillance methods

Currently, there is no nondestructive evaluation (NDE) method for unambiguously measuring the amount of radiation damage in material. Current NDE methods used for reactor component inspection are limited to crack detection using techniques such as ultrasonic (linear) methods, eddy currents, and remote visual inspections. Radiation damage assessment in material is accomplished through surveillance programs. Here, representative samples are placed in the nuclear reactor, and then they are removed during reactor shut–downs to perform destructive testing such as Charpy impact tests to monitor the likely state of damage of the actual components [41]. These samples can provide a limited prediction of material embrittlement, since they are dependent on knowing accurate information about operating temperature, fluence, flux, and material composition. However, actual fluence levels might only be accurate to within 25% since they are determined by reactor physics calculations based on location information and surveillance dosimetry, and material compositions are not

necessarily well–known or documented and copper content uncertainties can be as high as 30% [40]. Test reactors provide higher flux to therefore achieve higher fluence over a shorter time span for experimental characterizations of material samples, but since the flux is higher than in a nuclear power reactor, the material degradation will not necessarily correlate to the damage state of a material at the same fluence at a lower flux.

3.2.2 Planned life extension

Many reactors throughout the U.S. are close to or have surpassed their design life of about 40 years of operation, and older plants are currently undergoing assessment of technical basis to operate beyond 60 years. The U.S. Department of Energy (DOE) and the U.S. Nuclear Regulatory Commission (NRC) have initiatives in place for life extension of reactors to 60–80 years of operation, so that these reactors can remain operational while more advanced nuclear technologies are being developed and deployed [42]. Reactor components will thus receive higher radiation dose than originally designed for, so there is a need to develop a method of determining material aging due to radiation embrittlement to ensure continued safe operation of these power plants. To this end, it would be extremely useful to develop a nondestructive evaluation technique that could monitor radiation damage (i.e. embrittlement and decreasing ductility) on relevant RPV components for early detection of probable damage sites to enable nuclear power plant sustainability [43].

3.3 Radiation-Enhanced Diffusion

In the radiation damage event, high-energy neutrons (typically up to 10 MeV of kinetic energy in nuclear power plant reactors [44]) bombard the material and collide with atoms, creating a high-energy primary knock-on atom (PKA) [45]. A series of resulting collisions displace atoms from their original lattice site, producing a cascade of point defects (i.e. vacancies and self-interstitial atoms, SIAs). This cascade

subsides when the energy of the particles falls below that needed to displace atoms from their lattice sites; the time scale of this entire event is on the order of 10^{-11}s. At the higher operating temperatures of RPVs, these point defects diffuse through the ferrite matrix and either dissolve at sinks (e.g. grain boundaries, dislocations), vacancies and SIAs recombine or self-heal, or defects grow into larger clusters and dislocation loops [44, 46–48]. The excess amount of vacancies causes accelerated diffusion rates of solute atoms, known as radiation-enhanced diffusion (RED). Diffusion rates due to RED have been shown to be orders of magnitude higher than thermal diffusion rates for relevant neutron fluxes of nuclear reactors. The primary effect of RED is the acceleration of precipitation of copper, resulting in a high number density of small and coherent bcc copper-rich precipitates (CRPs) [47, 49–51]. RED and the migration of point defects also lead to cluster formation, dislocations, loops, and eventually cavities [45]. The evolution of these defects is highly dependent on the irradiation temperature, flux, fluence, and material composition.

3.4 Microstructural Changes

The irradiated microstructure of RPV steels under relevant fluence levels has been shown to consist of solute clusters [45,52], dislocation loops [45,53,54], and copper–rich precipitates [48, 55–58], typically on the order of 1–3nm in diameter and in quantities of number density larger than $10^{23}/\mathrm{m}^3$ [41, 47]. Note that both clusters and precipitates are aggregates of solute atoms, but clusters have no distinct interface within the matrix, whereas precipitates have a well–defined crystal structure and interface within the matrix [59]. Different dislocation density evolution trends have been reported - it has been shown that dislocation density remained constant [60], slightly decreased [61, 62], or increased [62] - though dislocation density appears to saturate at higher fluence, and the trend supposedly depends on initial microstructure of the material [62].

Research on multiple types of RPV steel has shown that an increase in fluence causes an increase in volume fraction of nanoscale defects such as solute clusters [57, 63], copper rich precipitates [57, 58], and dislocation loops [53, 54], followed by saturation with further increases in fluence [60]. Fluence and material composition supposedly do not have a pronounced effect on the size of defects [52]. At low fluence, the microstructure has been reported as inhomogeneous [57, 61]. Flux has a profound effect on the irradiated microstructure, which makes experimental characterization and prediction of low flux–high fluence embrittlement difficult [64]. Models have been developed to account for embrittlement at different fluxes [48, 65], but there is still a need for accurate experiments on which to base these models at the low flux typical of RPV components [64]. Material composition has been shown to influence the evolution of nanoscale defects observed in the irradiated microstructure - generally, volume fraction of nanoscale defects increased with increasing fluence and copper and nickel content [52, 58, 66]. A systematic study that investigated ferritic alloys and RPV steels showed that the presence Cu produced a greater increase in dislocation loops during irradiation, and the presence of Mn and Ni atoms hindered the growth of dislocation loops [54]. It has been shown that the presence of small amounts of Cr (about 0.1%) in ferritic alloys causes small dislocation loops to form even at low fluence, and also suppresses void formation [67]. It has been shown that in high Ni content RPV weld steels, precipitates and nanoclusters formed during irradiation were preferentially located along dislocations [57, 68]. In material with very small amounts of Cu and/or Ni, vacancy clusters have been shown to dominate the irradiated microstructure [67].

Most information about the evolution of microstructure in irradiated materials throughout the literature comes from microstructural characterizations as opposed to material models [69]. These characterizations come from techniques such

Positron Annihilation Spectroscopy (PAS) [54,60,61,70,71], small–angle neutron scattering (SANS) [52, 54, 55, 60, 66], transmission electron microscope (TEM) techniques [53, 54, 60, 63, 66, 72, 73], high resolution field emission scanning transmission electron microscopy (FEGSTEM) [49,66], and atom probe tomography [54,57,63,68,74], and multiple authors cite the need for performing more than one characterization to accurately interpret results from a single experimental technique [66, 70]. Molecular dynamics (MD) simulations have explored cascade effects on point defects of the radiation damage event and RED on migration and evolution of vacancies and SIAs [41, 44, 46]. Other numerical modelling initiatives primarily focus on kinetic Monte Carlo methods [75–77], cluster dynamics models [78], and the mean field method [75].

3.4.1 Copper-Rich Precipitates

In materials with Cu content greater than ≈ 0.1 wt.%, copper has shown to be more efficient in forming precipitates in irradiated steels than other alloying elements [58]. At RPV operating temperatures (≈ 290°C), the dissolved copper in the matrix is supersaturated. Copper–rich precipitates nucleate and grow due to RED, and they pin dislocations causing hardening [41, 56]. CRPs can also be enriched with Mn, Ni, Si, and P [46], and larger amounts of these elements in RPV material leads to increased nucleation rates and number densities of CRPs [46]. These precipitates have been shown to dominate early embrittlement in RPV steels containing greater than about 0.05-0.1% Cu, and their nucleation and growth saturates at higher fluence due to depletion of Cu in the matrix [41]. The neutron fluence at which CRP nucleation begins increases with decreasing Cu in the material due to the lower nucleation rate [46]. It has been shown that an increase in flux shifts the saturation of CRP contribution to hardening to higher fluence levels [48], or in other words higher flux slows the rate of precipitation of CRPs. RPV steels with Ni and Mn content contain CRPs that

are alloyed with Mn and Ni, both of which act to increase the volume of the precipitates [41]. It has also been shown that the addition of P acts to increase the number density of precipitates [46].

It has been suggested that during irradiation and thermal aging, copper atoms are dragged by migrating vacancies that form, due to the high binding energy between a copper atom and a single vacancy [79]. This is the mechanism for which copper-vacancy complexes form in irradiated steel, and these complexes ultimately evolve into the Cu-rich precipitates. This effect has been shown in atomistic simulations [80], and other positron annihilation spectroscopy results support this hypothesis [81].

As an example of the amount of precipitation formed during irradiation, atom probe tomography has shown, that irradiation up to a fluence of 5×10^{23} n/m^2 (E>1 MeV) in ASTM A533 steel with 0.14 wt.% Cu (referred to as JRQ) produced a large number density of CRPs, on the order of 3×10^{23} n/m^2 with an average radius of about 1 nm [82]. The composition of these precipitates was found to consist of Fe and Cu, enriched with Ni, Mn, Si and P. These copper-rich precipitates have also been seen by SANS techniques, e.g. [52, 54, 83].

3.4.2 Matrix Features

Matrix features that form during damage cascades are believed to be solute-vacancy cluster complexes, and are divided into two separate categories - unstable matrix defects (UMDs) and stable matrix features (SMFs) [47,48]. UMDs are primarily sub-nm scale vacancy clusters that can form in steels even with little to no Cu content, and they dissolve quickly (compared to typical reactor irradiation times) at typical reactor operating temperatures of 290°C [41]. However at high fluxes typical of test reactors ($\phi > 10^{16}$ n/m^2-s), these features can become significant. The increased amount of UMDs at high fluxes actually act as sinks, reducing RED and thus delaying CRP nucleation and growth [41]. They can further act as nucleation sites for SMFs.

SMFs are matrix features that remain in the microstructure for longer times. These features can include dislocation loops, vacancy-solute clusters, dislocation atmospheres, and small precipitates enriched with Mn, Ni, Si, and/or P [46]. These matrix features contribute to embrittlement, which generally increases with decreasing irradiation temperature and increases with square root of fluence [84], as they are weaker obstacles to dislocation motion.

3.4.3 Manganese-Nickel Precipitates

In materials with elevated levels of Mn and Ni, or with low levels of Cu, manganese-nickel-rich precipitates (MNPs) have been shown to form in the irradiated microstructure [46, 47, 85]. Lower irradiation temperatures promote the formation of these MNPs [41], which have been found in larger volume fractions than CRPs [47]. Pure MNPs form at a much slower rate than CRPs, and are thus referred to in the literature as "late–blooming phases" [46, 84]. Characterizing these features and their embrittlement effects is still an ongoing area of research, as it still has yet to be determined if these phases could contribute to increased embrittlement at low flux but very high fluence, which would be a concern for extended operation of nuclear reactors.

3.4.4 Phosphorous Phases and Segregation

It has been shown that phosphorous can contribute to radiation embrittlement [46,47, 49, 56, 59]. RED promotes P diffusion and nucleation of phosphide phases due to its low solubility in RPV steels, even though P is typically found in very small quantities (<0.05 wt.%) [46, 56]. There is a strong interaction of P and Mn elements, which can potentially form Mn_3P phases. Phosphorous has been shown to increase the CRP contribution to irradiation hardening in some cases, but this effect becomes less pronounced in RPV steels with much higher Cu content [46]. It has also been shown that irradiation causes phosphorous segregation to dislocations and grain boundaries,

which can contribute to irradiation hardening [46, 86]. However, P segregation to grain boundaries leads to brittle intergranular fracture, which has not been seen as a dominant failure mechanism in light water reactor RPV steels (typical US RPV materials).

3.5 Macroscopic Damage

The most prominent manifestation of radiation damage is embrittlement, which can be characterized by a shift in the ductile to brittle transition temperature (DBTT) to higher temperatures (meaning a decrease in impact and fracture toughness) and an increase in the yield strength [41, 52, 53, 57, 63, 87]. The DBTT is the approximate temperature at which the low-toughness brittle fracture regime of the material transitions to the high toughness ductile fracture regime – the transition region tends to exhibit a sharp increase in energy with temperature, but is not always well-defined especially in some irradiated steels. The DBTT can be measured using standard testing procedures of Charpy-V-notch impact tests and fracture toughness tests at increasing temperatures. The Charpy impact energy curves are determined by measuring the energy required for fracture of Charpy samples at different temperatures, producing curves similar to those shown in Figure 4. The DBTT is typically defined as the fracture temperature of 41 Joules of absorbed energy, T_{41}. These tests have been utilized in surveillance programs due to their simplicity. Fracture toughness tests using compact specimens and require more complex test setups that were not available at the start of surveillance programs and the beginning of current operational reactors [41], but these tests are used as a separate method of determining embrittlement effects, e.g. [87, 88].

It has been shown that nanoscale features form during irradiation and their interactions with dislocations cause an increase in hardness and yield stress, and causes an increase in the DBTT [41] and in some cases a decrease in the upper shelf energy

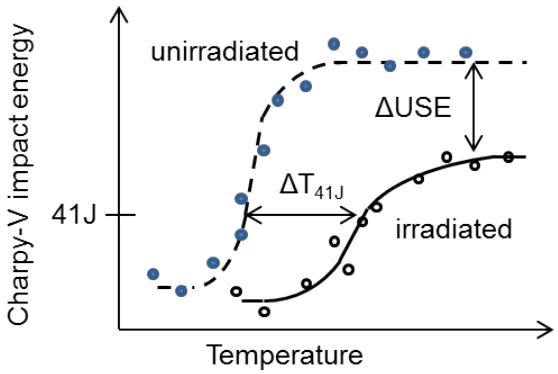

Figure 4: Pictorial representation of the change in Charpy-V transition temperature (ΔT_{41}) and upper shelf energy (ΔUSE) of irradiated RPV steel compared to the unirradiated state.

(USE); these changes are depicted in Figure 4. Failure of the RPV in pressurized-water-reactor pressure vessels due to pressurized thermal shock (PTS) is a major concern in RPV operation [89]. PTS can occur during reactor transients where the reactor is quickly cooled (inducing a thermal shock) but still under pressure or simply pressurized while still at low temperature (typical of end of reactor shut-down events). Extensive loss of fracture toughness of the RPV is a major concern in the operation of nuclear reactors for extended periods of time beyond their original design life of 40 years, where flaws could rapidly propagate through RPV wall.

It has been empirically shown that the increase in yield stress and the DBTT are related, generally by:

$$\Delta T_{41} = C\Delta\sigma_y \tag{36}$$

where $C \approx 0.65(\pm 15)$°C/MPa [50, 88, 90]. The USE has also been shown to empirically correlate with the change in yield stress [47, 90], and irradiation-induced reduction of USE has been shown to cause an additional increment of increase of T_{41} [46]. A two–component model was developed [41, 91] to predict embrittlement of irradiated RPV material based on two categories of irradiation–induced microstructural features: copper rich precipitates (CRPs) and stable matrix features (SMFs).

Their model is based on the observations that CRPs are the main contributor to embrittlement at low fluence and then saturate when copper has depleted in the matrix, and SMFs are the main contributor at higher fluences [41]. The authors further developed an experimental database of hardness changes due to irradiation, to break down contributions of different elements to formation of CRPs and SMFs results of which validate this two–component model [56]. This model has since been improved to predict transition temperature shifts in RPV steels, and is currently under consideration to be included in the NRC regulatory guide [84].

3.5.1 Model for Yield Stress Increase

Radiation damage causes defects in the material that act as dispersed obstacles to dislocation motion, causing an increase in yield strength. These obstacles are known to be some combination of copper-rich precipitates (subscript *crp*), nano-voids (subscript *nv*), interstitial (subscript *ic*)and vacancy (subscript *vc*) clusters or loops, and other phases (subscript *p*) such as phosphides and carbonitrides. Depending on the relative dislocation barrier strengths of these defects, the total change in yield stress due to the combination of these defects can best be represented as a root square sum (RSS), or linear sum (LS). Irradiation-induced defects in fluence and temperature ranges typical of the RPV are known to be weak-to-medium strength obstacles [92], so the total change in yield stress, $\Delta\sigma_y$, can be approximated as the RSS of the contributions for individual obstacles or defects:

$$\Delta\sigma_y = \sqrt{\Delta\sigma_{crp}^2 + \Delta\sigma_{nv}^2 + \Delta\sigma_{ic}^2 + \Delta\sigma_{vc}^2 + \Delta\sigma_p^2} \tag{37}$$

However, this approximation is not entirely valid, since in the unirradiated state most RPV steels contain strong obstacles (e.g. Mo_2C carbides) that are unchanged during radiation damage [41]. On the other hand, defects produced in radiation damage are generally weak dislocation pinning points.

Russell and Brown [93] proposed a model for strengthening due to interaction

of dislocations with a modulus mismatch in an Fe-Cu system, which is applicable to copper-rich precipitates and nano-voids in radiation damage [92]. The change in yield stress for features following the Russell-Brown hardening model, $\Delta\sigma_{rb}$, was proposed as [93]:

$$\Delta\sigma_{rb} = RGb\left[1 - \left(\frac{G_{rb}\log(r_{rb}/r_{ic})}{G\log(r_{oc}/r_{ic})} + \frac{\log(r_{oc}/r_{rb})}{\log(r_{oc}/r_{ic})}\right)^2\right]^{3/4} \frac{f_{rb}^{1/2}}{1.77 r_{rb}} \tag{38}$$

where R is the Schmidt factor, b is the Burger's vector, G is the shear modulus of the matrix material, r_{rb} is the radius of the feature that is described by the Russell-Brown model, r_{ic} and r_{oc} are the inner (dislocation core) and outer strain-field cut-off radius, and G_{rb} is the shear modulus of the feature.

For other features induced by radiation damage, the yield stress increase can be expressed as [94]

$$\Delta\sigma_j = R\gamma_j Gb\sqrt{2 r_j N_j} \tag{39}$$

where γ_j is the strengthening factor for the j-th feature, r_j is the radius, and N_j is the number density of the j-th feature. Defects produced in radiation damage generally produce weak dislocation pinning points, such that $\gamma_j < 0.4$ [41]. It has been suggested that strengthening by vacancy clusters, other phases such as phosphides and carbonitrides, interstitial clusters, and dislocation loops can be described by the form of σ_j [92]. So, by combining the models for σ_{rb} and σ_j into the total change in yield stress given in Equation 37, the total change in yield stress can be written in terms of size and number density of all the microstructural features.

3.6 Post-Irradiation Annealing

One potential method of mitigating radiation-induced embrittlement in the RPV is thermal annealing at temperatures much greater than the irradiation temperature (T_i) [95]. This has been shown to effectively recover some or most of the radiation embrittlement, depending on the material, irradiation, and annealing parameters [47, 82, 88, 96]. Nanstad et al. [88] investigated post-irradiation annealing effects

on hardness, yield stress, transition temperature, and fracture toughness of two RPV materials irradiated up to 5×10^{19} n/cm^2 (E>1 MeV) and annealed for 18-168h at 460°C. Results showed almost full recovery of the DBTT, specifically the Charpy T_{41-J} shift, and the resulting upper-shelf energy of the annealed samples was higher than that of the unirradiated material.

The microstructure due to PIA in RPV steel has been characterized by a low number density of large copper-rich precipitates [86, 97, 98]. During annealing, small precipitates dissolve in the matrix while others grow and coarsen – these coarsened precipitates have shown to be incoherent (fcc) with the matrix (bcc). Kuramoto et al. showed with atom probe tomography (APT) that in VVER-440-type weld material, CRPs coarsened at carbide-matrix interfaces and dislocations [97]. It has also been shown, with APT, that in ASTM A533 (JRQ) RPV steel, annealing caused a decrease of about an order of magnitude of number density of precipitates, increase in the precipitate size, and additionally phosphorus segregation on grain boundaries and dislocations [82, 86]. Phosphorus segregation to dislocations was also seen in the re-irradiated microstructure of VVER 400 weld metals [99]. An investigation of VVER-440 type RPV material with SANS also showed complete dissolution of CRPs following PIA in some materials, and partial dissolution of CRPs and coarsening of remaining precipitates [98].

In terms of physical feasibility of annealing an entire RPV, note that thermal annealing on an RPV has been previously done on a VVER Russian reactor design (a type of pressurized water reactor). Though this has not, to the author's knowledge, been completed on an RPV in the US, this thermal annealing process and details for the Nuclear Regulatory Commission requirements for the process can be found in the *Title 10 U.S. Code of Federal Regulations, Part 50* [95].

3.7 Re-Irradiation After PIA

Microstructural changes and the rate of embrittlement of re-irradiation following post-irradiation annealing (PIA) treatments is still an area of ongoing research [86, 97]. Results of Nanstad et al. [88] discussed in Section 3.6 showed that an intermediate annealing of 460°C/18h when 50% of the target neutron fluence was reached caused an increase in hardness and yield stress of only about half that as samples without an intermediate anneal. They found that except at higher fluence levels ($4 - 5 \times 10^{19}$ n/cm^2), annealing did not cause a difference in the rate of embrittlement during re-irradiation in terms of the shift of the DBTT, however the Charpy upper-shelf energy was still higher for re-irradiated samples compared to those that were not annealed. The intermediate anneal also resulted in less re-irradiation embrittlement of fracture toughness. Comparison of the ratio of DBTT to change in yield stress showed large discrepancies of the re-irradiated samples at lower fluence compared to pure irradiation (no intermediate annealing), potentially indicating intergranular fracture during the impact tests.

The re-irradiated microstructure has been shown to be somewhat different than the purely-irradiated microstructure of RPV material. Since PIA causes coarsening and growth of a few precipitates, the available copper in the matrix to form CRPs during re-irradiation is less than during the initial irradiation. So, there is a slower rate of cluster formation during re-irradiation compared to initial irradiation. Kuramoto et al. [97] showed that the coarsened precipitates seen following PIA were still present in the re-irradiated microstructure, as well as smaller newly formed CRPs, which were seen (with APT) mostly in the matrix. Segregation of phosphorous and CRPs to dislocations was also seen. Differences in positron annihilation spectroscopy (PAS) results of irradiated and re-irradiated material showed that matrix defects were the primary hardening mechanism in the re-irradiated samples [97].

3.8 Proposed NDE Techniques for Radiation Damage

Other techniques have been proposed for NDE of radiation damage in RPV materials, measurements of magnetic properties having received the most attention in the literature, for example magnetic hysteresis measurements [100–103], and Barkhausen noise (BN) measurements [104, 105]. Magnetic hysteresis and BN measurements are sensitive to lattice defects, which interact with domain walls (transition region where the magnetic moment changes direction), and change the shape of the hysteresis loops. Specifically, precipitates could have different magnetizations than the surrounding matrix, which is detectable by magnetic measurements. Magnetic hysteresis measurements are made by applying a cyclic magnetic field along the axis of the sample by exciting a coil wound around the sample [101]. Results over increasing neutron fluence showed a similar trend over different RPV materials with a variety of compositions, which were attributed to nanometer-sized defects such as Cu-, Mn-, and/or Ni-rich precipitates, as well as a stress relaxation mechanism due to preferential formation of defects on dislocations, reducing the internal stress of the dislocation [100, 101].

Electric property measurements have also been explored for NDE of radiation damage in RPV materials [86, 106]. Thermo-electric power (TEP) measurements of the Seebeck coefficient are based on a change in voltage due to an applied temperature potential, which is related to the material composition. Defects such as precipitates cause a change in the Seebeck coefficient, although the measurements are also influenced by surface inhomogeneities such as an oxide layer or debris. TEP measurements showed an approximately linear correlation with neutron embrittlement of RPV samples [106, 107]. However, analyses lack a physical interpretation of the influence of microstructural features on the Seebeck coefficient, and the relation to embrittlement relies solely on limited empirical correlations. Measurements of electrical resistivity were also proposed for NDE of radiation damage, but results were not reliable [107].

Ultrasonic velocity measurements have been used to evaluate highly irradiated

stainless steel internal component samples [108]. Internal components are housed inside the RPV and directly surround the fuel in a nuclear reactor, so they receive a much higher dose (at least two orders of magnitude larger) than RPV components. The main contributions to changes in velocity of one study were voids and density changes in the material, which caused changes in the second-order elastic constants of the material [108]. Measurements on highly irradiated stainless steel showed a change in ultrasonic velocity of less than 1.5%, so it is unlikely that ultrasonic velocity will be sensitive to microstructural changes from the much lower irradiations typical of RPV materials. Ultrasonic velocity measurements have also been correlated to porosity and grain size of nuclear fuel in post irradiation tests [109].

Ultrasonic attenuation measurements have been proposed for NDE of radiation damage of RPV steels [110, 111]. Pulse-echo attenuation measurements in an immersion tank were made on broken Charpy samples over a few different levels of neutron fluence. Results showed some small changes in the measured attenuation parameter up to a neutron fluence of 2.6×10^{19}n/cm^2 (E>1 MeV), but large variations in measurements obscured conclusive results. Further, some attenuation coefficients were presented only as an amplitude decrease from an impulse source, which considers the decrease in amplitude of all frequencies combined – since the attenuation coefficient is frequency-dependent, these results are quite questionable.

The NLU technique of second harmonic generation was previously proposed as a technique to detect microstructural changes similar to those produced in radiation damage (namely, copper-rich precipitates), by an investigation of thermal aging of A710 steel, but no investigation was reported beyond the scope of this surrogate material [14]. Research has only recently explored the performance of ultrasonic transducers in an irradiation environment [112], which is crucial for the development of NDE techniques to monitor radiation embrittlement of an RPV.

It is clear that there is not yet a solution for a viable NDE technique to monitor radiation embrittlement in RPV steels to address the pressing concerns of aging nuclear reactors. While magnetic techniques have thus far shown a sensitivity to radiation embrittlement, there are still gaps in relating the measurements to the microstructural changes. An ultrasonic technique with the potential to be scaled to interrogate structures larger than Charpy samples would be of strong interest to the nuclear industry. Further, ultrasonic techniques will likely provide different information that could not be extracted from magnetic techniques, and vice versa, so these techniques could be used as complementary NDE techniques. Since nonlinear ultrasound is a technique known for its sensitivity to microstructural changes, it is a strong candidate for the detection of radiation embrittlement.

3.9 Summary

This chapter provided a review of effects of radiation damage in reactor pressure vessel steels, in terms of microstructural and macroscopic material changes, due to a variety of operating conditions (neutron fluence, flux, irradiation temperature) and depending on material compositions. Nuclear reactors throughout the US have either reached or are close to the end of their operational design lifetime of 40 years. Since the RPV is not a structure that can be replaced, operational licenses of nuclear reactors are being extended for another 20 years, and there is a potential for even longer extensions. So, it is of strong interest to the US Department of Energy and the nuclear industry to develop a nondestructive evaluation method to determine the amount of radiation-induced embrittlement in the RPV. Further, inevitable depletion of surveillance samples is evidence of the need of an NDE method, especially if reactors are to operate for another 20-40 years. The following is a summary of key effects of radiation damage in RPV steels under relevant operating conditions:

- Microstructural changes due to radiation damage in RPV steels are mainly the

formation of precipitates (either CRPs in materials with $> 0.1\%$ Cu, or MNPs in materials with $< 0.1\%$ Cu), matrix features (vacancy-solute complexes, dislocation loops, and vacancy clusters), as well as phosphorous segregation to dislocations and formation of phosphide phases.

- Generally, an increase in neutron fluence increases the amount of precipitates and matrix features to form.
- Lower irradiation temperatures promote the formation of matrix defects and precipitates.
- Higher neutron flux slows the rate of formation of CRPs.
- MNPs form at a much slower rate than CRPs, and could potentially be a concern for long–term operation of RPVs.
- Macroscopic changes due to radiation damage in RPV steels are an increase in the ductile to brittle transition temperature, an increase in yield stress, and a decrease in the fracture toughness.
- Post-irradiation annealing can recover the radiation-induced embrittlement, by dissolving some of the precipitates, and causing a coarsening of the remaining precipitates.
- Re-irradiation after PIA generally causes less precipitates to form since the available copper (or other elements) is less than in the unirradiated state, because of the remaining coarsened precipitates. So, the radiation-induced embrittlement is less for the re-irradiated state compared to a purely irradiated state.
- Out of the previously proposed NDE techniques for RPV embrittlement, magnetic property measurements show the most promise, but there are still gaps in relating the measurements to the microstructural changes. Thus, there is a

need for a viable technique to address the embrittlement concerns of the aging nuclear reactors.

CHAPTER IV

ANALYTICAL MODEL DEVELOPMENT

4.1 Overview

This chapter analyzes different potential contributions to β of microstructural features prominent in radiation damage. The derivations presented here are based off the models described in Section 2.3. The main focuses are: (1) the acoustic nonlinearity produced due to a misfit strain of interstitial-type dislocation loops embedded in the material matrix; (2) an extension of the precipitate–pinned dislocation model to account for a distribution of radii of precipitates within the microstructure; (3) limitations of the pinned dislocation models in terms of a limiting number density of precipitates needed in order to effectively pin all dislocations; and (4) a model of the interaction of dislocations with interstitials and the effects on the acoustic nonlinearity parameter. The final section in this chapter will focus on a comparison of different models to assess the relative strength in terms of contribution to the acoustic nonlinearity parameter, with comments on expected dominating features of an irradiated steel microstructure.

4.2 Interstitial-type Dislocation Loops

The irradiated microstructure of steel contains many types of defects. These defects embedded in the surrounding material matrix will produce a local inelastic strain, or *eigenstrain*. The change in nonlinearity parameter from the initial material state due to local strains in the matrix was developed by Cantrell and Yost [33], and is given

as:

$$\beta - \beta_0 = \left(3 - \frac{C_{111}}{C_{11}} - \frac{C_{1111}}{C_{11}} + \frac{C_{111}^2}{C_{11}^2}\right) u_{,11} + \left(3\frac{C_{12}}{C_{11}} - \frac{C_{1112}}{C_{11}} + \frac{C_{12}C_{111}}{C_{11}^2} + \frac{C_{112}C_{111}}{C_{11}^2}\right)(u_{2,2} + u_{3,3}) \tag{40}$$

where the constants C_{ij}, C_{ijk}, and C_{ijkl} are the second and third-order elastic constants referred to the zero-stress state, assuming an isotropic medium, and $u_{i,j}$ are the displacement gradients. It has been shown that interstitial loops are present in the irradiated microstructure [63, 69], and that irradiation-induced clusters of self-interstitial atoms can be described as prismatic dislocation loops [113]. So, this section will consider the effect of strain from a distribution of interstitial loops on the acoustic nonlinearity parameter.

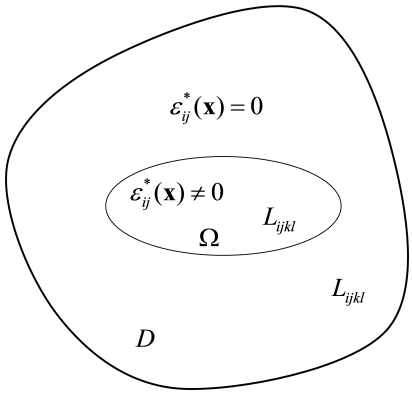

Figure 5: Inclusion embedded in a matrix.

First consider an inclusion of domain Ω embedded in a matrix of a homogeneous, linear elastic material of domain D, such that $\Omega \in D$, see Figure 5 [114]. This inclusion has a prescribed eigenstrain (i.e. inelastic strain or misfit strain) ε_{ij}^*, so from Hookes law the stress over domain D can be written as:

$$\sigma_{ij} = \begin{cases} L_{ijkl}\left(\varepsilon_{kl} - \varepsilon_{kl}^*\right) & \text{for } x \in \Omega \\ L_{ijkl}\varepsilon_{kl} & \text{for } x \in D - \Omega \end{cases}$$

where is the elastic stiffness tensor, and is the total strain field. To find the relationship between the eigenstrain and total strain, consider the average stress field over

D, which should vanish since the boundary is traction-free, i.e.

$$D\bar{\sigma}_{ij} = \int_D \sigma_{ij} dV = \int_\Omega L_{ijkl} \left(\varepsilon_{kl} - \varepsilon^*_{kl}\right) dV + \int_D L_{ijkl}\varepsilon_{kl} = 0 \ . \tag{41}$$

By defining average values for both ε_{ij} and ε^*_{ij} over their respective volume domains, we obtain the relationship:

$$\bar{\varepsilon}_{kl} = \frac{\Omega}{D}\bar{\varepsilon}^*_{kl} \ , \text{ where } \ \bar{\varepsilon}_{kl} = \frac{1}{D}\int_D \varepsilon_{kl} dV \ , \text{ and } \ \bar{\varepsilon}^*_{kl} = \frac{1}{\Omega}\int_\Omega \varepsilon^*_{kl} dV \tag{42}$$

Now consider a specific type of inclusion a prismatic dislocation loop that is either interstitial or vacancy in nature. This loop has a surface area of S, burgers vector b that is perpendicular to the loop surface, and normal vector $\mathbf{n}$. The eigenstrain of such a loop can be written as [114]

$$\varepsilon^*_{ij} = bn_i n_j \delta_S(\mathbf{S} - \mathbf{x}) \text{ , where } \ \delta_S(\mathbf{S} - \mathbf{x}) = \int_S (\mathbf{x} - \mathbf{y}) dS_y \ \ , \tag{43}$$

where $\delta_S(\mathbf{S} - \mathbf{x})$ is the area Dirac delta function. The average eigenstrain can be found by integrating Equation 42 over the area of the loop:

$$\bar{\varepsilon}^*_{ij} = \frac{1}{\Omega}\int_\Omega bn_i n_j \delta_S(\mathbf{S} - \mathbf{x}) dV = \frac{Sb}{\Omega} n_i n_j \ \ . \tag{44}$$

By defining the volume fraction of the dislocation loop as $f_L = Sb/D$ and utilizing Equation 42, the total strain can be written as:

$$\bar{\varepsilon}_{ij} = f_L n_i n_j \ \ . \tag{45}$$

Consider a dilute distribution of prismatic loops, so it can be assumed that the loops are far enough apart such that their interactions can be neglected. For ease of integration, we write the normal vector $\mathbf{n}$ in terms of spherical coordinates $0 < \theta < 2\pi$ and $0 < \varphi < \pi$ such that $\mathbf{n} = (\cos\theta \sin\varphi, \sin\theta \sin\varphi, \cos\varphi)$. So, the total averaged strain from this distribution is simply the superposition of the strain from each individual loop, which can be generally written as an integral that includes the probability density function, $p(\theta, \varphi)$, for loops:

$$\bar{\varepsilon}_{ij} = \int f_L(\theta, \varphi) n_i(\theta, \varphi) n_j(\theta, \varphi) p(\theta, \varphi) \sin\varphi d\theta d\varphi \ \ , \tag{46}$$

where $f_L(\theta, \varphi)$ is the volume fraction of loops, and the probability density function must satisfy:

$$\int p(\theta, \varphi) \sin \varphi d\theta d\varphi = 1 \quad . \tag{47}$$

Irradiation-induced dislocation loops in ferritic steel can be assumed to have approximately the same volume $V_L = Sb$ [63], and we will assume a fully random distribution of loop orientation. By solving for p in Equation 47 we obtain $p(\theta, \varphi) = 1/(4\pi)$, and the volume fraction simply becomes the total volume fraction of all loops, $f_L(\theta, \varphi) = \bar{f}_L = \rho Sb$, where ρ is the number density of dislocation loops in m^3. Using this result, we obtain the final expression for the total strain induced by a dilute distribution of dislocation loops:

$$\bar{\varepsilon}_{ij} = f_L \delta_{ij} \quad . \tag{48}$$

Assuming small strains, we can substitute this expression into Equation 40 to obtain the relationship between β and the strain due to interstitial-type dislocation loops:

$$\beta - \beta_0 = 6 f_L \quad . \tag{49}$$

It is thus expected that β will increase linearly with volume fraction of dislocation loops. It has been reported in the literature that dislocation loop number density increases with radiation dose and saturates at about 1-2 dpa, and loop size also increases with dose saturating at roughly 3-5 dpa [69]. So, it is expected that β will increase with dose and saturate at a few dpa. However, according to TEM measurements in [63], number densities of dislocation loops were about $3 - 7 \times 10^{21}$ $/m^3$, with an average diameter of $3 - 6$ nm, for low-alloy steels irradiated up to levels of neutron fluence similar to what were considered in experiments in this work ($\approx 1.25 \times 10^{20}$ n/cm^2 E > 1 MeV in [63]). This means that the volume fraction of loops is on the order of 10^{-5}, so the change in β will be orders of magnitude lower than the measurement sensitivity. So, it is expected that strain due to interstitial-type dislocation loops will not cause any significant changes on the measured β due

to irradiation.

4.3 Distribution of Precipitate Size

4.3.1 Model Development

It has been shown that radiation damage causes precipitates to form, with a distribution of radii, for example in [52]. Since $\Delta\beta_{ppd}$ depends strongly on the precipitate radius, specifically $\Delta\beta_{ppd} \propto r^4$, it is expected that considering a distribution of precipitate sizes instead of using purely the average radius of precipitates will provide a more accurate representation of $\Delta\beta_{ppd}$. The change in the acoustic nonlinearity parameter, $\Delta\beta$ due to precipitate pinned dislocations, with average precipitate radius $\bar{r}$ and total volume fraction f_{tot}, has been derived as:

$$\Delta\beta = 495\frac{\Lambda\Omega R^3 E_1^2 \left|\delta\right|}{G^3 b^2}\left[\frac{3B}{3B+4G}\right]\frac{\bar{r}^4}{f_{tot}^{1/3}} = C\frac{\bar{r}^4}{f_{tot}^{1/3}} \tag{50}$$

where the parameter C accounts for all variables that are independent of precipitate radius over microstructural evolution, and where f_{tot} is the total volume fraction of precipitates, and $\bar{r}$ is the mean radius of precipitates. The change in acoustic nonlinearity parameter due to a distribution of precipitate radii is defined as

$$\Delta\bar{\beta} = \int p(r)\Delta\beta(r)\,\mathrm{d}r \tag{51}$$

where $\Delta\beta(r)$ is the change in β due to precipitates of radius r and is defined here as

$$\Delta\beta(r) = C\frac{r^4}{\left[f(r)\right]^{1/3}} \tag{52}$$

and $f(r)$ is the volume fraction of precipitates of radius r. The function $p(r)$ is the probability density function of the precipitate radius that defines the volume fraction of precipitates at different radii. It is assumed the precipitate radius has a standard normal distribution of

$$p(r) = \frac{1}{\sigma\sqrt{2\pi}}\exp\left[\frac{-(r-\bar{r})^2}{2\sigma^2}\right] \tag{53}$$

where σ is the standard deviation of radius of precipitates. Note that $p(r)$ can also be written as

$$p(r) = \frac{f(r)}{f_{tot}} \tag{54}$$

Substituting equations 52 and 54 into equation 51, we obtain

$$\Delta\bar{\beta} = C \int \frac{f(r)}{f_{tot}} \frac{r^4}{\left[f(r)\right]^{1/3}} \, \mathrm{d}r = \frac{C}{f_{tot}} \int \left[f(r)\right]^{2/3} r^4 \, \mathrm{d}r \tag{55}$$

Now writing equation 55 in terms of $p(r)$ as defined in equation 54, we obtain

$$\Delta\bar{\beta} = \frac{C}{f_{tot}} \int \left[p(r) f_{tot}\right]^{2/3} r^4 \, \mathrm{d}r = \frac{C}{f_{tot}^{1/3}} \int \left[p(r)\right]^{2/3} r^4 \, \mathrm{d}r \tag{56}$$

Using the definition of $p(r)$ from equation 53:

$$\Delta\bar{\beta} = \left(\frac{C^3}{2\pi\sigma^2 f_{tot}}\right)^{1/3} \int \exp\left[-\frac{(r-\bar{r})^2}{3\sigma^2}\right] r^4 \, \mathrm{d}r = \left(\frac{C^3}{2\pi\sigma^2 f_{tot}}\right)^{1/3} I \tag{57}$$

This integral, I, can be reduced to a usable form using a change in variables of $y = \frac{r-\bar{r}}{\sqrt{3}\sigma}$ with $\mathrm{d}r = \sqrt{3}\sigma \, \mathrm{d}y$:

$$I = a \int e^{-y^2} \left(ay + \bar{r}\right)^4 \, \mathrm{d}y \tag{58}$$

where the substitution $a = \sqrt{3}\sigma$ has also been used. The explicit solution for this indefinite integral is found to be:

$$\begin{aligned} I = & \frac{a}{8} e^{-y^2} \Big\{ \sqrt{\pi} e^{y^2} \left(3a^4 + 12a^2\bar{r}^2 + 4\bar{r}^4\right) \mathrm{erf}(y) \\ & - 2a \left[a^3 y \left(2y^2 + 3\right) + 8a^2\bar{r} \left(y^2 + 1\right) + 12a\bar{r}^2 y + 8\bar{r}^3\right] \Big\} \end{aligned} \tag{59}$$

The bounds on y are taken such that $0 < r < \bar{r} + 4\sigma$, and using the change in variables the integral should thus be evaluated between $y_{min} = -\frac{\bar{r}}{a}$ and $y_{max} = \frac{4\sigma}{a}$. The full solution can then be written as:

$$\Delta\bar{\beta} = \left(\frac{C^3}{2\pi\sigma^2 f_{tot}}\right)^{1/3} I \Big|_{y_{min}}^{y_{max}} \tag{60}$$

4.3.2 Numerical Study of Precipitate Distribution

A simple numerical study can be done using the model for contribution of a distribution of precipitate sizes to the acoustic nonlinearity parameter. Consider a typical precipitate size distribution profile of precipitates in two different RPV steels (here, JRQ and JFL – the reader is referred to Chapter 7 for further information on these materials) measured by small angle neutron scattering (SANS), as shown in Figure 6 [52]. These precipitate size distribution curves were measured over different levels of neutron dose (dpa), where essentially the number density of precipitates increased with increasing dose. The results of the change in the acoustic nonlinearity parameter over increasing neutron dose (dpa) are shown in Figure 7, where $\Delta\beta$ is shown for the model using the average precipitate radius, and the model for the distribution of precipitate sizes. The results show that β decreases with increasing dose, since β is inversely related to the number density of precipitates i.e. $\beta \propto N^{-1/3}$. Depending on the distribution, taking into account the distribution of precipitates causes an increase of approximately two times in the predicted change in β.

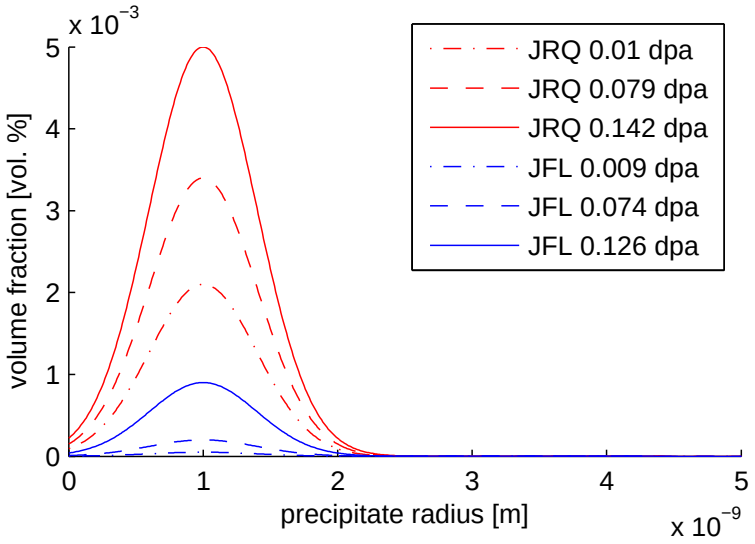

Figure 6: Distribution of precipitates assuming a Gaussian distribution and using volume fraction and average radius values (from Ulbricht et. al 2005).

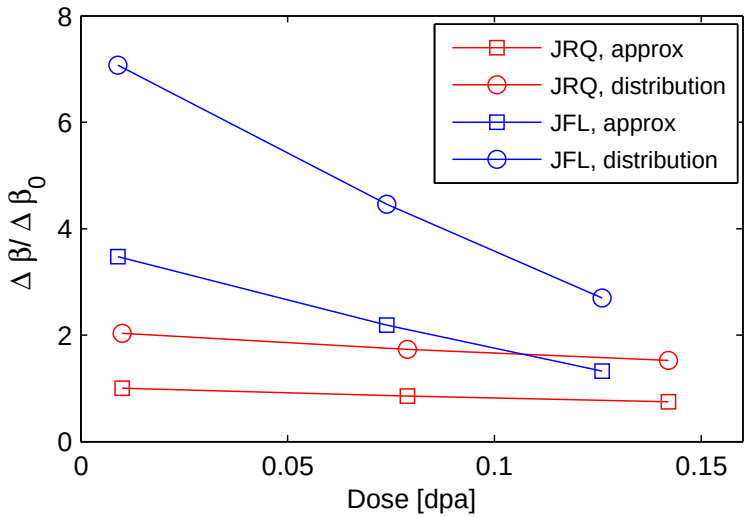

Figure 7: Change in β due to precipitate-pinned dislocations, calculated using average radius values and using a distribution of precipitate sizes.

4.4 Intersection of Dislocation Pinning Models

This section explores the intersection of the dislocation pinning model with the precipitate–pinned dislocation model [115]. Both models describe the change in magnitude of the acoustic nonlinearity parameter due to pinned dislocation segment. The precipitate–pinned dislocation model assumes, clearly, that a distribution of precipitates pins the dislocation segments, and the pure dislocation pinning model considers more general pinning points that are likely grain boundaries, other dislocations, or potentially other defects in the material.

However, there should be some critical number density of precipitates, N_{cr}, only above which this precipitate–pinned dislocation contribution to β applies. The critical density corresponds to the density when all dislocations are pinned at least once in their lengths and therefore it is a constant multiple of the initial dislocation density. Above this critical density, additional precipitates will only shorten the lengths of the already pinned dislocation segments. Therefore, the evolution of β is likely to follow some combination of the general dislocation pinning model (Equation 22) and the

precipitate-pinned dislocation model (Equation 28), which can be expressed as:

$$\Delta\beta \approx (1-\alpha)\,\Lambda L_0^4 \sigma_0 + \alpha\Lambda \frac{\overline{r_p^3}}{N^{1/3}} \tag{61}$$

where α represents the probability of forming the 3–precipitate cluster to bend an existing dislocation segment. This probability is close to zero at very low precipitate density, and is assumed to rapidly increase to 1 at N_{cr}. It is expected that α increases exponentially to 1 because the probability of an additional precipitate to interact with a dislocation depends on the precipitate concentration at the moment when the additional precipitate is added. Further, once the precipitate number density reaches N_{cr}, the chance for any additional nucleated precipitate to interact with a dislocation is 100%. In this way, it is assumed the probability follows Boltzmann statistics, which represents the chance of a group of precipitates to form a specific configuration near a dislocation line, such that $\alpha = \exp(-B/N)$, where B is a positive number representing the precipitate configurational entropy, and N is the current precipitate number density. This formulation is borrowed directly from statistical mechanics. The configurational entropy of a system is related to the number of possible arrangements of particles within the system. . The parameter α is also equivalent to the volume fraction of precipitate–pinned dislocation segments, such that the term $(1-\alpha)$ represents the volume fraction of dislocations pinned by other features (e.g. grain boundaries, or other dislocations). Note that both the general model of pinned dislocations (Equation 22) and the model of precipitate–pinned dislocations (Equation 28) cannot apply at the same time to the same dislocation segment - if a dislocation segment is pinned by two precipitates, that same segment cannot also be pinned by other features. It is expected that the first term in Equation 61 would dominate the behavior of β in the initial stages of radiation damage when precipitates are beginning to form. Then, as the number density of precipitates increases close to the N_{cr}, the second term in Equation 61 would dominate the trend of β.

4.5 Dislocation-interstitial row interactions

Interstitial atoms tend to collect at the core of the an edge dislocation (i.e. end of a dislocation half–plane), since this is the area of lowest energy [20]. It is likely that such a formation can occur during radiation damage – that interstitials preferentially migrate to dislocations. These interstitials would then lock the dislocations and cause hardening since a higher stress would be required to move the dislocation.

In fact, it has been shown in some RPV materials during radiation damage that phosphorous segregates to dislocations [46, 47, 49, 56, 59]. Radiation-enhanced diffusion promotes accelerated phosphorous diffusion and nucleation of phosphide phases due to its low solubility in RPV steels, even though P is typically found in very small quantities (<0.05 wt.%) [46, 56]. Atom probe tomography has shown significant segregation of P, as well as Mn, to dislocations in Fe-P-Mn ternary model alloys [46]. Further, dislocation loops have also been shown with TEM to form preferentially near dislocation lines [63]. So, this section will explore the effect of interstitial atom segregation to dislocations on the acoustic nonlinearity parameter.

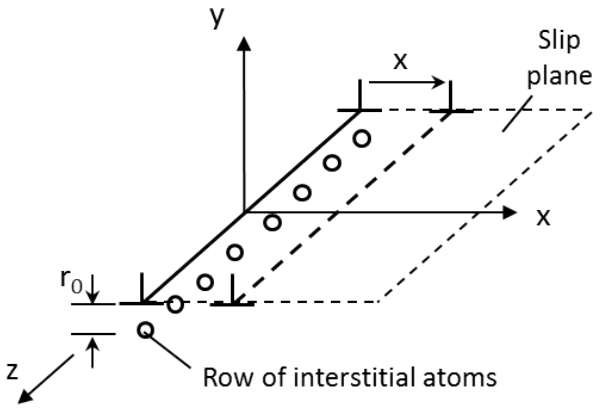

Figure 8: Diagrams of row of interstitial atoms at edge of half–plane of edge dislocation, illustrating movement of the dislocation along the slip plane given some applied shear stress (based off of diagram on pg. 209 in Bacon and Hull, *Introduction to Dislocations*).

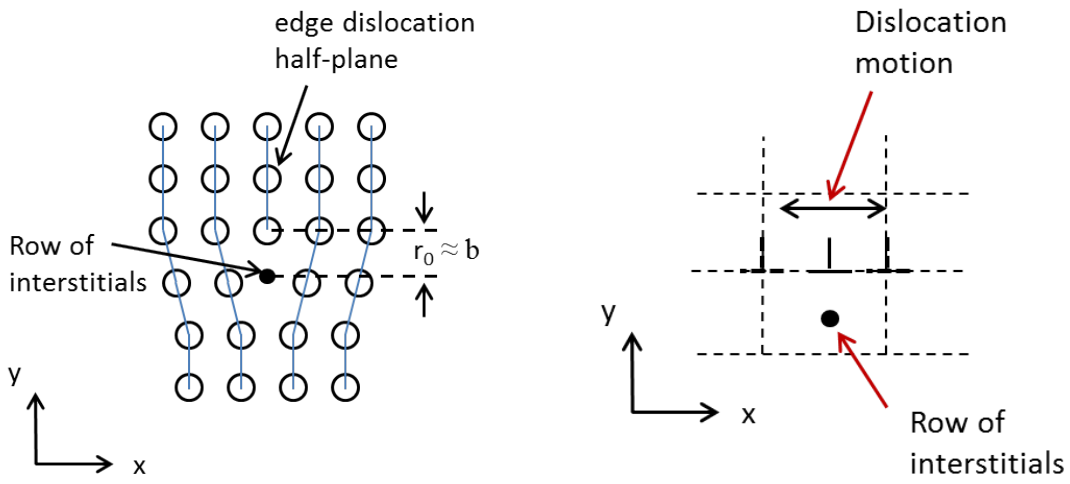

(a) (b)

Figure 9: (a) Diagram in x-y plane of row of interstitial atoms at edge of half–plane of edge dislocation, and (b) diagram in x-y plane showing dislocation movement trapped by interstitial row.

4.5.1 Derivation of Displacement

Consider a row of interstitial atoms located a distance r_0 in the y–direction from an edge dislocation, as depicted in Figures 8 [20] and 9a, and assume the core sites are saturated, i.e. every defect site along the dislocation core is occupied by an interstitial. The force in the x–direction, $F(x)$, on the dislocation line required to move the dislocation a distance x is [20]:

$$F(x) = -2Gb\Omega_v|\delta|r_0\frac{x}{(x^2 + {r_0}^2)^2} \tag{62}$$

where x is the displacement, G is the shear modulus, b is the Burger's vector, Ω_v is the volume per atom of the interstitials, and δ is the misfit parameter of the interstitials. Since this force–displacement relationship is nonlinear, it is possible that this interaction could contribute to the nonlinearity parameter.

4.5.1.1 Setting up the equations

This derivation will follow the derivation in Cantrell's chapter in Kundu's *Ultrasonic Nondestructive Evaluation* [12] for nonlinearity due to dislocation dipoles, but modified for dislocation-interstitial interactions. Cantrell assumes the equation of motion for a longitudinal wave propagating through an isotropic solid as:

$$\rho_0 \left(\frac{\partial^2 u}{\partial t^2} \right) = \frac{\partial \sigma}{\partial X} \tag{63}$$

where ρ_0 is the density, u is the total longitudinal wave displacement, σ is the stress, and X is the spatial coordinate and direction of wave propagation. In the current case, the displacement u will have a lattice contribution u_l and dislocation–interstitial contribution u_{di}:

$$u = u_l + u_{di} \tag{64}$$

such that the equation of motion becomes:

$$\rho_0 \frac{\partial^2}{\partial t^2} \left(\frac{\partial u_l}{\partial X} + \frac{\partial u_{di}}{\partial X} \right) = \frac{\partial^2 \sigma}{\partial X^2} \tag{65}$$

We assume the stress can be expressed as:

$$\sigma = \sigma_1 + B_1 \cos(\omega t - kX) + B_2 \cos 2(\omega t - kX) + C_2 \sin 2(\omega t - kX) \tag{66}$$

The purpose of the following derivation will be to develop an expression for $\frac{\partial u_{di}}{\partial X}$, to use in equation 65, to model the wave propagation and ultimately develop an expression for the second harmonic amplitudes B_2 and C_2. It is assumed that amplitude B_1 remains constant with propagation distance. The second harmonic amplitudes are functions of distance such that $B_2 = B_2(X)$ and $C_2 = C_2(X)$, and satisfy the boundary conditions

$$B_2(0) = C_2(0) = 0 \ . \tag{67}$$

These solutions will then be used to develop an expression for β due to dislocation–interstitial row interactions.

4.5.1.2 Relation of ultrasonic displacement to dislocation displacement

This derivation follows the method of derivation presented in section 6.3.3.1 in [12] for dislocation dipole contribution to the nonlinearity parameter. Dislocation motion creates a plastic strain, which can be derived as follows. Consider a volume of crystal with edge dislocations with an applied shear stress, as depicted in Figure 10. The shear stress causes the dislocations to displace along the slip plane, such that the top surface of the crystal volume will displace relative to the bottom surface. If a dislocation displaces the entire length in the x-direction of this volume for a total distance of d, the top surface will be displaced by a distance equal to the Burgers vector, b. If the dislocation only displaces through a portion of this total distance, say x_i, the displacement of the top surface relative to the bottom surface of the crystal will be $(x_i/d)b$. The total displacement, D, for a volume of N mobile dislocations will then be:

$$D = \frac{b}{d}\sum_{i=1}^{N} x_i \tag{68}$$

The plastic strain, γ_{di}, resulting from the displacement of these dislocations can then be written as:

$$\gamma_{di} = \frac{D}{h} = \frac{bN\bar{x}}{hd} = \Lambda_{di} b\bar{x} \tag{69}$$

where h is the height of the crystal volume, $\bar{x}$ is the average displacement by the dislocations, and $\Lambda_{di} = N/(hd)$ is the density of mobile dislocation–interstitial row pairs, in units of $1/m^2$. This density of dislocation–interstitial row pairs can be expressed as $\Lambda_{di} = \alpha\Lambda_d$, where Λ_d is the dislocation density and α is a factor that accounts for percentage of dislocations trapped by interstitial rows, such that $0 \leq \alpha \leq 1$. If $\alpha = 0$, then no dislocations are trapped by interstitial rows, and if $\alpha = 1$, then all dislocations are trapped by interstitial rows. The relation between the plastic strain from dislocation motion and ultrasonic wave displacement due to dislocation

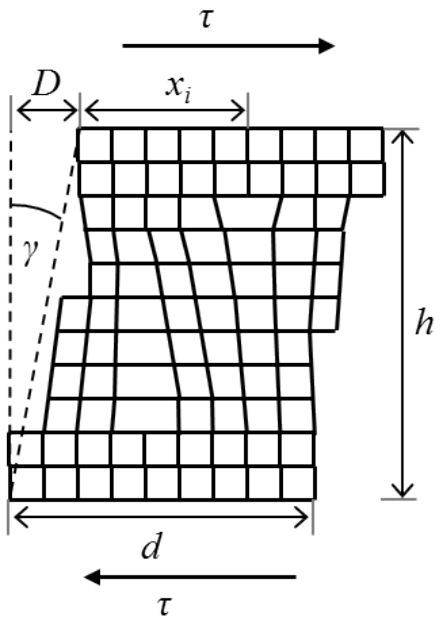

Figure 10: Geometry of dislocation motion along slip plane in a volume of a crystal.

motion is:

$$\frac{\partial u_{di}}{\partial X} = \Omega \gamma_{di} = \Omega \Lambda_{di} b x \tag{70}$$

where Ω here is the conversion from displacement in the slip plane to the longitudinal displacement u_{di}. *The purpose of the following section will be to develop an equation for x, the dislocation displacement, to relate back to the longitudinal wave displacement, u.*

4.5.1.3 Equation of Motion

The equation of motion for the dislocation–interstitial row pair given some applied stress σ is:

$$m\frac{\partial^2 x}{\partial t^2} = \frac{F(x)}{b} + b\sigma R \tag{71}$$

where x is the displacement of the dislocation, m is the effective combined mass of the dislocation–interstitial row per unit length (on the order $\rho_0 b^2$), and R is the conversion factor from the longitudinal displacement in the direction of wave propagation to displacement of the dislocation along its slip plane. Note that the two terms on the

right-hand side of Equation 71 are normalized with b such each expression is in units of a force per unit length, since we are using a mass per unit length for the trapped dislocations. We assume $r_0 \approx b$, and while this is not an exact expression and r is likely less than b, this serves as a good approximation. Assuming small displacements, the force from equation (62) can be approximated with the Taylor expansion of x:

$$F(x) \approx -2G\Omega_v|\delta| \left(\frac{x}{b^2} - \frac{2x^3}{b^4} \right) \tag{72}$$

4.5.1.4 Solving the equation of motion for dislocation-interstitial row

Substituting equation (72) into equation (71), the equation of motion becomes:

$$m\frac{\partial^2 x}{\partial t^2} + \frac{2G\Omega_v|\delta|}{b} \left(\frac{x}{b^2} - \frac{2x^3}{b^4} \right) = b\sigma R \tag{73}$$

and assuming the stress σ is of the form given in equation (66). The solution to equations 73 and 66 is determined with an iterative procedure, as in [12]. First solve for the linear solution x_1, by considering only first-order terms in the equation for force (equation (72)), and approximating stress without the second harmonic terms. The differential equation for x_1 is then

$$m\frac{\partial^2 x_1}{\partial t^2} + 2G\Omega_v|\delta|\frac{x_1}{b^3} = bR\left[\sigma_1 + B_1\cos\left(\omega t - kX\right)\right] \quad . \tag{74}$$

The solution to this equation is:

$$x_1 = \frac{b^4 R\sigma_1}{2G\Omega_v|\delta|} - \frac{b^4 RB_1}{m\omega^2 b^3 + 2G\Omega_v|\delta|}\cos\left(\omega t - kX\right) \quad . \tag{75}$$

The term $m\omega^2 b^3$ in the denominator of the second term of equation (75) is much smaller compared to the second term $2G\Omega_v\delta$ for ultrasonic frequencies of interest ($\sim 10^6$ Hz), and can be neglected. The solution then reduces to:

$$x_1 = \frac{b^4 R\sigma_1}{2G\Omega_v|\delta|} - \frac{b^4 RB_1}{2G\Omega_v|\delta|}\cos\left(\omega t - kX\right) = a\sigma_1 + aB_1\cos\left(\omega t - kX\right) \quad , \tag{76}$$

where the variable a has been introduced for simplicity and is defined as:

$$a = \frac{b^4 R}{2G\Omega_v|\delta|} \quad . \tag{77}$$

To find the approximate solution to the full nonlinear equation of motion, the solution for x_1 is then substituted for x in the higher-order term (x^3 term) in equation (73) and the full expression for stress is used. The final equation to solve is:

$$m\frac{\partial^2 x}{\partial t^2} + \frac{2G\Omega_v|\delta|}{b^3}x - \frac{4G\Omega_v|\delta|}{b^5}x_1^3 = bR\left[\sigma_1 + B_1\cos(\omega t - kX)\right. \\ \left. + B_2\cos 2(\omega t - kX) + C_2\sin 2(\omega t - kX)\right] \ . \tag{78}$$

The expression for x_1^3 is written out in full:

$$\begin{aligned} x_1^3 =& \sigma_1^3 a^3 + B_1^3 a^3\cos^3(\omega t - kX) + 3B_1^2\sigma_1 a^3\cos^2(\omega t - kX) \\ &+ 3B_1\sigma_1^2 a^3\cos(\omega t - kX) \ , \end{aligned} \tag{79}$$

where $\cos^2(u)$ and $\cos^3(u)$ components can be expanded into $\cos(u)$, $\cos(2u)$, and $\cos(3u)$ components. The solution to equation 78 is

$$\begin{aligned} x = & \left[\frac{2a^3}{b^2}\left(\sigma_1^3 + \frac{3}{2}\sigma_1 B_1^2\right) + a\sigma_1\right] \\ & + \left[\frac{2a^3}{b^2}\left(3\sigma_1^2 B_1 + \frac{3}{4}B_1^3\right) + aB_1\right]\cos(\omega t - kX) \\ & + \left[\frac{3a^3}{b^2}\sigma_1 B_1^2 + aB_2\right]\cos 2(\omega t - kX) \\ & + aC_2\sin 2(\omega t - kX) \ , \end{aligned} \tag{80}$$

where harmonics higher than the third are neglected. To summarize, equation (80) represents an approximate solution to the equation of dislocation motion from equation (73). The desired relation for $\frac{\partial u_{di}}{\partial X}$ can now be written using equations (70) and

(80) as:

$$\begin{aligned}\frac{\partial u_{di}}{\partial X} &= \Omega\Lambda_{di}bx \\ &= \Omega\Lambda_{di}b\left[\frac{2a^3}{b^2}\left(\sigma_1^3+\frac{3}{2}\sigma_1 B_1^2\right)+a\sigma_1\right] \\ &+ \Omega\Lambda_{di}b\left[\frac{2a^3}{b^2}\left(3\sigma_1^2 B_1+\frac{3}{4}B_1^3\right)+aB_1\right]\cos\left(\omega t-kX\right) \\ &+ \Omega\Lambda_{di}b\left[\frac{3a^3}{b^2}\sigma_1 B_1^2+aB_2\right]\cos 2\left(\omega t-kX\right) \\ &+ \Omega\Lambda_{di}baC_2\sin 2\left(\omega t-kX\right) \quad , \end{aligned} \tag{81}$$

4.5.2 Lattice Contribution to the Second Harmonic Wave

The solution for the lattice contribution to the ultrasonic wave displacement is derived elsewhere [12] and is reproduced here as:

$$\begin{aligned}\frac{\partial u_l}{\partial X} &= \left(\frac{\sigma_1}{A_{11}}-\frac{1}{4}\frac{A_{111}B_1^2}{A_{11}^3}-\frac{1}{2}\frac{A_{111}\sigma_1^2}{A_{11}^3}\right) \\ &+ \left(\frac{B_1}{A_{11}}-\frac{A_{111}B_1\sigma_1}{A_{11}^3}\right)\cos(\omega t-kX) \\ &+ \left(\frac{B_2}{A_{11}}-\frac{1}{4}\frac{A_{111}B_1^2}{A_{11}^3}\right)\cos 2(\omega t-kX) \\ &+ \left(\frac{C_2}{A_{11}}\right)\sin 2(\omega t-kX) \quad . \end{aligned} \tag{82}$$

4.5.3 Solution for Second Harmonic Wave Amplitude

The full (approximate) solution for equation (65), reproduced here as

$$\rho_0\frac{\partial}{\partial t^2}\left(\frac{\partial u_l}{\partial X}+\frac{\partial u_{di}}{\partial X}\right)=\frac{\partial^2\sigma}{\partial X^2} \quad ,$$

is now derived, by using equations (66), (81), and (82). Assuming the fundamental amplitude B_1 is constant with propagation distance X, and all amplitude terms are time-independent, these equations result in the coupled differential equations:

$$4k\frac{\partial C_2}{\partial X}-\frac{\partial^2 B_2}{\partial X^2}=\left[4aA_{11}k^2\Omega\Lambda_{di}b\right]B_2+\left[\frac{12A_{11}k^2\Omega\Lambda_{di}a^3\sigma_1}{b}-\frac{k^2A_{111}}{A_{11}^2}\right]B_1^2 \tag{83}$$

and

$$\frac{\partial^2 C_2}{\partial X^2} + 4k\frac{\partial B_2}{\partial X} + \left[4aA_{11}k^2\Omega\Lambda_{di}b\right]C_2 = 0 \quad , \tag{84}$$

where the relation $A_{11} = \frac{\rho_0\omega^2}{k^2}$ has been used to simplify the equations. A solution to equations (83), (84), and boundary conditions given in equation (67) is found by assuming $B_2 = d_1 X$ and solving for d_1 to obtain B_2 and C_2. For clarity's sake, equations (83) and (84) are written in a simpler form:

$$4k\frac{\partial C_2}{\partial X} - \frac{\partial^2 B_2}{\partial X^2} = f_1 B_2 + f_2 B_1^2 \tag{85}$$

and

$$\frac{\partial^2 C_2}{\partial X^2} + 4k\frac{\partial B_2}{\partial X} + f_1 C_2 = 0 \tag{86}$$

where

$$f_1 = 4aA_{11}k^2\Omega\Lambda_{di}b \quad \text{and} \quad f_2 = \frac{12A_{11}k^2\Omega\Lambda_{di}a^3\sigma_1}{b} - \frac{k^2 A_{111}}{A_{11}^2} \tag{87}$$

Solving these equations we find the following solutions for B_2 and C_2:

$$B_2 = \frac{-f_1 f_2 B_1^2}{2f_1 + 32k^2 + f_1^2 X^2}X^2 \tag{88}$$

and

$$C_2 = \frac{f_2 B_1^2}{4k}X - \frac{f_1^2 f_2 B_1^2}{8k\left(2f_1 + 32k^2 + f_1^2 X^2\right)}X^3 \tag{89}$$

Note that all coefficients of X for B_2 and C_2 are of the same order of magnitude. So, assuming small propagation distances for nonlinear ultrasonic measurements, B_2 and C_2 can be written in terms of their first order linear approximation, as:

$$B_2 \approx 0 \tag{90}$$

and

$$C_2 \approx \frac{f_2 B_1^2}{4k}X = \frac{B_1^2 kX}{4A_{11}}\left[\frac{12A_{11}^2\Omega\Lambda_{di}a^3\sigma_1}{b} - \frac{A_{111}}{A_{11}}\right] \quad . \tag{91}$$

Writing this in terms of $\beta_{lat} = -A_{111}/A_{11}$, the equation for C_2 becomes:

$$C_2 = \frac{B_1^2 kX}{4A_{11}}\left[\frac{12A_{11}^2\Omega\Lambda_{di}a^3\sigma_1}{b} + \beta_{lat}\right] \quad . \tag{92}$$

4.5.4 Solution for the Acoustic Nonlinearity Parameter

The nonlinearity parameter, β is defined as:

$$\beta = 8\frac{C_2'}{k^2 B_1'^2 X} \quad , \tag{93}$$

where B_1' and C_2' are the first and second harmonic displacement amplitudes, respectively. β is defined in terms of displacement amplitudes instead of the stress amplitudes found in the above derivation since typical nonlinear ultrasonic experiments will measure displacement amplitudes. Following [12], the displacement can be approximately related to the stress through the equation:

$$\sigma \approx A_{11}\frac{\partial u}{\partial X} \quad , \tag{94}$$

so that the displacement amplitudes can be expressed as:

$$B_1' = -\frac{B_1}{kA_{11}} \, , \quad \text{and} \quad C_2' = \frac{C_2}{2kA_{11}} \quad . \tag{95}$$

The second harmonic displacement amplitude can then be written as:

$$C_2' = \frac{k^2 B_1'^2 X}{8}\left[\beta_{lat} + \frac{12A_{11}^2\Omega\Lambda_{di}a^3\sigma_1}{b}\right] \quad . \tag{96}$$

Substituting equation (96) into equation (93), we obtain the expression for the total β due to dislocation-interstitial row interactions as:

$$\beta_{total} = \beta_{lat} + \beta_{di} = \beta_{lat} + \frac{12A_{11}^2\Omega\Lambda_{di}a^3\sigma_1}{b} \quad , \tag{97}$$

where the nonlinearity parameter due to dislocation-interstitial interactions, β_{di}, has been defined as:

$$\beta_{di} = \frac{12A_{11}^2\Omega\Lambda_{di}a^3\sigma_1}{b} \quad . \tag{98}$$

The parameter β_{di} is non-dimensional, so this expression is confirmed from a dimensionality argument. Substituting the value for $a = b^4R/(2G\Omega_v|\delta|)$ into Equation 98, we obtain a final expression:

$$\beta_{di} = \frac{3A_{11}^2\Omega\Lambda_{di}R^3b^{11}}{2G^3\Omega_v^3|\delta|^3}\sigma_1 \quad . \tag{99}$$

Note that the stress σ_1 in Equation 99 can be a residual stress in the material, or possibly due to a misfit strain from a distribution of precipitates embedded in the matrix.

4.6 Model Comparisons

This section compares the different models presented above, along with those previously developed and reviewed in Section 2.3, to determine the relative strengths of the models. The purpose of these comparisons is to predict which microstructural features formed during radiation damage of RPV steels may be detectable by nonlinear ultrasound. Radiation damage causes microstructural features such as copper-rich precipitates, precipitates of other compositions, vacancy clusters, solute clusters, phosphorous segregation to dislocations. So, models that consider precipitate, dislocation, vacancy, or interstitial row effects on the nonlinearity parameter are relevant, and models for pinned dislocations, dislocation-interstitial row interactions, precipitate-pinned dislocations, and vacancy contributions to the acoustic nonlinearity parameter will be considered in this section. Further, these comparisons will show which features will dominate in the nonlinear response at different stages of radiation damage.

4.6.1 Dislocation-interstitial row versus pinned dislocations

In this section, we will compare the change in magnitude of β of a microstructure of dislocations to that of dislocations trapped by interstitial rows. Specifically, the microstructures compared in this case are:

1. Microstructure with dislocations

2. Microstructure with dislocations trapped by interstitial rows

In this scenario, we assume the stress on the dislocation segment is the same (i.e. some residual or internal stress), such that the interstitial row does not produce a significant

stress on the dislocation segment. The change in β due to pinned dislocations, $\Delta\beta_{pd}$, has been shown to be:

$$\Delta\beta_{pd} = \frac{24}{5}\frac{\Lambda\Omega R^3 L^4 A_{11}^2}{b^2 G^3}|\sigma| \tag{100}$$

The change in β due to the nonlinear force-displacement relation of a dislocation interacting with an adjacent interstitial row of atoms, $\Delta\beta_{di}$, has been derived as:

$$\Delta\beta_{di} = \frac{3A_{11}^2\Omega R^3\zeta\Lambda b^{11}|\sigma|}{2G^3\Omega_v^3|\delta|^3} \quad . \tag{101}$$

where ζ is the fraction of dislocations interacting with an adjacent interstitial row of atoms.

To investigate the relative strengths of these two effects on nonlinearity, one can compare the case where the microstructure initially has some distribution and density of dislocations, and then interstitial rows are preferentially formed on dislocations. We assume the residual stress σ is the same in both cases such that:

$$\frac{\Delta\beta_{di}}{\Delta\beta_{pd}} = \frac{5\zeta b^{13}}{16\Omega_v^3|\delta|^3 L^4} \tag{102}$$

If we assume that phosphorous atoms occupy the interstitial sites, the atomic volume of a single interstitial can be expressed as $\Omega_v = 4/3\pi r_i^3$, where $r_i \approx 1\times10^{-10}$m and thus $r_i \approx b/2.87$ where b is the Burger's vector in steel. Note that it has been experimentally verified that phosphorous atoms preferentially segregate to dislocations and grain boundaries during radiation damage in RPV steels. Therefore, equation (102) can be simplified to:

$$\frac{\Delta\beta_{di}}{\Delta\beta_{pd}} = \frac{56\zeta}{|\delta|^3}\left(\frac{b}{L}\right)^4 \tag{103}$$

For phosphorous atoms in an Fe matrix, $|\delta| \approx 10^{-2}$, so we can further simplify:

$$\frac{\Delta\beta_{di}}{\Delta\beta_{pd}} = 5.6\times10^7\zeta\left(\frac{b}{L}\right)^4 \tag{104}$$

So, the strength of $\Delta\beta_{di}$ depends strongly on the dislocation loop length. We assume the loop length is roughly proportional to the grain size of the material. For steels, this

is likely on the order of 10^{-5}, and given $b = 2.87 \times 10^{-10}$ m for steel, the ratio b/L is on the order of 10^{-4}. Even for finer grained material and for all dislocations interacting with interstitial rows, the magnitude of $\Delta\beta_{di}$ is still extremely small compared to $\Delta\beta_{pd}$ – on the order of 10^{-10} times smaller. This is likely because the pinning length is so large compared to the relative scale of the dislocation-interstitial separation. Therefore, for a microstructure of purely dislocations, additional interstitial rows interacting with dislocations will not have a significant effect on β.

4.6.2 Dislocation-interstitial row versus precipitate-pinned dislocations

Now consider the case where we start with a distribution of both dislocations and precipitates in the microstructure, then interstitial rows are allowed to form on dislocations. Specifically, the two microstructures compared are:

1. Microstructure with dislocations pinned by precipitates
2. Microstructure with dislocations pinned by precipitates, and interstitial rows trapping dislocations

So the trapped dislocations (by interstitial rows) are also being pinned by precipitates, which create the stress on the dislocation segment. In this case, the form of β due to precipitate-pinned dislocations, the stress σ and loop length L depend on precipitate parameters, such that $\Delta\beta_{ppd}$ can be written as:

$$\Delta\beta_{ppd} = \frac{24}{5}\frac{\Lambda\Omega R^3 L_p^4 A_{11}^2}{b^2 G^3}|\sigma_p| \tag{105}$$

Similarly, the relation for $\Delta\beta_{di}$ can be written in terms of precipitates parameters, such that:

$$\Delta\beta_{di} = \frac{3A_{11}^2\Omega R^3\zeta\Lambda b^{11}|\sigma|}{2G^3\Omega_v^3|\delta|^3} \quad . \tag{106}$$

The stress in both equations (105) and (106) in this case is due to the precipitates embedded in the surrounding matrix, and the ratio of $\frac{\Delta\beta_{di}}{\Delta\beta_{ppd}}$ is the same as that given

in equation (102). The loop length in this case depends on the precipitate spacing. To determine the relation between loop length and precipitate spacing, we can again pull from statistical mechanics which suggests that the average spacing between two non-interacting particles is equal to $L_p = 2r_s$, where $r_s = \left(\frac{3}{4\pi N}\right)^3$ is the Wigner-Seitz radius. This is the radius of a sphere whose volume is equivalent to the average volume of an atom in a solid. Note this definition of L, at least in terms of the volume fraction of precipitates and average precipitate radius, has been used previously to analyze precipitate contribution to β [13]. In terms of the number density of precipitates N, $L_p = 1.24N^{-1/3}$, so the relation can be further reduced to:

$$\frac{\Delta\beta_{di}}{\Delta\beta_{ppd}} \approx 2.4 \times 10^7 \zeta \left(bN^{1/3}\right)^4 \tag{107}$$

So, depending on the total number density of precipitates, the relative magnitude of $\Delta\beta_{di}$ compared to $\Delta\beta_{ppd}$ can be quite large and significant. For $\zeta = 1$ there is a critical number density of precipitates where $\Delta\beta_{di} = \Delta\beta_{ppd}$, where this $N_{cr,2} = 1.2 \times 10^{23}\text{m}^{-3}$. Note that this $N_{cr,2}$ is different than and not related to the critical number density N_{cr} described previously in the intersection of dislocation pinning models.

A plot of the relative magnitudes of $\Delta\beta_{di}$ compared to $\Delta\beta_{ppd}$ is shown in Figure 11 in terms of increasing number density of precipitates. The trend is shown for increasing values of ζ i.e. percent of dislocations interacting with an interstitial row, where "interacting" again means that an interstitial row has segregated to and formed on a dislocation. Figure 12 shows the comparison in terms of increasing ζ, plotted for different constant values of number density of precipitates.

It can be seen in Figures 11 and 12 that the critical number density of precipitates, i.e. $N_{cr,2}$ such that $\Delta\beta_{di} = \Delta\beta_{ppd}$, increases with decreasing ζ. This means that the relative strength of $\Delta\beta_{di}$ increases with increasing amount of dislocations trapped by interstitial rows. Further, increasing the number density of precipitates increases the strength of $\Delta\beta_{di}$ relative to $\Delta\beta_{ppd}$. Note that increasing the radius of precipitates, which increases the stress exerted by the embedded precipitate, increases both $\Delta\beta_{di}$

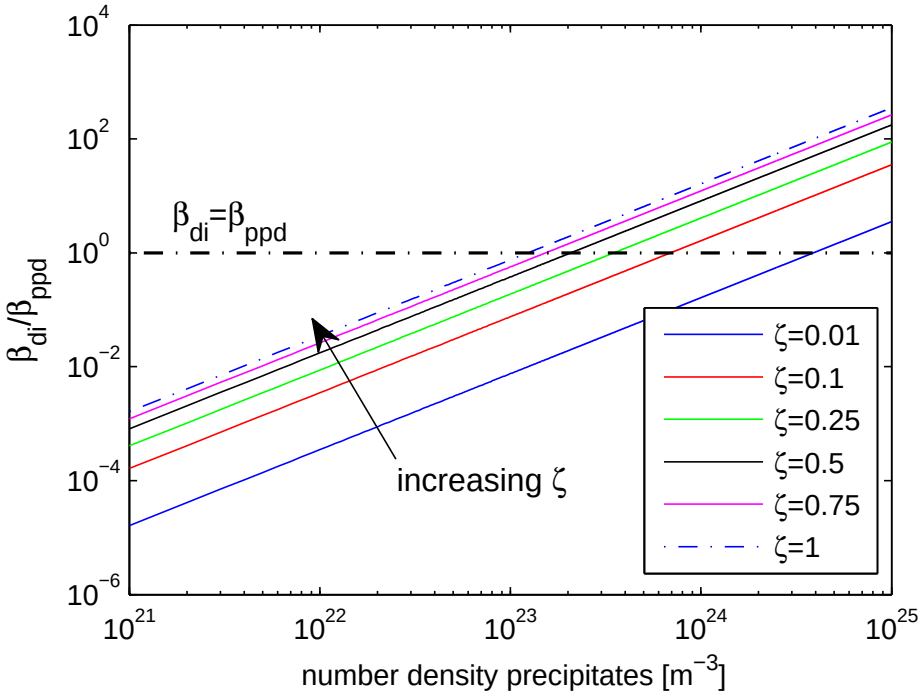

Figure 11: Relative strength of β_{di} and β_{ppd} over increasing number density of precipitates

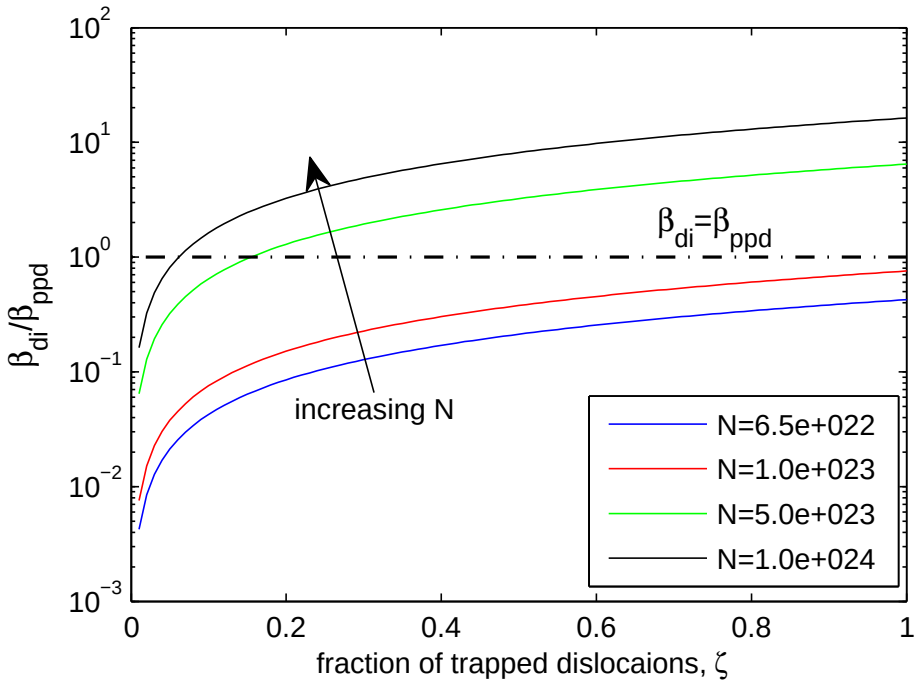

Figure 12: Relative strength of β_{di} and β_{ppd} over increasing values of ζ, the fraction of trapped dislocations.

and $\Delta\beta_{ppd}$, but by the same amount.

4.6.3 Vacancies versus precipitates

The contributions to the acoustic nonlinearity parameter for precipitates and vacancies are given in Equations 105 and 31, respectively. First, we compare the total nonlinearity due to a microstructure with purely vacancies to one of purely precipitates (and dislocations in both cases and scenarios).

In this case, we have a dislocated microstructure with a distribution of precipitates and vacancies. We assume a random distribution such that the loop length in both Equations 105 and 31 is equivalent. Thus, to compare the contribution to β of vacancies compared to precipitates, one need only to look at the difference in stress produced by these microstructural features. The stress due to a vacancy was derived previously as:

$$\sigma_v = \frac{-4G\,(1+\nu)}{3\,(1-\nu)}\frac{r_v^3}{r^3}\delta_v \tag{108}$$

and the stress due to a precipitate was derived as:

$$\sigma_p = \frac{-4G\,(3B_p)}{(3B_p+4G)}\frac{r_p^3}{r^3}\delta_p \tag{109}$$

To evaluate the relative contributions of these two features, the ratio of $|\sigma_v|$ to $|\sigma_p|$ is considered, which reduces to

$$\frac{\sigma_v}{\sigma_p} = \left[\frac{(1+\nu)\,(3B_p+4G)}{9\,(1-\nu)\,B_p}\right]\frac{|\delta_v|}{|\delta_p|}\frac{r_v^3}{r_p^3} \tag{110}$$

In this work we are considering low alloy steel, for which $\nu = 0.33$ and $G \approx 80$ GPa. The misfit parameter for vacancies is known to range from -0.1 to 0, and the radius is $r_v \approx b/2 = 0.1435$ nm. In RPV material, copper precipitates have been shown to form during radiation damage, e.g. [41, 47]. If we assume the precipitate is purely copper (which is generally not realistic), the bulk modulus of the precipitate is thus the bulk modulus of copper, $B_p = 140$ GPa, and the misfit parameter is $\delta_p = 0.024$ [116]. The first bracketed term in Equation 110 representing the material

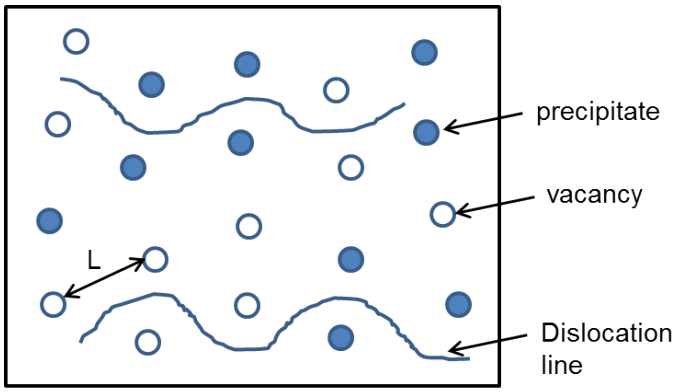

Figure 13: Two-feature pinning model: diagram of dislocation pinning by two different microstructural features, precipitates and vacancies.

properties is not much more than 1 even if the precipitate composition is somewhat softer than copper, and the ratio of the misfit parameters will vary from 0 to 5, depending on the vacancy misfit parameter. However, the ratio in Equation 110 is clearly dominated by the relative ratios of the radii of the vacancies and precipitates. The precipitate radius has been reported to be on the order of 1 nm in irradiated RPV steel, so the ratio $(r_v/r_p)^3$ is on the order of 0.001. So, the precipitate contribution to β will dominate over the vacancy contribution.

4.6.4 Two-Feature Pinning Model

Assume we have a microstructure containing dislocations, and two types of dislocation pinning features, for example vacancies and precipitates. Assume all pinning points are uniformly distributed, such that the distance between pinning points is roughly the same throughout the microstructure. A diagram of this microstructure is depicted in Figure 13, with the particle spacing L indicated. Both features will exert a local stress field in the vicinity of a dislocation segment - σ_p is exerted by the precipitates, and σ_v is exerted by the vacancies.

Assuming we have a number density of precipitates N_p and number density of

vacancies N_v, the average stress on a dislocation segment can be expressed as:

$$\sigma_{avg} = \frac{N_p\sigma_p + N_v\sigma_v}{N_p + N_v} \tag{111}$$

Section 4.6.3 shows that the stress field of a precipitate will likely be much larger than that of a vacancy, due to the larger radius of the precipitate compared to the vacancy. So, replacing some precipitate pinning points by vacancy pinning points will reduce the internal stress acting on the dislocation segment. Recall that the change in β due to dislocation pinning is:

$$\Delta\beta = C\Lambda L^4\sigma \tag{112}$$

where C contains material parameters and can be found by comparing Equation 112 to Equation 100. Therefore, for a constant dislocation pinning length L, replacing precipitate pinning points with vacancies will decrease the total change in β. This approach can be used to determine the total change in β due to multiple types of pinning features.

To further extend Equation 111 to the specific case of precipitates and vacancies as the two pinning features, the average stress can be fully written as:

$$\sigma_{avg} = \frac{-4G}{r^3}\left[\frac{N_v}{(N_p+N_v)}\frac{(1+\nu)}{3(1-\nu)}r_v^3\delta_v + \frac{N_p}{(N_p+N_v)}\frac{3B_p}{3B_p+4G}r_p^3\delta_p\right] \tag{113}$$

To find the change in β due to the average stress on a dislocation segment from a distribution of precipitates and vacancies, we use the same formulation as in Section 2.3.2: we evaluate the stress, σ_{avg} at $L/2$ and assume two precipitates (or vacancies) act on the dislocation segment, such that $|\sigma| = 2\sigma_{avg}(r = L/2)$. The change in β_{pv}, the acoustic nonlinearity due to dislocation pinning by a combination of precipitates and vacancies, becomes:

$$\Delta\beta_{pv} = \frac{1536}{5}\frac{\Omega R^3 C_{11}^2}{G^2b^2}\Lambda L\left[\Gamma_v\frac{(1+\nu)}{3(1-\nu)}r_v^3\delta_v + \Gamma_p\frac{3B_p}{3B_p+4G}r_p^3\delta_p\right] \tag{114}$$

where $\Gamma_v = N_v/(N_p+N_v)$ and $\Gamma_p = N_p/(N_p+N_v)$. With this model, the total change in β due to two types of dislocation pinning features can be calculated.

4.7 Summary

This chapter presents models that determine the effects on the magnitude of the acoustic nonlinearity parameter due to different microstructural features formed throughout radiation damage in RPV steels. These newly-developed models describe the change in β due to a distribution of sizes of precipitates pinning dislocations, which shows current models that consider an average precipitate radius under–predict the change in magnitude of β. Another model provides a hypothesis for a critical number density of precipitates to pin dislocations and influence the magnitude of acoustic nonlinearity parameter, by considering the intersection of the general dislocation pinning theory and that of the precipitate-pinned dislocation theory. Further, a model is developed that provides theoretical evidence for the contribution of interstitial row segregation to dislocations to the magnitude of β.

By comparing these models with each other and previously developed models, the following conclusions can be drawn about the relative influence of different microstructural features formed in radiation damage in RPV steels on the magnitude of β:

- Beyond a critical number density of precipitates, which positively depends on the percentage of dislocations interaction with interstitial rows, the relative magnitude of $\Delta\beta_{di}$ will dominate that of $\Delta\beta_{ppd}$.

- If few or no precipitates are present in a microstructure, the effect on β of dislocations interacting with an interstitial row will be negligible compared to pinned dislocations (by grain boundaries, other dislocations, point defects, etc.).

- Precipitate contribution to the magnitude of β will dominate over the contribution of vacancies of a similar number density.

CHAPTER V

EXPERIMENTAL METHODS

5.1 Overview

Second harmonic generation measurements of the acoustic nonlinearity parameter can be conducted using multiple wave types, different generation and detection methods, and experimental set-ups. The general process is similar in all cases, where an ultrasonic tone burst at frequency ω is generated in the material, propagates some distance through the material or structure, and the response – amplitudes of the first harmonic and second harmonic waves, A_1 and A_2 respectively – is measured at some distance from the transmitter. Measurements of β have been realized using longitudinal waves e.g. [25, 117], Rayleigh surface waves e.g. [26, 30, 118–120], and Lamb wave (or plate) modes [23, 27, 121, 122].

The majority of this work focuses on longitudinal wave measurements of the acoustic nonlinearity parameter, with some exploration of Rayleigh wave measurements. This section gives a general overview of current experimental methods for both longitudinal and guided wave measurements of β, followed by a detailed description of the measurement techniques, set-ups, and post-processing used for the longitudinal and Rayleigh wave experiments. Finally, an overview of other complementary material property measurements – hardness testing and thermo-electric power – is also provided.

5.1.1 Longitudinal Waves

Measurements of β using longitudinal waves have been conducted with contact piezoelectric transducers, capacitive transducers [117, 123], and laser interferometer detection [123]. Contact piezoelectric transducers offer a robust solution since these

transducers are typically used in other linear ultrasonic measurements, sample surface preparation is not extreme (typically involving hand polishing of the contacting surface), and can be purchased off-the-shelf for relatively low cost. However, transducers must be bonded (or coupled using a liquid coupling agent) to the sample surface which can introduce measurement variation if conditions are not kept consistent [124]. Capacitive transducers offer a "non-contact"-type detection method where the transducer is held at a small distance above the sample (1–10 μm). The sample (or a conductive coating) acts as one plate of a capacitor, and the impinging ultrasonic wave causes the capacitive gap spacing to vary with time. While this method offers a more direct way of measuring absolute displacements of the first and second harmonic waves compared to piezoelectric transducers (which require a series of calibrations for these absolute measurements [125]), sample preparation is cumbersome, requiring an optically flat and parallel sample surface over the receiver area and a small gap of only a few microns.

An absolute measure of β is possible with longitudinal waves using either capacitive transducers [117] or contact piezoelectric transducers using a calibration procedure [125] in which the absolute displacement amplitude of the first and second harmonic waves can be measured. β is more typically measured as a relative parameter since it is more practical in an in-situ setting to measure the relative amplitudes of A_1 and A_2 rather than the absolute physical displacement of the first and second harmonic waves. Further, in the current experiments on irradiated material, absolute measurements were not feasible due to time limitations in handling the radioactive samples. In the simplification of a relative measure of nonlinearity, the electrical amplitudes of the first and second harmonic are instead measured and the relative acoustic nonlinearity parameter is calculated, which is defined as:

$$\beta' = \frac{A_2^{el}}{\left(A_1^{el}\right)^2} \frac{8}{x\kappa^2} \tag{115}$$

Note that the relative acoustic nonlinearity parameter is proportional to the absolute

acoustic nonlinearity parameter and thus the material property and microstructural changes it encompasses, with respect to its initial state. From this point forward, any mention of the "acoustic nonlinearity parameter" refers to the relative acoustic nonlinearity parameter as defined in Equation 115. A measurement of β' can be made by varying the input amplitude and measuring the resulting first and second harmonic amplitudes, and then calculating the slope of the linear fit between $\left(A_1^{el}\right)^2$ and A_2^{el}, to eliminate nonlinearity from instrumentation, which do not follow the same rule that $A_2 \propto A_1^2$ as is the case for the quadratic material nonlinearity. Note that in measurements utilizing longitudinal waves, the propagation distance and the wavenumber were generally kept constant; otherwise β' is scaled accordingly.

5.1.2 Guided Waves

Guided wave measurements of the acoustic nonlinearity parameter have the advantage of being capable of eliminating any contact or transducer effects of the transmitting transducer, as well as eliminating nonlinearities induced by different excitation voltages. This is done by making measurements of the first and second harmonic wave at different propagation distances from the source transducer, i.e. varying x in Equation 115. Then, the slope of the linear fit between $A_2^{el}/\left(A_1^{el}\right)^2$ and x is an equivalent measure of β' from Equation 115, although care must be taken to account for diffraction effects particularly if the transmitting transducer has some nonlinearity associated with it [16]. As such, measurements utilizing Rayleigh waves have received considerable attention throughout the literature – for example using wedge–contact generation and/or reception [26, 28, 30, 120, 124], laser interferometer detection, air coupled detection [16], comb transducer generation and detection [119], and EMAT detection [126]. Using specific Lamb wave mode pairs to generate the second harmonic wave [11, 127] has also been explored using wedge contact transducers to make

measurements of β' [23, 121, 122]. However, Lamb waves are multi-modal and dispersive – the phase and group velocity are frequency-dependent – making it difficult to isolate specific frequencies of a single mode, and thus difficult to accurately extract the first and second harmonic amplitudes that are purely from material nonlinear effects. While guided waves do offer some advantages in nonlinear measurements, achieving consistent coupling becomes increasingly difficult for guided wave wedge set-ups, which can still factor into measurement error on the detection side, so the push toward a non-contact detection method will be crucial for robust measurements on real structures.

5.2 Longitudinal Measurements

5.2.1 Experimental Set-up

The majority of measurements of β in this thesis used longitudinal waves through Charpy V-notch impact samples. These samples are 10 mm x 10 mm x 55 mm in geometry. In these longitudinal experiments, two commercial piezoelectric contact transducers were mounted on opposite sides of the Charpy samples to transmit and receive an ultrasonic longitudinal wave through the thickness (along the 10 mm dimension). The lithium-niobate transducers, manufactured by Valpey Fisher, were 6.35 mm in diameter Light oil coupling was used between the transducer faces and the sample surface to ensure efficient acoustic energy transmission. The sample and transducers were mounted and aligned in a specially designed fixture for accurate alignment and consistent clamping [128]. A RITEC high power amplifier, used either by itself with a built-in function generator or in conjunction with an external function generator, excited the transmitting transducer (with center frequency tuned to f_1) with a multi-cycle sinusoidal wave at f_1. The number of cycles was optimized with each experimental set. The receiving transducer had a center frequency of approximately $2f_1$ to accurately detect both the small amplitude second harmonic wave

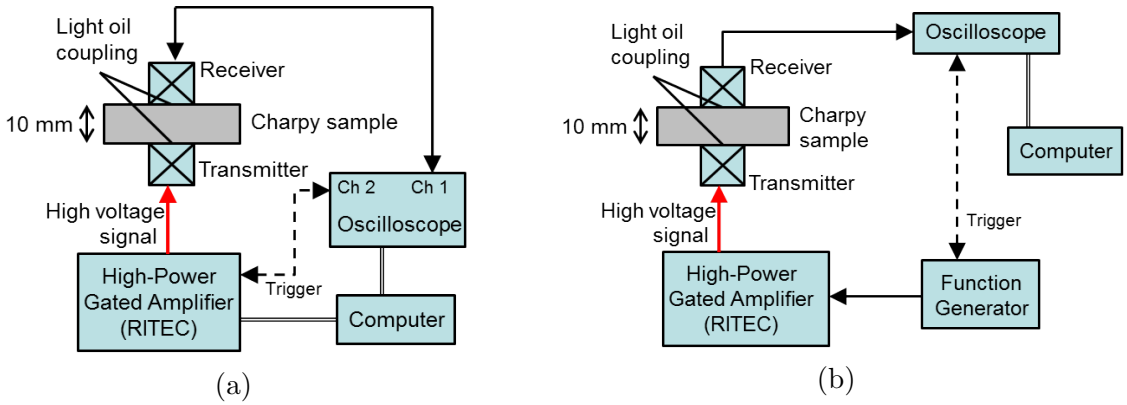

Figure 14: Schematics of experimental set-ups for longitudinal SHG measurements of the acoustic nonlinearity parameter (from Matlack et al. *JAP* 2012, and Matlack et al. *JNM* 2014).

and the much larger amplitude first harmonic wave simultaneously. The received signal was averaged 256 times, to improve the signal-to-noise ratio, with an oscilloscope (Tektronix TDS 5034B), and then transferred to a computer for post-processing. The two experimental set-ups used in this work for longitudinal wave measurements of β' are shown in schematic form in Figure 14 [115, 129].

The amplitudes of the first and second harmonic waves, A_1 and A_2, were obtained by extracting the steady-state portion of the time signal, applying a Hann window to the extracted time signal, and taking a fast Fourier transform (FFT) of the extracted and windowed signal. Figure 15 [115] shows a typical measured time-domain signal and its corresponding Hann-windowed time signal, and Figure 16a [115] shows a its respective FFT. Note that the full signal did not necessarily fit in the thickness of the sample, but the FFT was taken on only the amount of cycles of that fit within the thickness of the sample to eliminate contributions from reflected waves. The purpose of using a relatively long signal compared to sample thickness was to obtain a higher energy acoustic wave and eliminate ringing effects at the end of the signal. The output level of the amplifier was increased in small increments of output power up to a maximum of about 740 V_{pp} (peak-to-peak voltage) to achieve ten separate measurements of A_1 and A_2, and the slope of A_2/A_1^2 was calculated -

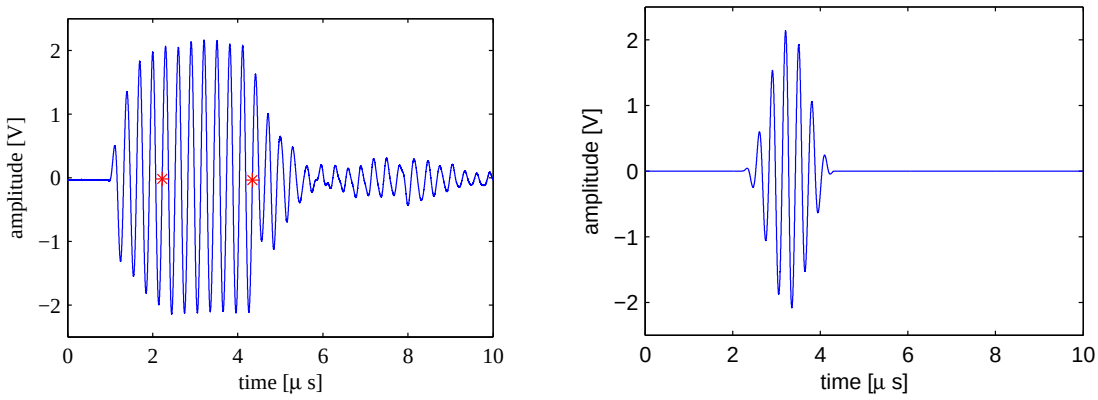

(a) (b)

Figure 15: (a) Representative time signal as measured by the receiving transducer in the longitudinal measurements, and (b) the corresponding Hann-windows time signal. Data is taken from one of the irradiated-annealed-re-irradiated samples (see Chapter 7).

this slope is a relative measure of the acoustic nonlinearity parameter, β', as defined in Equation (115). An example of the measurement data for the first and second harmonic amplitudes is shown in Figure 16b [115], illustrating the linearity of the A_2 to A_1^2 relationship.

In one set of experiments, a RITEC high power amplifier (SNAP–5000) generated a 15–cycle sinusoidal wave at 2.25 MHz, and the frequencies of the transducer pair were tuned to 2.5 and 5.0 MHz for the exciting and receiving transducer, respectively. The output power of the RITEC amplifier was varied in 5% increments from 40-90% full power. In the second set of experiments, a function generator (Agilent 33250A) generated a 12–cycle sinusoidal wave at 3.3 MHz, amplified with a high-power gated amplifier (RITEC GA2500A), and the frequencies of the transducer pair were tuned to 3.5 and 7.5 MHz for the exciting and receiving transducer, respectively.

5.2.2 Measurement Fixture

In order to make robust and accurate measurements of the acoustic nonlinearity parameter, the experimental measurement fixture must allow for consistent and repeatable measurements. The fixture for longitudinal wave measurements of the acoustic

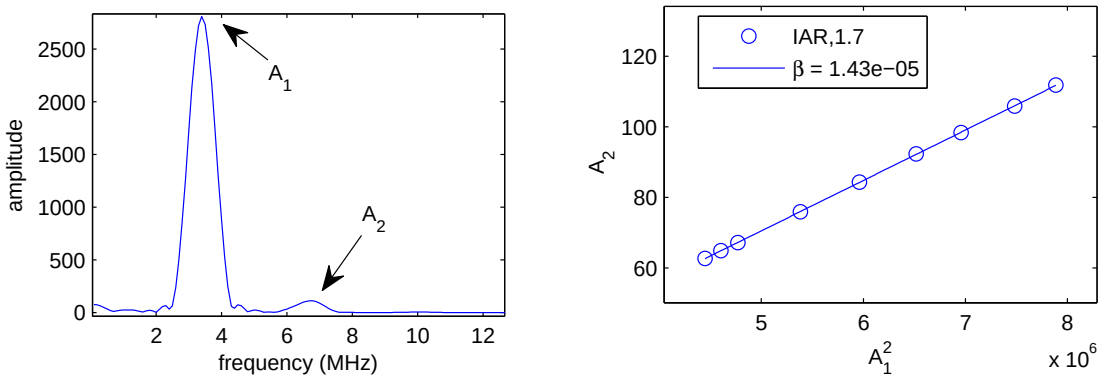

(a) (b)

Figure 16: (a) Representative FFT of time signal shown in Figure 15, and (b) an example of the measurement data for first and second harmonic amplitudes, where the slope of the linear fit of the data is the relative acoustic nonlinearity parameter β'.

nonlinearity parameter must align both transducers with a high degree of precision, must clamp the transducers to the surface of the material sample with a consistent contact pressure, and must minimize setup time since sensitive samples (radioactive material) were handled. These design points ensure accuracy of the extracted first and second harmonic amplitudes that make up the measured acoustic nonlinearity. To make nonlinear ultrasonic measurements more accessible, the fixture must have a simple and intuitive setup.

The proposed fixture design for measurements on irradiated samples enabled quick set up of an experiment to make a nonlinear ultrasonic measurement. The main functions of the fixture are to clamp the sample, and self-align and clamp the transducers in a repeatable manner. All parts are mounted to a plate and are shown in an exploded view in Figure 17a [128], and a photograph of the fixture is shown in Figure 17b [128]. The sample (a) is placed on fixed plate (c) by pulling back the movable plate (d) and placing sample in between this plate and the fixed plate (b). The fixed plate (c) is L-shaped to make sample mounting quick and easy while ensuring NLU measurements are taken at the same location on each sample. The movable plate (d)

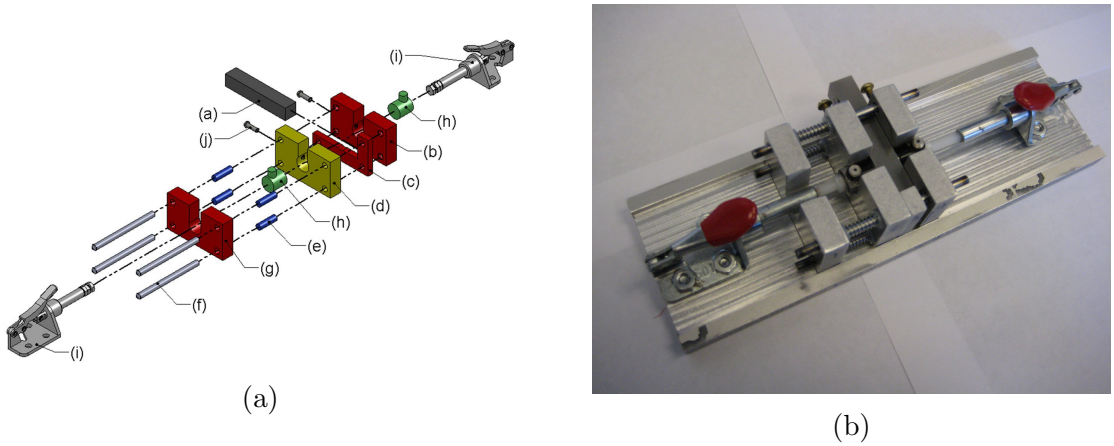

(a) (b)

Figure 17: (a) Schematic and (b) photo of fixture designed for longitudinal wave measurements of the acoustic nonlinearity parameter.

is spring-loaded (e) and clamps the sample in place once released, while also allowing for easy removal of the sample. The spring mechanism works by mounting the springs (e) on alignment rods (f) in between the movable plate (d) and another fixed plate (g). Transducers (h) are housed in notches in plates (b) and (d) on opposite sides of the sample (a) that align transducers in the vertical center of the sample. Toggle clamps (i) are used to clamp transducers onto sample, while also allowing for a user-defined clamping force. The clamps used have a maximum holding force of 445 N. By changing the length of the toggle clamp, measurements can be made on samples with different thickness. The alignment rods (f) enable an automatic alignment of all plates. Set-screws (j) mounted on plates (b) and (d) provide accurate horizontal alignment of the transducers. The photograph in Figure 17 (right) shows the fully assembled fixture with mounted sample and transducers.

This fixture was used for measurements of the acoustic nonlinearity parameter on the irradiated samples as well as the surrogate samples investigated throughout this work. For one set of irradiated sample measurements, the fixture was transported to a laboratory in Dresden, Germany, and experiments were set up by staff certified to handle the radioactive samples. Thus, these experiments provided a good means of evaluating the performance of the fixture. It was found that there was a maximum

of 5% variation between different measurements on the same sample, which is small compared to changes measured in the acoustic nonlinearity parameter over irradiation damage. Thus, the fixture provided repeatable measurements.

5.2.3 Post-Processing

5.2.3.1 Varying input parameters

While different input parameters were used in different sets of longitudinal wave measurements of β, each data set presented in this work compares measurements to a baseline material (undamaged, unirradiated, etc.), such that the parameter β/β_0 is always presented, where β_0 is the measured β of the undamaged, unirradiated, or otherwise baseline material. This normalization eliminates any effects from different signal lengths (i.e. different amounts of acoustic energy), and frequency of first and thus second harmonic waves. It also eliminates any effects of nonlinearity due to instrumentation from transducers, amplifier, and coupling/contact conditions (so long as these conditions are consistent). Further, specific excitation frequencies used in these experiments was optimized based on each specific transducer pair used in the experiment.

5.2.3.2 Diffraction Correction

A more accurate expression for the acoustic nonlinearity parameter can be found by accounting for the on-axis diffraction effects of both the first and second harmonic wave. A diffraction correction $|D_\beta|$ to β is introduced as [123]:

$$|D_\beta| = \frac{|D(\omega)|^2}{|D(2\omega)|} \tag{116}$$

where $|D(\omega)|$ and $|D(2\omega)|$ are the diffraction corrections to the first and second harmonic waves, respectively. The equation for the acoustic nonlinearity parameter scaled by this diffraction correction, β_D, is then given by:

$$\beta_D = |D_\beta|\beta \tag{117}$$

The linear diffraction correction, i.e. the diffraction correction for the propagating first harmonic wave, has been derived in full previously [130] for a piston source such that the amplitude is constant across the source. This diffraction correction is given by:

$$D(\omega, x, a) = 1 - \exp\left(-i\kappa a^2/x\right)\left[J_0\left(\kappa a^2/x\right) + iJ_1\left(\kappa a^2/x\right)\right] \tag{118}$$

where $\kappa = \omega/c$. In actuality, transducer are not a perfect piston source and there is some spatial distribution of amplitude over the surface of the transducer face, which has been shown to approximate a Gaussian distribution [131]. This function is shown in Figure 18 for three separate frequencies of 2.25 MHz, 3.3 MHz, and 4.6 MHz. The lower two frequencies were the excitation frequencies used in the ultrasonic measurements throughout this work. The function is shown for wave propagation distances up to 30 mm, and for a $^1/_4$–inch diameter ultrasonic transducer. The Charpy V-notch samples measured throughout this work had a thickness (along the direction of wave propagation) of approximately 10 mm, which is clearly in the near-field of the 3.3 MHz and 4.6 MHz wave. Figure 19 shows the same diffraction correction function focused on the relevant variations in wave propagation distance for the different sample sets investigated in this work. It can be seen that even though most measurements are made in the near-field region, the variation in measured wave amplitude due to sample thickness (and thus linear diffraction) variations is minimal.

The diffraction of the second harmonic wave is spatial different than that of the first harmonic. The wave is generated not by the transducer, but by the propagating first harmonic wave, which is diffracting over propagation distance. The diffraction can be physically interpreted as follows: at each instance that a portion of the second harmonic wave is generated, that portion will then diffract linearly over the remainder of propagation distance to the receiving transducer. This nonlinear diffraction effect

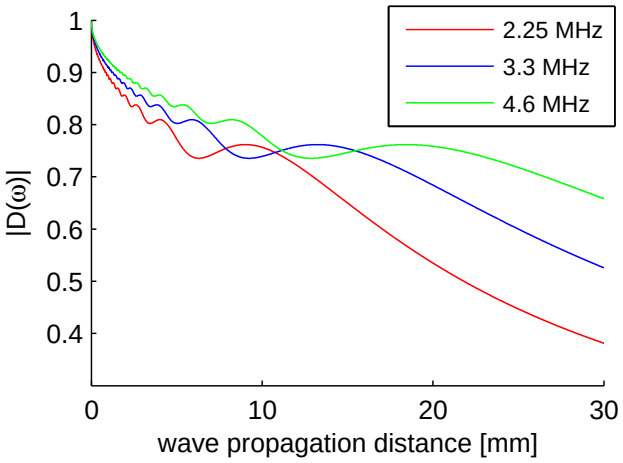

Figure 18: Linear diffraction correction for increasing wave propagation distance for three separate frequencies.

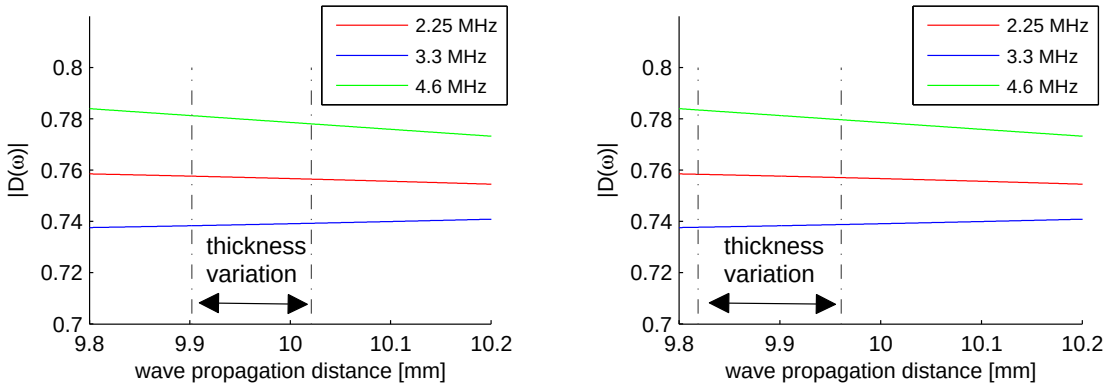

(a) (b)

Figure 19: Linear diffraction correction for increasing wave propagation distances corresponding to sample thickness of the measured Charpy irradiated RPV steel samples at $T_i = 290°C$ (left) and $T_i = 255°C$ (right), for three separate frequencies.

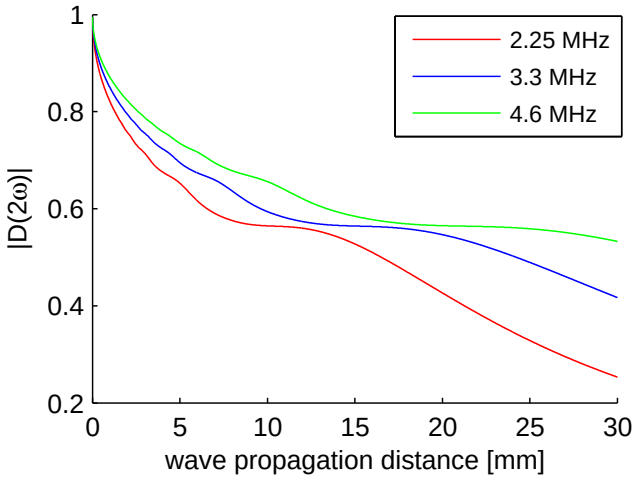

Figure 20: Nonlinear diffraction correction for increasing wave propagation distance for three separate excitation frequencies (first harmonic frequencies are labelled in the plot).

has been derived previously [123, 132] and is given as:

$$|D(2\omega, x, a)| = \frac{\left| \int_0^x \left[D\left(\omega, x - \sigma/2, a\right) \right]^2 \mathrm{d}\sigma \right|}{x} \tag{119}$$

where $D\left(\omega, x, a\right)$ is given in Equation 118.

The trend of the nonlinear diffraction correction for increasing wave propagation distance is shown in Figure 20. Note that labels in this plot are the frequencies of the excitation or first harmonic wave. Figure 21 shows the same diffraction correction function focused on the relevant variations in wave propagation distance for different sample sets investigated in this work. It is again shown that the difference in the diffraction correction for the sample thicknesses investigated is minimal. Calculations of the diffraction correction for measured β on the various sample sets measured in this work are given in Appendix A, showing negligible changes to β for the variation in thickness of the samples measured.

5.3 Air-Coupled Detection: Rayleigh Wave Measurements

To monitor the acoustic nonlinearity parameter using Rayleigh waves, a piezoelectric transducer-wedge setup with air-coupled detection was used; see schematic in Figure

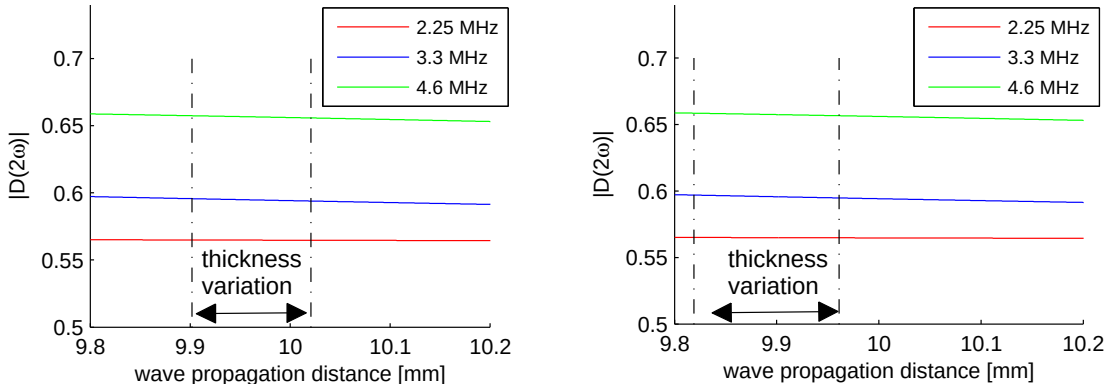

Figure 21: Nonlinear diffraction correction for increasing wave propagation distances corresponding to sample thickness of the measured Charpy irradiated RPV steel samples at (a) $T_i = 290°C$ and (b) $T_i = 255°C$, for three separate excitation (first harmonic) frequencies.

22, from [16]. The same high-power gated amplifier (RITEC) utilized in the longitudinal measurements – a RITEC GA2500A used in conjunction with function generator Agilent 33250A – was used to excite an 2.1 MHz ultrasonic 20-cycle tone burst in a narrowband commercial piezoelectric transducers mounted on acrylic wedge, which was then mounted on the test sample. This wedge was designed so the longitudinal wave propagating through the wedge was at an angle such that a Rayleigh surface wave was generated at the interface of the wedge and test sample – essentially, the angle satisfied phase matching between the wave velocity component in the propagation direction in the wedge material and the Rayleigh wave velocity in the test sample. An air-coupled transducer with center frequency of 3.9 MHz was used to receive the first and second harmonic waves in air, which were leaked as longitudinal waves from the Rayleigh wave propagating along the sample surface. This received signal was amplified by 40 dB and an average of 256 signals was taken with an oscilloscope (Tektronix TDS 5034B) for a higher signal–to–noise ratio, and then transferred to a computer for signal analysis. Signals were windowed to eliminate transducer ringing at the beginning and end of the signal, and then a fast frequency transform was performed to obtain the amplitudes of the first and second harmonic waves (A_1 and A_2,

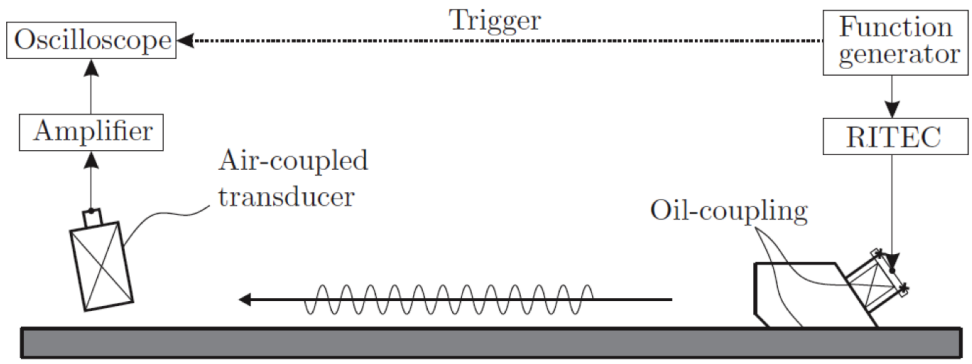

Figure 22: Schematic of experimental set-up for Rayleigh wave measurements of β using wedge generation and an air-coupled receiver.

respectively). This process was repeated for several wave propagation distances, and the acoustic nonlinearity parameter was measured as the slope of the ratio A_2/A_1^2 over propagation distance x, as shown in Figure 23. A detailed description for the signal processing techniques and diffraction corrections for Rayleigh wave nonlinear measurements using air coupled detection is given in [133]. This setup has been validated by measuring the relative nonlinearity parameter in two different aluminum alloys (Al 2024-T351 and Al 7075-T651) and comparing the ratio of the measured nonlinearity parameters with ratios from absolute measurements in the literature [133].

5.4 Complementary measurements

5.4.1 Vickers Microhardness

Vickers microhardness measurements were made on heat treated surrogate samples after both the solution annealing and thermal aging treatments. A Buehler High Quality Hardness Tester was used, and the same conditions and parameters applied for measurements of the same material (i.e. applied load and load time was kept constant). Hardness measurements were made at six different locations on each specimen, and both lateral and transverse measurements were made to investigate any potential sample anisotropy.

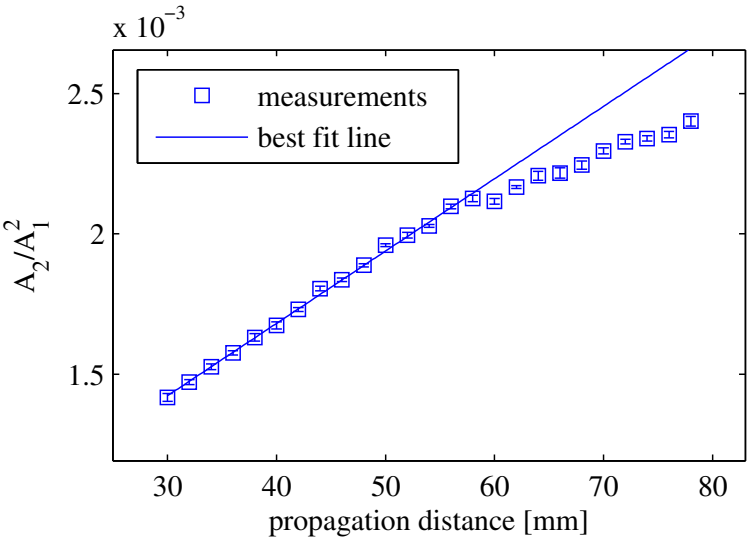

Figure 23: Representative measurement (average of three separate measurements) of β using Rayleigh waves and air-coupled detection – the slope of the linear fit between the measured ratio A_2/A_1^2 over propagation distance x is proportional to β.

5.4.2 Thermo-electric Power

Thermo-electric power (TEP) measurements were utilized to gain insight into the general trend of precipitation in thermally aged material [16,134,135]. This technique is based on the Seebeck effect, which relies on the fact that when a temperature differential, ΔT, is applied to a sample, a change in voltage, ΔV is generated across the sample. The Seebeck coefficient, measured by the TEP technique, is defined as:

$$S = \frac{\Delta V}{\Delta T} \tag{120}$$

The Seebeck coefficient is sensitive to chemical composition of the material, and TEP is generally used industrially to sort metals and alloys. Generally, most elements decrease the TEP value in Fe-based materials and alloys. The TEP value is also increased due to coherency strains of precipitates, and decreased due to dislocations. Incoherent precipitates have been shown to have no effect on the TEP value [135]. TEP has been used, for example, to monitor precipitation in duplex steel [134], and to monitor copper precipitates interstitial-free steel [135]. TEP has advantages of being a quick measurement independent of sample size [135], however it is very sensitive to

surface conditions and contact interfaces between the probe and sample [136].

TEP measurements were made using a Koslov Thermo-Electric Alloy Sorter TE-3000, which is calibrated with a Hastelloy C-276 steel probe. Sample surfaces were first prepared by thoroughly cleaning with acetone to remove any debris. The TEP alloy sorter was turned on and allowed to warm up for a sufficient amount of time before making measurements. To make a measurement, the reference probe was place on the sample, and then the probe with the heated tip was applied to the other side of the sample with slight pressure for a few seconds. Three to five measurements were made on each sample in each heat treated condition, to determine a representative value of TEP.

CHAPTER VI

SURROGATE MATERIAL

6.1 Overview and Purpose

Neutron irradiated samples are by nature difficult to work with since samples are radioactive, require experimentation and storage in either hot cell facilities or at least in shielding fixtures, contaminate experimental instrumentation, and create radioactive waste. Therefore, it is of interest to develop a set of surrogate specimens that approximates some aspect of an irradiated RPV steel microstructure. A sample set such as this could help deconvolve influences of different microstructural features to the acoustic nonlinearity parameter, since a surrogate sample set will only contain selected microstructural features present in radiation damage.

Two materials have been identified as potential candidates for a surrogate material: Fe-Cu alloys, and 17-4PH stainless steel. It has been shown in previous work that thermal aging of model alloys, such as binary Fe-Cu alloys, produces copper precipitates of similar size and number density as radiation damage in RPV steels [137–140]. These alloys, as well as tertiary Fe-Cu-X alloys, have been widely investigated previously as model alloys to study precipitation effects during thermal aging that also occur due to radiation damage in RPV steels, for example [137, 138, 141–145]. 17-4PH stainless steel is known to harden through the formation of copper precipitates during thermal aging [146–150]. This chapter focuses on 17-4PH material, and provides background on current knowledge of the microstructural evolution in 17-4PH under thermal aging, presents nonlinear ultrasonic measurements on thermally aged

17-4PH, and discusses how these measurements could provide insight into deconvolving the effect of copper-enriched precipitates, which is the most important contributor to radiation embrittlement in RPV steels, to ultrasonic nonlinearity from other radiation-induced microstructural features.

6.2 17-4PH Stainless Steel

6.2.1 Background

17-4PH stainless steel is a martensitic precipitate-hardenable (hence the designation "PH") martensitic alloy. This material is a "self-quenching" steel, meaning it transforms from austenite to martensite irrespective of the cooling rate. It has been shown that the martensitic transition begins at 160°C upon cooling from above the austenitic temperature. Hardening in this material is caused by thermal aging, where the material is held at a temperature between about 400°C and 600°C for some time [151]. In these temperature ranges, copper has a low solubility, and so these atoms diffuse and form precipitates, which pin dislocations. Generally, an increasing amount of coherent precipitates form in the material up to a peak aging time. After peak aging, these precipitates coarsen and become incoherent with the matrix.

It has been reported that the 17-4PH material in the solution annealed state (typically 1050°C for 1 hour followed by water quenching) exhibits a martensitic microstructure with a small percent of alpha-ferrite (reported to be ∼7% at room temperature in [146]). Microstructural analysis has shown no copper precipitates formed in the martensitic phase of the solution annealed state. TEM analysis showed a high density of small, incoherent precipitates of fcc-copper in the alpha-ferrite phase, which remained unaffected by subsequent heat treatment [148]. Dislocation density in the martensite at room temperature has been reported to be at $4\times10^{15}/\mathrm{m}^2$, and about $1\times10^{15}/\mathrm{m}^2$ in the austenitic phase [146]. This dislocation density has been shown to remain constant up to about 500°C. These dislocations are induced in the martensite

and austenite phases during transformation, due to the difference in density of the two phases such that regions of forming martensite cause deformation on the surrounding austenitic regions. Viswanathan et al. mention possible quenched-in vacancies should be present in the quenched microstructure as well, but the authors do not provide evidence of these vacancies [149].

Further heat treatment and tempering has been shown to produce copper-rich precipitates. In the standard "tempered" microstructure after aging for 4 hours at 580°C fine coherent bcc-copper precipitates were detected with bright-field TEM and three-dimensional atom probe (3DAP) analysis [148]. Quantitative values for the density and the size of these precipitates were not given. Heat treatment beyond this tempering has been shown to produce a high density of incoherent copper-rich precipitates, with a reported diameter of 3 nm after 100 hours of aging at 400°C, and a diameter of 8 nm after 5000 hours of aging at 400°C, along with other phases and precipitates alloyed with other elements [148].

Hsiao and authors [150] measured copper-rich elliptically-shaped precipitates with short and long axis dimension of 15 nm and 25 nm in diameter, in a sample that was aged at 480°C for 1 hour after solution annealing and water quenching. The authors state that the precipitate is shown to be coherent from TEM bright field images since there is no large strain contrast, however FEG-TEM shows the precipitate has an fcc structure, indicating it is incoherent with the matrix.

Bhattacharya and authors [147] conducted magnetic Barkhausen noise measurements to characterize aging of 17-4PH. Corresponding X-ray diffraction measurements showed that samples in the quenched condition had a residual stress of -248 ± 20 MPa, and after aging for 1h at 475°C this stress was reduced to 18 ± 8 MPa.

Note that in addition to precipitates, dislocations also strongly contribute to nonlinearity. So, to investigate precipitation effects on the acoustic nonlinearity parameter using 17-4PH material, an aging temperature should be chosen such that the

Table 1: Chemical composition of as-received 17-4PH stainless steel.

C	Cr	Cu	Ni	Mn	Si	Nb
0.023	15.15	3.07	4.46	0.63	0.46	0.26
Mo	Co	N	P	S	Ti	Fe
0.08	0.044	0.023	0.016	0.001	0.001	remainder

dislocation density remains constant over heat treatment. Previous work measured dislocation density changes in 17-4PH samples with neutron diffraction shows dislocation density starts to decrease drastically around 500°C, below which the dislocation density in the martensite remains roughly constant at $4 \times 10^{15}/\text{m}^2$ [146].

6.2.2 17-4PH Specimen Preparation

Bulk material of 17-4PH stainless steel, with composition shown in Table 1, was received as rectangular bars with thickness of about 13 mm. The material had a tensile strength of 1384 N/mm^2 and a yield strength of approximately 1263 N/mm^2. The as-received material was previously hot rolled and solution annealed at 1040°C for 6 hours, and then air cooled. Some specimens were left as-received in terms of geometry, and these samples were used for Rayleigh wave measurements. Other specimens with geometry of 10 mm x 10 mm x 56 mm were cut using wire EDM to reduce surface stresses, reduce material elimination, and produce a sufficient surface finish, and these samples were used for longitudinal wave measurements. All specimens were surface ground at low speed and with sufficient cooling to ensure smooth and parallel faces. After surface grinding, as well as after all heat treatments, samples were hand polished with 400 grit polish paper, and Charpy-sized samples were polished with addition 600 and 800 grit polish paper.

As mentioned, two different geometries of samples were investigated. Charpy-sized samples were aged from either the as-received state (referred to as "AC" for "air cooled"), while some samples were given a second solution annealing treatment at

1175°C for 2 hours in a vacuum furnace and subsequently quenched with high-pressure gas (referred to as "GQ" for "gas quenched"). The purpose of the second solution annealing and gas quench was to avoid precipitation formation during cooling from the solution annealing, so that the as-is state was free of precipitates. Some samples from both the AC and GQ sets were then aged in an uncontrolled atmosphere for 1-6 hours at 400°C.

Rectangular bar samples were left in the as-received geometry of 19 mm x 38 mm x 230 mm. Samples were then aged for 0.1-6 hours at 400°C. Some as-received samples were then given a second solution annealing treatment at 1100°C for 2 hours in an uncontrolled atmosphere and then water quenched (referred to as "WQ" for "water quenched"), creating a baseline condition similar to the GQ condition. One WQ sample was then aged for 1 hour at 400°C.

All aged samples were heated in a furnace from room temperature, at an average rate of 9°C/min. A thermocouple close to the surface of the samples was used to monitor the sample temperature. After heat treatment, samples were air cooled to room temperature. A summary of the sample designations and aging conditions are given in Table 2.

6.2.3 Material Characterizations

Vickers hardness measurements and thermo-electric power measurements were made on all heat treated 17-4PH samples to assess the success of the heat treatments. The measured hardness for bar and Charpy samples is shown in Figure 24 [16]. These hardness measurements were made using a 2000g force for 10 seconds. Results show an increase in hardness with increasing heat treatment time as is expected for this particular aging temperature and time of 400°C up to 6 hours [151].

Thermo-electric power (TEP) results are shown in Figure 25 for heat treated Charpy and bar samples [16]. Results show an increase in TEP with increasing heat

Table 2: Sample designations and aging conditions for 17-4PH Charpy samples.

Geometry	Wave Type	Sample Designation	Solution Annealing	Cooling	Aging Time @ 400C
Charpy	Longi-tudinal	GQ	1100C/2h	gas quenched	–
		GQ-1	1100C/2h	gas quenched	1h
		GQ-6	1100C/2h	gas quenched	6h
		AC	1040C/6h	air cooled	–
		AC-1	1040C/6h	air cooled	1h
		AC-6	1040C/6h	air cooled	6h
bar	Rayleigh	GQ	1100C/2h	water quenched	–
		GQ-1	1100C/2h	water quenched	1h
		AC	1040C/6h	air cooled	–
		AC-0.1	1040C/6h	air cooled	0.1h
		AC-1	1040C/6h	air cooled	1h
		AC-6	1040C/6h	air cooled	6h

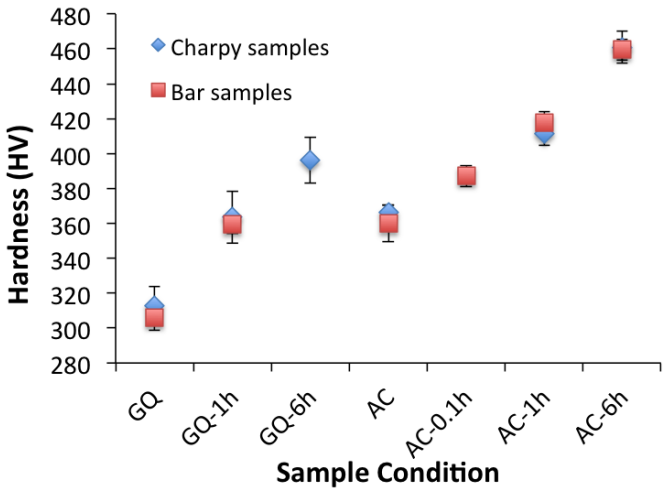

Figure 24: Measured Vickers hardness for 17-4PH Charpy and bar heat treated samples, for gas quenched and air cooled initial state. Note that "GQ" is used for water quenched samples in bar form, since microstructure due to gas vs. water quench is expected to be comparable.

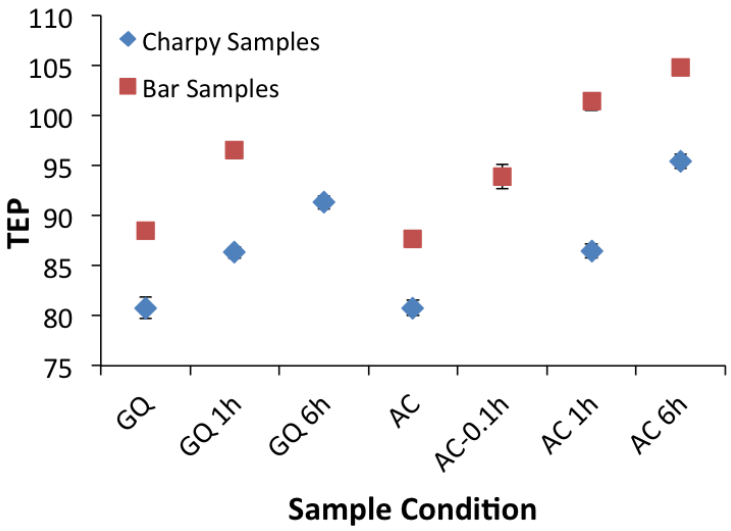

Figure 25: Measured thermo-electric power (TEP) for 17-4PH Charpy and bar heat treated samples, in the gas/water quenched and air cooled initial state. Note that "GQ" is used for water quenched samples in bar form, since microstructure due to gas vs. water quench is expected to be comparable.

treatment time for both quenched and air cooled initial state samples. It is specifically pointed out that the TEP value for both the gas quenched samples and the air cooled samples is the same for both the bar and Charpy sample sets. Note that the TEP value is consistently higher in the bar samples compared to the Charpy samples, indicating some difference in at least surface composition or baseline microstructure for the Charpy samples. An increase in TEP corresponds to a decreasing amount of copper in the matrix material, indicating the formation of copper precipitates.

TEM work was also done on the air-cooled 17-4PH samples, in efforts to characterize the size and number density of the precipitates. The TEM analysis was conducted at Pacific Northwest National Laboratory. However, the microstructure was so heavily dislocated and deformed that it was difficult to accurately view and analyze the precipitates. A TEM image of the air-cooled as-received (AC) condition is shown in Figure 26. There was little evidence of precipitation in this condition, and the images were dominated by contrast produced by a high density of dislocations in the grains. The high density of dislocations limited the ability to image any

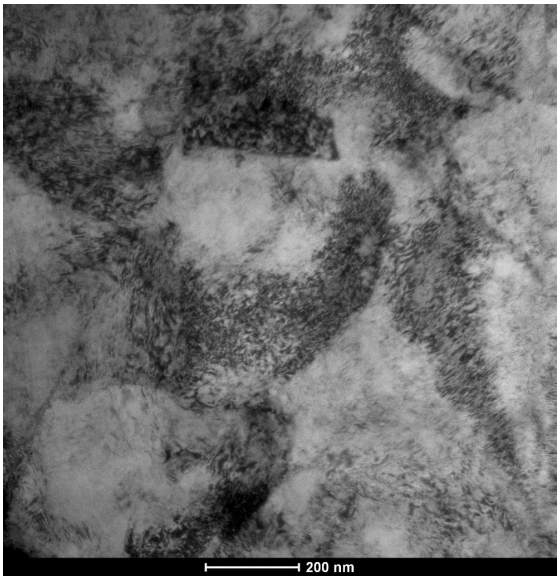

Figure 26: TEM image for 17-4PH as-received (air cooled condition). No evidence of precipitation can be seen, and grains contain a very high dislocation density, as indicated by the darker regions on the image.

precipitation unless precipitates are relatively large (at least 2-4 nm in radius). TEM images of 17-4PH material aged for 1 hour (AC-1) are shown in Figure 27. These images are still dominated by dislocation contrast, but a few isolated precipitates are indicated at the higher magnification – these are the small, striped, circular regions in the image. These precipitates may be carbides, due to their limited number and vicinity to grain boundaries, but composition could not be confirmed with the current TEM measurements. Chemical analysis of these small precipitates with TEM would require much thinner samples. The black spots seen in the higher magnification image in Figure 27 may be small copper-rich precipitates. A TEM image of 17-4PH material aged for 6 hours (AC-6) is shown in Figure 28. The contrast from the high dislocation density continued to mask the ability to accurately image any precipitation present.

3D Atom probe tomography (APT) was also conducted on the 17-4PH AC-6 sample at Pacific Northwest National Laboratory. Atom probe tomography maps atoms, and regions of visible clustering of atoms is indicative of clusters or precipitates, and more details and information can be found in [59, 74]. Preliminary results of Cu, Cr,

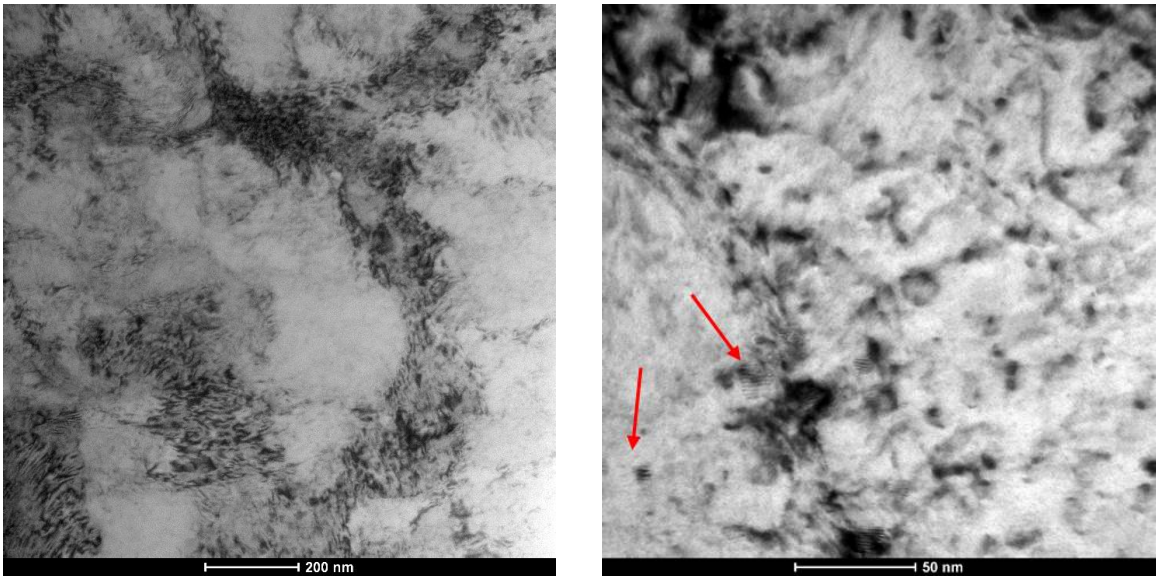

(a) (b)

Figure 27: TEM images for 17-4PH sample aged at 400°C for 1 hour (AC-1). Arrows indicate some isolated precipitates in the image on the right.

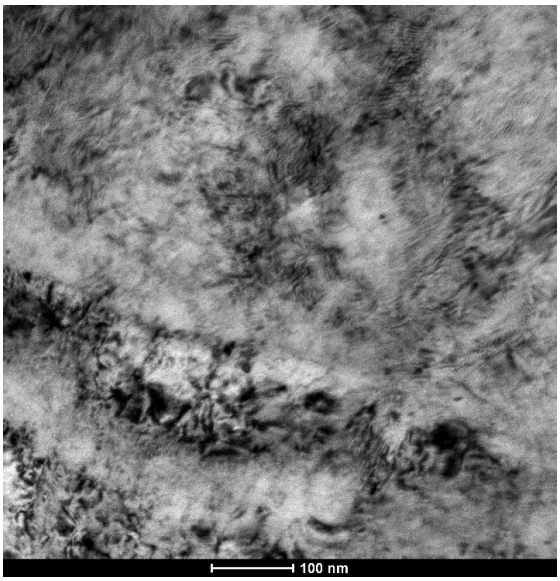

Figure 28: TEM image for 17-4PH sample aged at 400°C for 6 hours (AC-6). The contrast indicates there is still a high density of dislocations, which is likely masking the ability to image the precipitates.

and Ni atom maps are shown in Figure 29, and note that the datasets shown here were clipped to a thickness of 10 nm into the page for better clarity. These results show some clustering of Cu, but no segregation of clustering of any other atomic species was seen. Copper appears to be in the early stages of nucleation, clusters are measured to be less than 1 nm in diameter, and statistically significant clustering is difficult to discern. This supports the previous results where precipitation was not visible in TEM images. Since Cu is in such an early stage of nucleation, APT cannot accurately distinguish the precipitates nor provide an accurate estimate of number density.

6.2.4 Nonlinear Ultrasonic Measurement Results

Results for normalized measured β over heat treatment conditions with Rayleigh waves and an air-coupled detection system are shown in Figure 30 [16]. Results show about a 10% difference between air cooled as-is samples, and a decrease in β with increasing heat treatment time at 400°C, with a decrease of about 45% for the maximum aging time of 6 hours. Note that the difference in measured β for the as-is samples is not insignificant, but it is small compared to the change in β detected during thermal aging. A summary of the measured changes in β with Rayleigh waves for thermally aged samples is given in Table 3.

Results for normalized measured β over heat treatment conditions with longitudinal waves are shown in Figure 31. Measurements of the as-is condition are compared to the heat treated condition for each sample, since there was significant variation between samples in the air cooled or gas quenched condition. Results show no significant change in β due to aging at either 1 or 6 hours at 400°C. Specifically, for the gas quenched samples, an average of +4.9% change in β was detected for the samples aged for 1 hour, and an average of +3.4% change in β was detected for the samples aged for 6 hours. In both cases, the standard deviation of the measurements

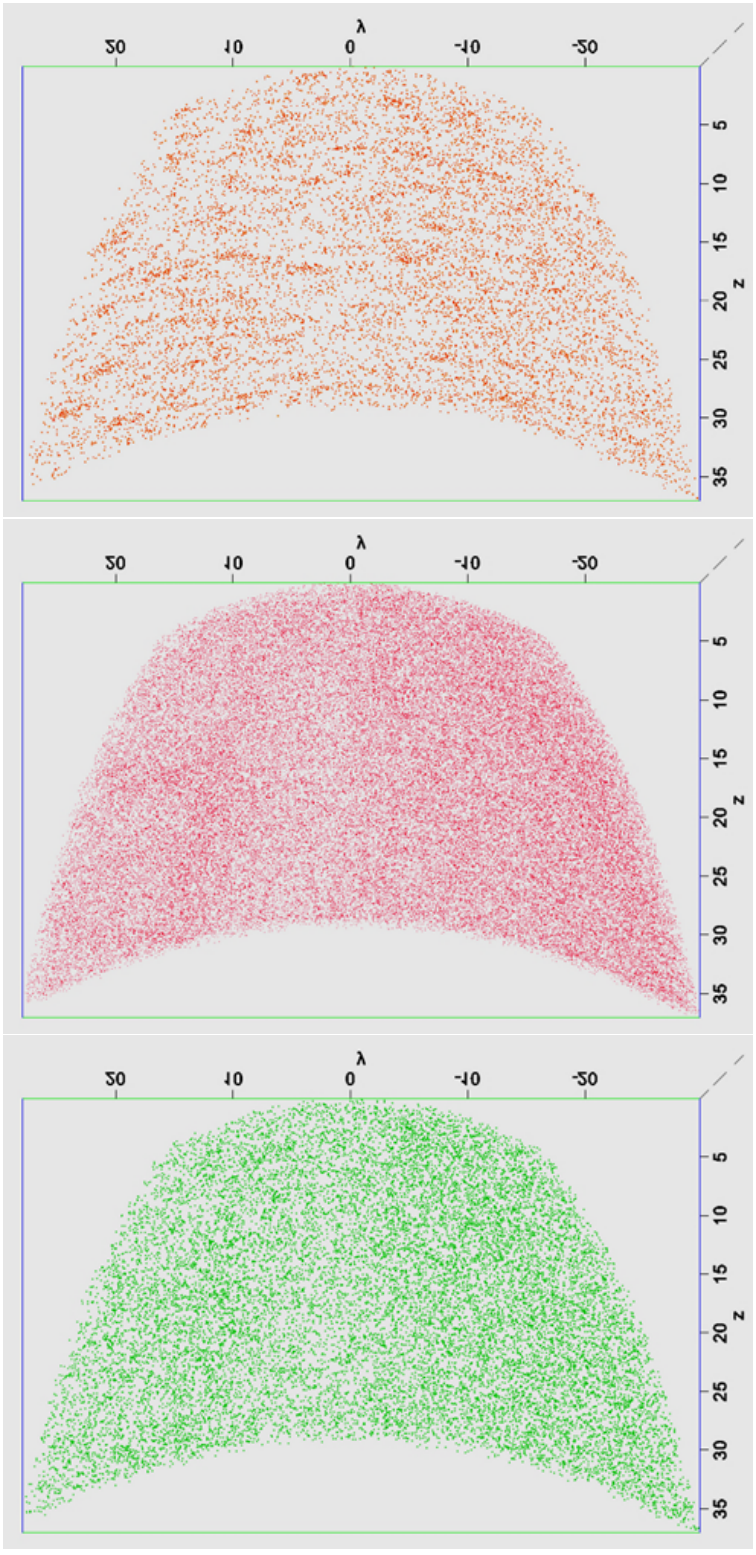

Figure 29: APT atom maps of Cu, Cr, and Ni (from top image to bottom) from sample 17-4PH AC-6.

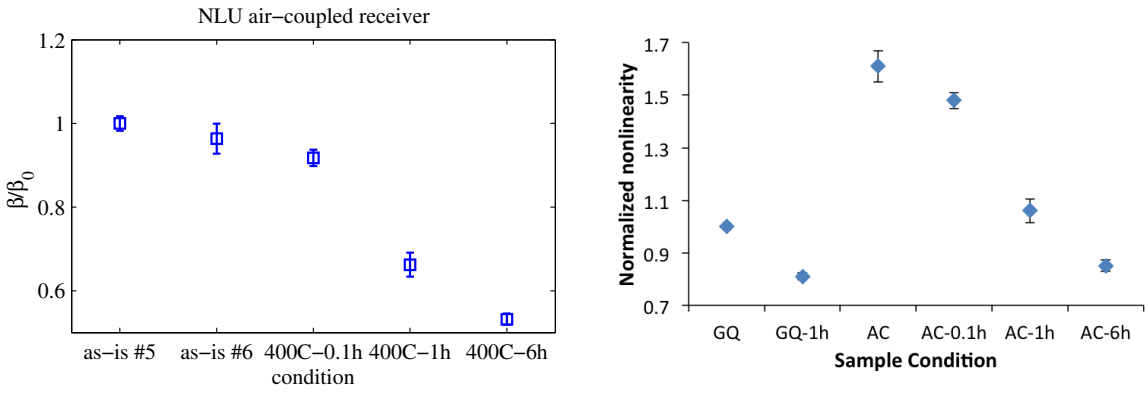

(a) (b)

Figure 30: Normalized measured β with Rayleigh waves and air-coupled detection for 17-4PH thermally aged material at 400°C in (a) air cooled state, and (b) water quenched compared to air cooled state. Each data point represents an average over three separate measurements.

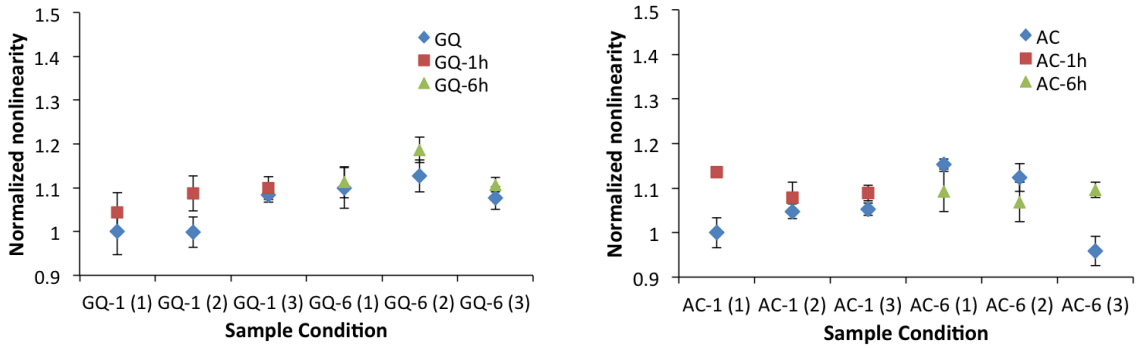

(a) (b)

Figure 31: Measurements of β using longitudinal waves for (a) gas quenched and (b) air cooled thermally aged 17-4PH Charpy samples.

was only slightly lower than these changes, meaning that the measurements are not sensitive enough to detect the changes in the microstructure. Similar results are seen in the air-cooled samples, although these samples showed more variation than the gas quenched samples. A summary of the measured changes in β for thermally aged samples is given in Table 4.

Table 3: Normalized measured β for gas/water quenched and air-cooled samples, using Rayleigh waves.

Sample Condition	Rayleigh β/β_{GQ}
GQ	1.0
GQ-1	0.81
GQ-6	n/a
AC	1.61
AC-0.1	1.48
AC-1	1.06
AC-6	0.85

Table 4: Change in β measured in 17-4PH Charpy samples over thermal aging, relative to as-is state.

Sample Condition	$\Delta\beta$ (longitudinal)	Standard Deviation
GQ-1	+4.9 %	3.7 %
GQ-6	+3.4 %	2.4 %
AC-1	+6.6 %	5.9 %
AC-6	+0.7 %	12.3 %

6.3 Discussions

6.3.1 Differences between Rayleigh and longitudinal measurements

The results from Section 6.2.4 show that Rayleigh waves are able to detect changes in the 17-4PH microstructure during thermal aging. The measured decrease in β with heat treatment time is likely due to the increased formation of copper precipitates that form in increasing quantities up to peak aging time. Recall that, in the simplest form of the precipitate-pinned model as presented in Section 2.3.2, $\Delta\beta \propto r^3/N^{1/3}$, where r is the average radius of the precipitates and N the number density of precipitates.

However, the longitudinal waves were unable to detect any changes among the aging conditions. Recall that the second harmonic wave amplitude, and thus the acoustic nonlinearity parameter, grows with propagation distance. The propagation distance in the longitudinal wave measurements was 10mm, whereas the propagation distance in the Rayleigh wave measurements was much larger (30-60mm). In these experiments, there is some non-zero "system" nonlinearity excited by the measurement system, likely from the transmitting transducer and the high power amplifier. This initial $A_{2,0}$ wave will diffract linearly, with a trend similar to the first harmonic wave diffraction model shown in Equation 118. If the propagation distance is small enough such that the generated material nonlinearity ($A_{2,m}$) is not large compared to the diffracted system-generated nonlinearity ($A_{2,0}$), the measured β will be dominated by the system nonlinearities. In order to increase measurement sensitivity for the longitudinal waves, the frequency needs to be much higher, since $\beta \propto \omega^2$. However, at higher frequencies, the measurements would also be very sensitive to contact conditions due to the smaller wavelength, making a repeatable measurement more difficult to attain.

Note that the system nonlinearity generated in the Rayleigh wave experiments also has the propagation distance through the wedge to diffract and also attenuate. It is likely that the system nonlinearity that is actually excited in the sample is much

lower in the Rayleigh wave measurements due to the portion of the wave propagation through the wedge. These are likely the reasons why the Rayleigh wave measurements showed a change in β in the 17-4PH thermally aged material, but the longitudinal wave measurements did not.

6.3.2 Expected Trends with Nonlinearity

In the early stages of precipitate hardening, strengthening is related to the stress required for dislocations to cut through small coherent precipitates. After precipitates grow beyond a critical radius, r_c, strengthening is associated with dislocations bowing around precipitates, i.e. the Orowan mechanism. A model for strengthening due to small coherent precipitates has been previously applied to precipitate hardening mechanisms in precipitate-hardenable material [151, 152]:

$$\Delta\tau \propto f^{1/2} r^{1/2} \tag{121}$$

where τ is the flow stress, f is the volume fraction of precipitates and r is the precipitate radius. The change in hardness is assumed to be proportional to the increase in yield stress due to precipitate strengthening, so the relation of hardness to precipitate parameters has been shown [151, 152] to be:

$$\Delta\tau \propto \Delta H_v \propto N^{1/2} r^2 \tag{122}$$

where N is the number density of precipitates, and H_v is the Vickers hardness. This assumes precipitates are spherical, such that $f = N\,(4\pi/3)\,r^3$. Considering the theory for precipitate-pinned dislocation contribution to nonlinearity as described by Equation 28, the expected relation of β to changes in hardness due to precipitation is

$$\Delta\beta \propto \frac{r^{13/3}}{H_v^{2/3}} \tag{123}$$

If the radius of precipitates is constant over increasing heat treatment time, then the change in acoustic nonlinearity parameter can be related to increasing hardness by:

$$\Delta\beta \propto \frac{1}{H_v^{2/3}} \tag{124}$$

6.3.3 Interpretation of Rayleigh wave results

The results of measured β with Rayleigh waves is plotted against the hardness data in Figure 32. If we assume the radius of the precipitates is roughly constant over heat treatment times from 0-6 hours, then the measured β should be linearly proportional to $1/H_v^{2/3}$. Further, the slope of the resulting linear fit between β and $1/H_v^{2/3}$ should be proportional to $r^{13/3}$. That the relation between β and $1/H_v^{2/3}$ for the air cooled bar samples is in fact linear supports the assumption that the radius is roughly constant over heat treatment time. So, the relative change in radius of the precipitates between the air cooled and water quenched states can be estimated by comparing the slopes of the linear fit between β and $1/H_v^{2/3}$. Using this method, it is estimated that the precipitates in the 17-4PH air cooled samples are about 30% larger in radius than precipitates in the 17-4PH water quenched samples. A larger radius of precipitates in the air cooled state is consistent with the higher measured β in this as-is sample compared to the water-quenched sample.

Note that this is an extremely rough estimation and it is based off a linear fit from only two points available for the water-quenched specimen. Clearly more data is necessary to clarify, with any certainty, the relation between β, hardness, and the radius of the precipitates present in the thermally aged microstructure. Nevertheless, this model and method could be used to extract precipitate information if assumptions and estimations are validated by microstructural characterizations.

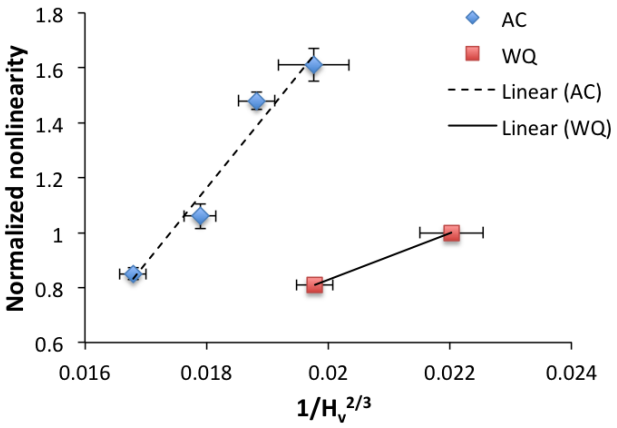

Figure 32: Normalized measured β with Rayleigh waves plotted against $1/H_v^{2/3}$, after Equation 123.

6.4 Summary

This section investigated surrogate sample sets of Fe-Cu material and 17-4PH, which are known to produce copper precipitates during thermal aging. These results can be used to investigate the effects of the copper precipitates on measured β for the irradiated material, and begin to deconvolve different microstructural effects due to irradiation on β. Investigations into 17-4PH stainless steel material showed successful heat treatments of samples designed for both longitudinal and Rayleigh wave measurements. Hardness and TEP measurements provided indirect evidence of increasing amounts of precipitation induced during increasing times of thermal aging at 400°C. Rayleigh wave measurements of β decreased with increasing heat treatment time of 17-4PH stainless steel, which is consistent with the precipitate-pinned dislocation contribution to β. However, longitudinal wave measurements of β showed little detectable change, compared to the measurement sensitivity, in the same samples. A model relating hardness to number density and radius of precipitates is used to estimate differences in precipitate radius due to different initial cooling rates following solution annealing.

CHAPTER VII

EXPERIMENTAL RESULTS: IRRADIATED MATERIAL

7.1 Overview

This chapter presents the experimental results of the irradiated RPV steel material. The main focus of the chapter is the nonlinear ultrasonic measurements of β on a series of samples irradiated at increasing levels of neutron fluence, at different irradiation temperatures and of different material compositions. Results of these measurements show the dependence of β on these irradiation parameters. Results of previously published material properties of the investigated samples, as well as small-angle neutron scattering measurements of precipitate parameters for some of the samples, are also presented for comparison. Finally, neutron diffraction measurement results are presented, the purpose of which was to measure dislocation density in the irradiated samples, although results from this study were inconclusive.

7.2 Material Samples

Nonlinear ultrasonic (NLU) measurements were made on a series of irradiated RPV steel samples. The material sample matrix used enabled an investigation into a variety of effects such as neutron fluence, material composition, irradiation temperature, and to a small extent neutron flux. Experiments were run on two sets of RPV reference steel materials referred to as "JRQ" and "JFL." Note that these materials were used in a previous International Atomic Energy Agency (IAEA) investigation [153]. These steels are ASTM standard A533B Cl.1 (IAEA reference material code "JRQ") and A508 Cl.3 (IAEA reference material code "JFL"), with chemical compositions shown in Table 5, and they have been reported on in the literature [52, 86, 88, 153]. JRQ

Table 5: Chemical composition (wt.%) of JRQ and JFL materials.

Material	C	Si	Mn	Cr	Mo	Ni	P	Cu	S
JRQ	0.18	0.24	1.42	0.12	0.51	0.84	0.017	0.14	0.004
JFL	0.17	0.25	1.42	0.16	0.52	0.75	0.004	0.01	0.002

was manufactured as a rolled plate with final thickness of 225mm, and received the following heat treatments comprising the initial material state: solution annealed at 880°C, water cooled, treated at 665°C for 12 hours, then held at 620°C for 40 hours. JRQ had an inhomogeneous microstructure, with fairly large prior austenite grain size of about $27 \pm 14\mu$m [87]. JFL is a forged steel and received the following heat treatments comprising the initial material state: solution annealed at 880°C for 9 hours then water cooled, then held at 640°C for 9 hours, then air cooled. JFL had a finer grain structure with grain size reported to be $11 \pm 6\mu$m [87]. The main differences between these two materials are their Cu and P content; JRQ contains a higher concentration of Cu (0.14 wt.%) and P (0.017 wt.%) than JFL (Cu: 0.01 wt.%, P: 0.004 wt.%). Samples were irradiated at two separate irradiation temperatures: 255°C and 290°C. The full matrix of sample conditions is given in Table 6 [115].

Samples irradiated at 290°C were irradiated in the 10 MW (thermal) SAPHIR reactor at Paul Scherrer Institute (PSI), at an irradiation temperature of 290°C and at a neutron flux of approximately 5×10^{12} n/cm^2–s. These samples were part of a previous study with PSI and Oak Ridge National Laboratory (ORNL) [86, 88]. Samples were irradiated to a total neutron fluence of $0.5 - 5.0 \times 10^{19}$ n/cm^2, and some samples were given an annealing treatment of 460°C/18h when 50% of the target fluence was reached. Two other samples were then given a second annealing treatment of 460°C/18h after the full neutron fluence was reached. A total of five sample conditions at 290°C were investigated, all JRQ material, referred to as heat 1. Note that the sample designations use the following abbreviations: unirradiated

(U), irradiated (I), annealed (A), and re-irradiated (R). The sample geometry was a broken half of a standard Charpy V-notch sample, with dimensions of 10 mm x 10 mm x 27 mm, with wave propagation through one of the 10 mm dimensions, which was kept consistent among all samples and measurements. Sample surfaces were hand polished with up to 600 grit polish paper and cleaned in an ultrasonic bath. Two broken Charpy halves at each of the five conditions were measured. The only unirradiated JRQ sample available from this heat (i.e. set of samples) for NLU measurements was half the thickness of the broken Charpy half - with dimensions of 10 mm x 5 mm x 27 mm. This thickness difference was accounted for in the NLU measurements, as described below.

Samples irradiated at 255°C were irradiated at the Rheinsberg power reactor to two fluence levels, up to a neutron fluence of 10^{20} n/cm^2 (E > 1 MeV). Two different materials were investigated – JRQ (heat 2) and JFL – so a total of 4 sets of irradiated samples were measured, and three samples were measured in each sample set. The sample geometry was a standard Charpy-V sample (10 mm x 10 mm x 55 mm), with wave propagation consistently oriented through one of the 10 mm dimensions. Four separate unirradiated Charpy samples of both JRQ and JFL material were measured, with the same geometry as the irradiated samples in this set (full Charpy-V samples). Prior to NLU measurements, the unirradiated specimens were wet ground with 600 grit abrasive paper and the irradiated specimens were wet ground with a specially designed grinding machine with 240 grit abrasive paper.

7.3 Nonlinear Ultrasonic Results

Results for the measured β as a function of increasing fluence and the influence of post-irradiation annealing and re-irradiation of JRQ material irradiated at 290°C are given in Figure 33 [115]. Each data point represents an average over three separate measurements on the same sample at the same location, and error bars indicate

Table 6: Conditions for samples undergoing irradiation, post-irradiation annealing, re-irradiation, and re-annealing. Neutron fluence and flux levels are all in terms of neutron energies of E > 1 MeV.

Material	Irrad. Temp.	Abbrev.	Flux (10^{12} n/cm^2)	Irrad. (10^{19} n/cm^2)	Anneal	Re-irrad.	Re-anneal
JRQ	–	U	–	–	–	–	–
(heat 1)	–	UA	–	–	460C/18h	–	–
	290°C	IAR,0.5	5.0	0.25	460C/18h	0.25	–
	290°C	IAR,1.7	5.0	0.85	460C/18h	0.85	–
	290°C	IARA,1.7	5.0	0.85	460C/18h	0.85	460C/18h
	290°C	I,5	5.0	–	–	–	–
	290°C	IA,5	5.0	5.0	460C/18h	–	–
JRQ	–	U	–	–	–	–	–
(heat 2)	255°C	I,5.4	3.01	5.4	–	–	–
	255°C	I,9.8	5.37	9.8	–	–	–
JFL	–	U	–	–	–	–	–
	255°C	I,5.1	2.82	5.1	–	–	–
	255°C	I,8.6	4.74	8.6	–	–	–

one standard deviation from the mean. Separate data points for the same sample condition represent measurements on separate Charpy halves of the same sample condition, or measurements at different locations along the length of the Charpy half. All measurements are normalized to a baseline of β_0, which is the measured β of the unirradiated condition for JRQ heat 1. The results in Figure 33 show little variation among locations and between different sample halves when compared to the changes due to irradiation and annealing; these spatial and sample variations in the same Charpy sample are shown to be insignificant. The measured β increased from the unirradiated state to the maximum neutron fluence, with a maximum increase of 18% at 5×10^{19} n/cm^2 (E > 1 MeV). Results show a decrease in measured β from the irradiated condition (I or IAR) to the annealed condition (IA or IARA) a 23.2% decrease due to annealing in the I,5 and IA,5 samples, and a 25.7% decrease due to annealing in the IAR,1.7 and IARA,1.7 samples. A summary of these changes in

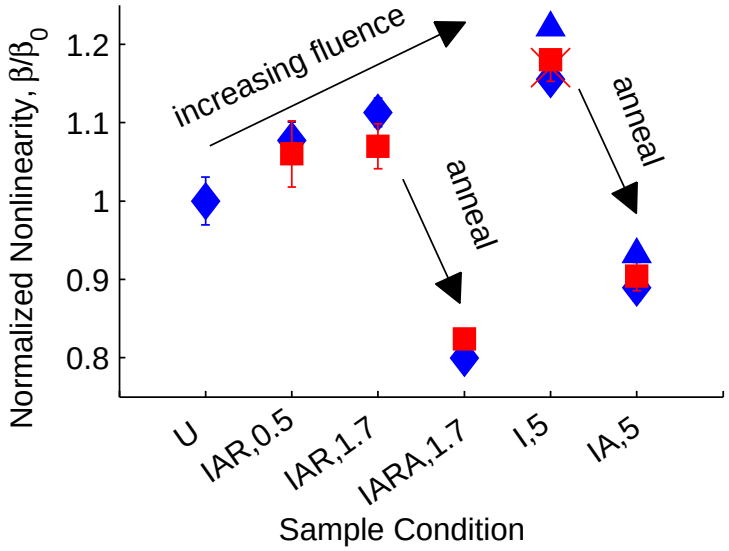

Figure 33: Results of measured β for irradiated, annealed, re-irradiated, and re-annealed JRQ steel, over increasing neutron fluence at T_i = 290°C. and showing effects of annealing. Data points represent measurements on the first Charpy half at location 1 (◆) and location 2 (▲), and on the second Charpy half at location 1 (■) and location 2 (✕).

Table 7: Change in β due to increased neutron fluence and annealing of JRQ for T_i = 290°C.

Total Neutron Fluence	$\Delta\beta/\beta_0$ from irradiation	$\Delta\beta/\beta_0$ from annealing
0.5×10^{19} n/cm^2	+7%	–
1.7×10^{19} n/cm^2	+9%	-25.7%
5×10^{19} n/cm^2	+18%	-23.2%

β due to neutron fluence and then due to annealing is given in Table 7. Note that the intermediate anneal in samples IAR,0.5 and IAR,1.7 effectively recovered most of the irradiation-induced embrittlement during the first irradiation to half the target fluence [88], so a more representative value for the neutron fluence of these samples in terms of β might be half the fluence listed in Table 7.

The dependence of β on neutron fluence for RPV material irradiated at 255°C is shown in Figure 34 [128, 129], and summarized in Table 8. Each data point in Figure 34 represents separate measurements on three different samples of the same

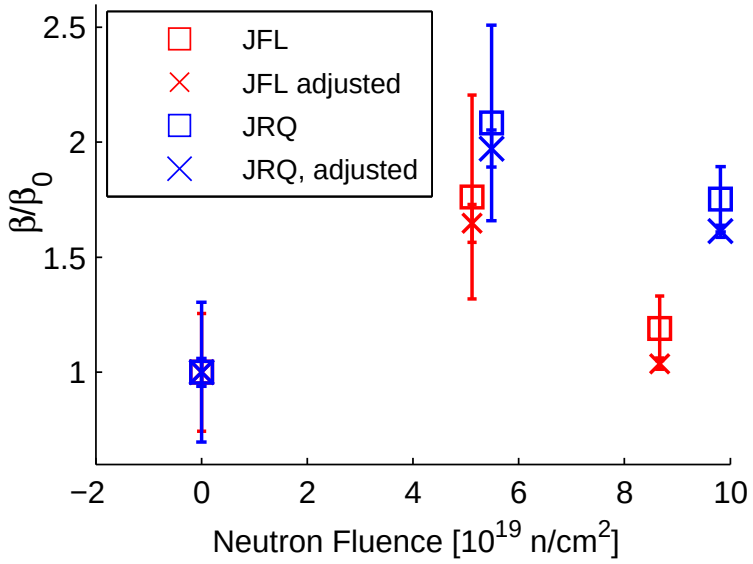

Figure 34: Dependence of β on neutron fluence for JRQ and JFL steel irradiated at $T_i = 255°\text{C}$.

Table 8: Change in β/β_0 due to increased neutron fluence of JRQ and JFL for $T_i = 255°\text{C}$.

Material	Total Neutron Fluence (E > 1 MeV)	$\Delta\beta$
JRQ	5.4×10^{19} n/cm^2	+97%
	9.8×10^{19} n/cm^2	+61%
JFL	5.1×10^{19} n/cm^2	+65%
	8.6×10^{19} n/cm^2	+4%

material and fluence level, and the error bars represent the standard deviation from the mean of β for the three samples (except for the unirradiated samples, where four samples were measured and averaged). All measurements are normalized to a baseline, β_0, which is the measured β of the unirradiated condition for each material. One set of data points represents the results adjusted for surface roughness effects. The variation in the raw measured β for different specimens at the same fluence level ranged from 8–30%, which was found to be primarily due to surface roughness effects. This was confirmed by experiments on unirradiated samples polished to decreasing levels of surface roughness. See Appendix B for details of the surface roughness adjustments. The remainder of the measurement variability was caused by slight variations in coupling and clamping force. Note that linear ultrasonic measurements of longitudinal wave velocity and the attenuation coefficient were also made on these JRQ and JFL samples, and details of these measurements and results are given in Appendix C. Ultimately, measurements of β showed a much-improved sensitivity to increases in neutron fluence compared to the velocity and attenuation.

While β for both JRQ and JFL is normalized by the measured β in the unirradiated state, note that the β_0 for JFL material was 17% higher than for unirradiated JRQ. There is an increase in β from the unirradiated state to the medium dose samples, then a decrease from medium dose to high dose. It is important to note that the measured β for the high dose samples is still larger than the unirradiated samples. The initial increase in β is larger in the JRQ samples than the JFL samples. It is important to note that the same trend in β as a function of fluence is seen for the two different types of steel. The results in Figure 34 and 33 were corrected for diffraction of the first harmonic wave propagating through material with slightly varying thickness.

Results for measured β for JRQ and JFL material at $T_i = 255°\text{C}$ as a function of increasing neutron fluence are shown together with the results of measured β for

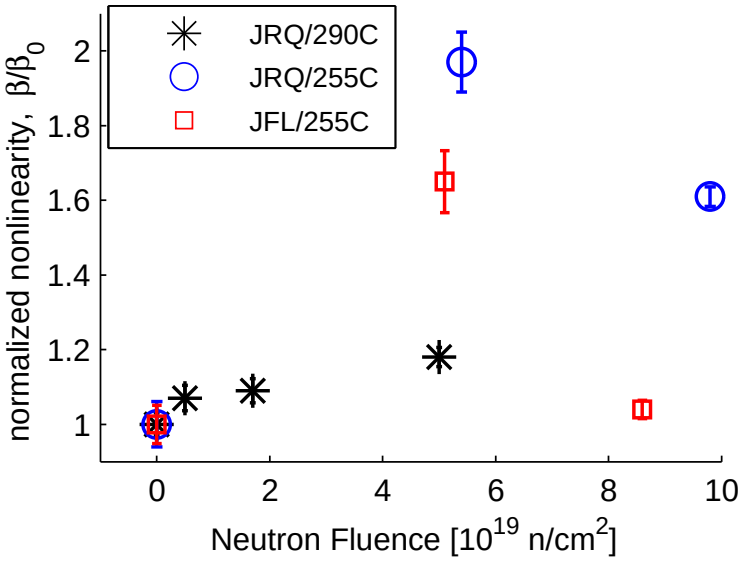

Figure 35: Influence of increasing neutron fluence (E > 1 MeV) on β , for JRQ and JFL at $T_i = 255°C$ and 290°C. Each dataset is normalized to the measured β in the unirradiated state, β_0. JRQ samples irradiated at 290°C to 0.5×10^{19} and 1.7×10^{19} n/cm^2 received an intermediate anneal at 50% target fluence.

irradiated JRQ at $T_i = 290°C$ in Figure 35 [115]. Results for JRQ at $T_i = 290°C$ in Figure 35 have here been averaged over all measurements on different Charpy halves and different locations. Note that light water reactor pressure vessels typically operate at 290°C±30°C, so the irradiation temperatures of the two data sets considered in this study approximate vessel operational conditions [41]. These results are presented in terms of a normalized β to the unirradiated state in each sample set, i.e. $\beta_i/\beta_0 = (A_2/A_1^2\omega^2)_i \,/\, (A_2/A_1^2\omega^2)_0$. Since the radial frequency ω, where $\omega = 2\pi f$, was the same for the experiments on the unirradiated samples (measurement of β_0) and the irradiated samples (measurement of β_i), the dependence of β on ω is eliminated. In this way, the different excitation frequencies used in the different measurement sets ($f = 2.25$ MHz for $T_i = 255°C$ and $f = 3.3$ MHz for $T_i = 290°C$) does not influence the relative comparison of the measured β. The values of measured β that are not normalized are given in Table 9 for reference, but note that values of β for samples irradiated at 290°C cannot be directly compared with raw β values for samples irradiated at 250°C due to the differences in experimental input parameters. The

differences in fundamental frequency were due to limitations in equipment during earlier experiments - higher frequencies are more ideal for the shorter wave propagation distances encountered in these experiments, since the shorter wavelength allows more cycles and thus higher amplitude of A_2, given the same sample thickness. The combination of linear and nonlinear diffraction effects as described in Section 5.2.3.2 were found to be negligible; details can be found in Appendix A.

The trend of β as a function of neutron fluence for the irradiated JRQ at $T_i = 290°C$ is similar to the trend for samples irradiated at 255°C [128] and as seen in Figure 35 an increase in β up to a medium fluence of roughly 5×10^{19} n/cm^2. However, the increase in β is much more pronounced in the samples with $T_i = 255°C$, even in the low-copper alloy of JFL. At a neutron fluence of 5×10^{19} n/cm^2, it is shown that at $T_i = 255°C$, β increased by almost 100% in JRQ and 65% in JFL, while at $T_i = 290°C$, β increased by only 18% in JRQ, all from the respective unirradiated conditions of each sample set. These results show that the acoustic nonlinearity parameter strongly depends on the irradiation temperature as well as the level of neutron fluence.

7.3.1 Determination of β_0 for JRQ Heat 1

The only unirradiated JRQ heat 1 sample available for NLU measurements was half the thickness of the irradiated samples for $T_i = 290°C$, such that the wave propagation distance was 5mm in the unirradiated JRQ heat 1 sample, compared to 10mm in the irradiated/annealed JRQ heat 1 samples at $T_i = 290°C$. Since β depends linearly on propagation distance, this thickness difference must be accounted for. Another effect of the thinner sample on the measurements was that a smaller number of cycles had to be used for the sinusoidal excitation, since the maximum cycles possible in terms of the thickness (such that reflections from the incoming wave did not interfere with the received signal) were used for the measurements in the irradiated samples to obtain maximum acoustic energy – specifically, only 6 cycles of a 3.3MHz ultrasonic

Table 9: Measured β in all irradiated sample sets.

Material	Sample.	β_{raw}
JRQ	U*	1.307 e-5
(heat 1)	UA*	1.349 e-5
	IAR,0.5	1.407 e-5
	IAR,1.7	1.455 e-5
	IARA,1.7	1.045 e-5
	I,5	1.51 e-5
	IA,5	1.163 e-5
JRQ	U	1.949 e-6
(heat 2)	I,5.4	3.844 e-6
	I,9.8	3.144 e-6
JFL	U	2.357 e-6
	I,5.1	3.883 e-6
	I,8.6	2.445 e-6

*Values adjusted for 5mm thickness effects, as described in Section 7.3.1 .

wave could fit in the thickness of the 5mm sample (with 4 somewhat steady-state cycles extracted for the FFT and subsequent analysis), compared to 12 cycles of a 3.3 MHz ultrasonic wave that could fit in the thickness of the 10mm samples. A representative time signal of a 3.3 MHz wave propagated through the 5mm-thick unirradiated JRQ heat 1 sample is shown in Figure 36. So, the difference in β due to the different thickness could not be accounted for by simply scaling the measured β by the thickness difference, as is indicated by Equation 7.

To determine the β_0 from the 5mm unirradiated sample (sample designation: U,JRQ1), an unirradiated sample from JRQ heat 2 (sample designation: U,JRQ2) with thickness of 10mm was used as a comparison sample. The procedure for the thickness correction was as follows. A measurement of β was made on sample U,JRQ2 with propagation distance of 10mm and with the same input parameters (12 cycles, 3.3 MHz excitation) as the irradiated JRQ heat 1 samples, to produce the measurement $\beta_{2,10}$. Then, sample U,JRQ2 was cut to a thickness of 5mm, and measurements of β

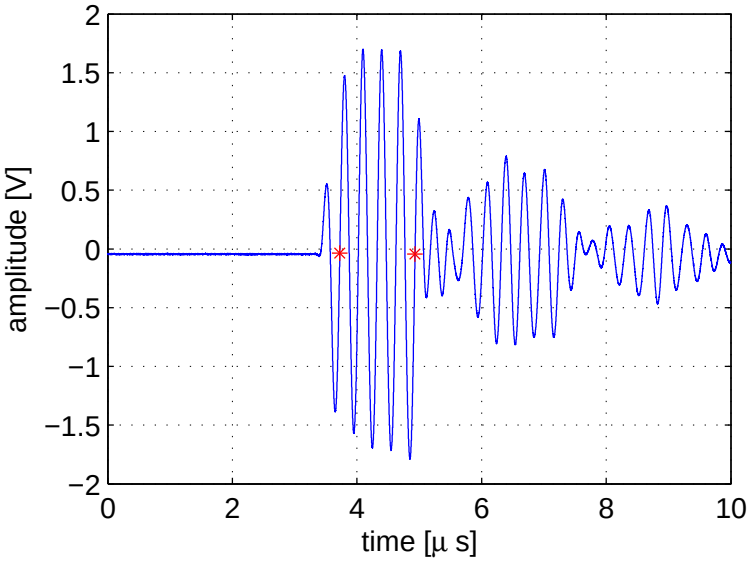

Figure 36: Representative time signal of a 3.3 MHz propagated wave through the 5mm-thick unirradiated JRQ heat 1 sample. The red points represent the bounds for the section of the signal extracted for the FFT.

were made on sample U,JRQ2 (now with wave propagation distance of 5mm), using input parameters of 5 cycles and 3.3 MHz excitation. Then, a measurement of β was made on sample U,JRQ1 (the 5mm thick sample) with the same input parameters used for $\beta_{2,5}$ - 5 cycles and 3.3 MHz excitation, to produce the measurement of $\beta_{1,5}$. The value for $\beta_{1,10}$ - measured β for the unirradiated condition of JRQ heat 1 to be used as the baseline for the irradiated JRQ heat 1 samples - was then calculated by:

$$\beta_{1,10} = \frac{\beta_{1,5}}{\beta_{2,5}} \beta_{2,10} \tag{125}$$

This value of $\beta_{1,10}$ is used as the baseline β_0 for the JRQ samples irradiated at 290°C, and this expression was used to calculate the raw β for the unirradiated JRQ heat 1 condition given in Table 9.

7.4 Previous Material Characterizations

Measurements of macroscopic material properties such as tensile tests and Charpy-V impact tests were conducted previously, and are reproduced here for comparison to the nonlinear ultrasonic measurements. Sample material properties are given in

Table 10: Measured material properties of samples for NLU, based on previous material characterizations. Neutron fluence levels are in terms of neutron energies of E > 1 MeV (from Zurbuchen et al. 2009, Nanstad et. al 2004, and Nanstad et al. 2005).

			Tensile Tests		Charpy-V Tests	
RPV Material	Irrad. Temp.	Abbrev.	σ_{ys} [MPa]	UTS [MPa]	T_{41J} [C]	USE [J]
JRQ (heat 1)	–	U,JRQ1	470	650	-28	200
	290°C	IAR,0.5	471	∼648	-1	∼235
	290°C	IARA,0.5	–	–	-43	∼290
	290°C	IAR,1.7	490	∼680	28	∼205
	290°C	IARA,1.7	–	–	-18	∼230
	290°C	I,5	∼581	–	68	∼170
	290°C	IA,5	–	–	-22*	–
JRQ (heat 2)	–	U,JRQ2	484	618	-13	192
	255°C	I,5.4	770	847	167	133
	255°C	I,9.8	843	904	209	111
JFL	–	U,JFL	470	614	-43	211
	255°C	I,5.1	587	706	9	196
	255°C	I,8.6	640	746	36	196

*Estimated based on 89% recovery of ΔT_{41J} [88].

Table 10, which are based on previous measurements and characterizations found elsewhere [86–88].

Previously, small angle neutron scattering experiments were conducted on the JRQ and JFL material irradiated at 255°C [52]. Results showed an increasing volume fraction of precipitates with increasing neutron fluence. Precipitate radius was measured at an average of 1nm in all irradiated conditions. The volume fraction of precipitates in JRQ was about an order of magnitude greater than in JFL. Table 11 shows the results from these previous measurements [52], as well as calculated number densities of precipitates assuming spherical precipitates, such that $f_p = V_p N_p = 4/3\pi r_p^3 N_p$.

Previous atom probe tomography experiments were done on some of the JRQ samples irradiated at 290°C [82]. From these measurements, precipitate number densities and radii of gyration were estimated. The estimates for these precipitate

Table 11: Results of previous SANS measurements of precipitate volume fraction and average radius, and calculated number densities, for JRQ and JFL irradiated at 255°C (from Ulbricht et al. 2005).

Material	Neutron Fluence	f_p (vol. %)	$\bar{r}_p$ (nm)	N_p (1/m^3)
JRQ	5.4×10^{19} n/cm^2	0.34	1.0	8.12×10^{23}
	9.8×10^{19} n/cm^2	0.50	1.0	11.94×10^{23}
JFL	5.1×10^{19} n/cm^2	0.02	1.0	0.48×10^{23}
	8.6×10^{19} n/cm^2	0.09	1.0	2.15×10^{23}

Table 12: Results of previous APT measurements of *estimated* precipitate number densities and average radius, for some of the JRQ samples irradiated at 290°C (from Miller et al. 2006).

Material	Condition	Total Neutron Fluence	N_p (/m^3)	$\bar{r}_p$ (nm)
JRQ	IAR,1.7	1.7×10^{19} n/cm^2	1.3×10^{23}	0.9 ± 0.4
	IARA,1.7	1.7×10^{19} n/cm^2	0.1×10^{23}	1.6
	I,5	5.0×10^{19} n/cm^2	3.0×10^{23}	1.1 ± 0.1
	IA,5	5.0×10^{19} n/cm^2	0.2×10^{23}	1.5 ± 0.1

parameters for the samples relevant to this work are provided in Table 12 [82].

7.5 Neutron Diffraction Measurements

7.5.1 Background

Two sets of neutron diffraction experiments were run at the Los Alamos Neutron Science Center (LANSCE) on both unirradiated and irradiated JRQ $T_i = 255$°C samples, i.e. the same samples used for the nonlinear ultrasonic measurements shown in Figure 34. Room temperature measurements were run on the neutron powder diffractometer (NPDF) on five JRQ samples. Post-processing on experimental results have the potential to give microstructural parameters for samples investigated such as dislocation density and dislocation arrangement. These results could provide inputs into nonlinear ultrasonic models such as the precipitate-pinned dislocation model.

Neutrons exhibit both particle and wave properties, and have a wavelength comparable to interatomic spacings. When a neutron beam is scattered by crystals, there are directions in which the incident plane waves scatter in-phase, leading to peaks at certain positions, corresponding to Bragg's law. The intensity, position, and shape of these peaks can be related to the crystalline structure and other material parameters [154]. Peak position or diffraction angle θ can be related to interplanar spacing d and wavelength of radiation, and specific diffraction angles correspond to specific interplanar spacings. Calculation of diffracted intensity over a range of angles shows peaks at certain positions corresponding to the different lattice planes in the sample. This information can then be analyzed to determine microstructure parameters. Neutron scattering will penetrate the entire sample volume, so results are a volume average for the samples. The following describes the NPDF measurements, analysis, and results on JRQ samples.

7.5.2 NPDF Experiments and Results

Room temperature neutron scattering experiments were run on the NPDF on five JRQ samples. Sample JRQ336 was the unirradiated baseline sample. Two samples (JRQ972 and JRQ975) were irradiated to 5.4×10^{19} n/cm^2 (E > 1MeV) ("medium" fluence), and the other two samples (JRQ927 and JRQ928) were irradiated to a neutron fluence of 9.8×10^{19} n/cm^2 (E > 1MeV) ("high" fluence). Samples were cut to a rectangular geometry of 5mm x 5mm x 10mm. Peak intensity data was analyzed in two different ways to obtain dislocation density-related information. In the first analysis, the values of full-width at half maximum (FWHM) were extracted at each peak location. The FWHM is defined as the peak width in degrees at half the peak height. The slope of the best-fit line of the FWHM vs. peak location is proportional to the dislocation density; this plot, termed the Williamson-Hall plot, is shown in Figure 37a for each of the four JRQ irradiated samples plus a silicon standard. The silicon

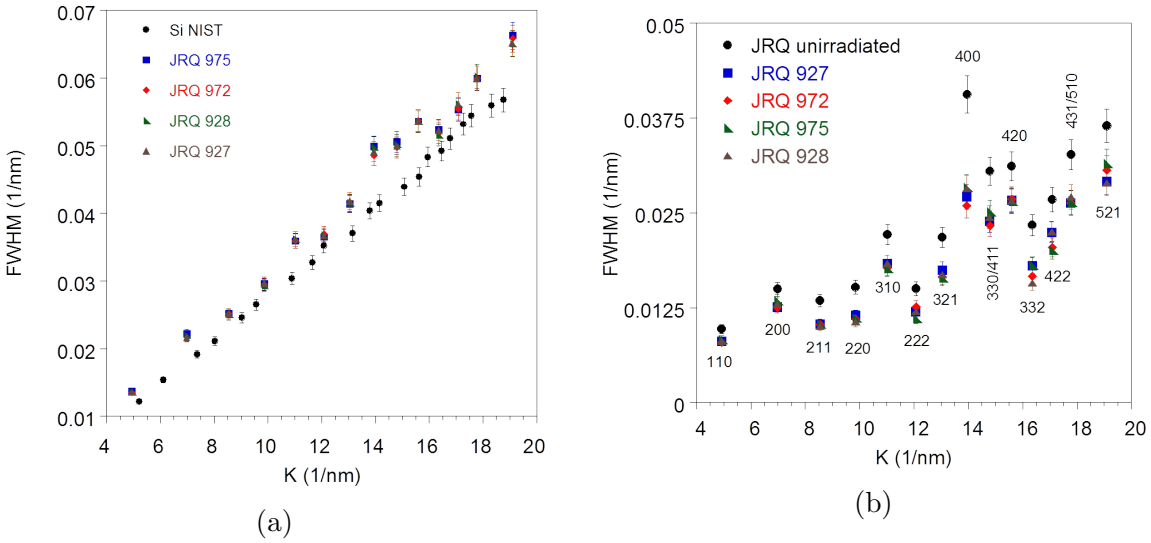

Figure 37: (a) Williamson-Hall plot for medium and high dose JRQ samples and silicon standard, and (b) all samples. Labels indicate hkl lattice planes.

standard measurement shows the contribution to peak broadening from the NPDF instrument. These results show that dislocations contribute to peak broadening since the FWHM is higher in all JRQ samples than the silicon standard, but there is little significant difference between JRQ samples at medium and high fluence. The Williamson-Hall plot for both unirradiated and irradiated samples is shown in Figure 37b. This figures shows the FWHM plotted over $K = 2\sin\theta/\lambda$, where θ is the diffraction angle and λ is the wavelength of neutrons. Note that the instrument broadening is accounted for in these results by subtracting out broadening measured with the silicon standard, and that some peak positions correspond to contributions from two separate lattice planes. While these specific results show a decrease in peak broadening from unirradiated to irradiated state, this change is small and most likely due experimental error, since these samples were measured on two separate run cycles on the NPDF.

A more comprehensive line profile analysis was done using the CMWP (Convolution Multiple Whole Profile) Fit Control [155] software program, which fits the peak intensity data to a theoretical model with which microstructural properties such as

dislocation density, arrangement, and type can be extracted. The details are not given here since the results had large error, due to multiple fit-parameters needed, and the dislocation density of the samples was at the edge of the detection limit of the NPDF. As such, results from these neutron diffraction measurements were not used for model inputs in this work.

7.6 Summary

This chapter presents the experimental results for measured acoustic nonlinearity parameter over increasing neutron fluence in different RPV materials irradiated at different temperatures. The effects of post-irradiation annealing and re-irradiation on measured β are also explored. The main conclusions derived from these nonlinear ultrasonic measurements are as follows:

- β increased up to 100% due to increasing neutron fluence in two RPV materials under different irradiation temperatures, and then decreased at higher neutron fluence.
- The increase in β due to increasing neutron fluence was larger in the JRQ material, which contained higher Cu and P content.
- For similar neutron fluence, the increase in β was larger for a lower irradiation temperature
- Post-irradiation annealing showed a clear decrease in β over different levels of initial neutron fluence.
- Measurements of dislocation density in the JRQ $T_i = 255°C$ samples using neutron powder diffractometry were inconclusive, since the dislocation density was at or below the resolution limit of the NPDF.

CHAPTER VIII

DISCUSSIONS

This chapter provides interpretations of the experimental results on irradiated RPV material, in terms of the analytical models developed in Chapter 4 and microstructural characterizations throughout the current literature. In low-alloy steels under typical RPV conditions, neutron irradiation causes radiation-enhanced diffusion, which results in microstructural features such as copper-rich precipitates, solute clusters, matrix defects in the form of solute-vacancy complexes, and potentially dislocations and interstitial loops [41, 47, 54], as reviewed in Section 3.4. With such a complex microstructure that is still to this day being characterized and understood, it is not possible at this point to present a comprehensive model to describe the changes in β shown in the experimental sections in this work. Therefore, dominant microstructural features in the irradiated material that affect β will be discussed for the different irradiation conditions explored in this work.

8.1 Precipitate Contribution

Considering the model described in Equation 22 for the change in β due to pinned dislocations, and assuming the precipitate-pinned contribution is stronger than other pinning features due to the higher stress induced by the precipitate misfit, β should generally increase by $\exp(-B/N)/N^{1/3}$ below N_{cr}, and decrease by $N^{1/3}$ above N_{cr}, as described in the model presented in Section 4.4. The plot in Figure 38 [115] illustrates this trend, and note that for simplicity we assume $B = 0.33$ such that $\Delta\beta = 1$ when $N/N_{cr} = 1$, and the function is plotted over increasing N normalized by N_{cr}. The plot in Figure 38 shows the function $\Delta\beta = \exp(-0.33/N)/N^{1/3}$. Since the change in β over neutron fluence for $T_i = 255°\text{C}$ changes trend after the medium

fluence of roughly 5×10^{19} n/cm^2, we can infer that N_{cr} occurs roughly around this medium fluence level. Comparison of this model with experimental results suggest that in the JRQ samples irradiated at 290°C, the number density of precipitates is below N_{cr}, which explains the increasing measured β with increasing neutron fluence, due to the likely increasing number density of precipitates. This model qualitatively agrees with the experimental results, but suggests there are other microstructural features that contribute to the total $\Delta\beta$.

Previously, small angle neutron scattering (SANS) experiments were conducted on the same JRQ and JFL samples with $T_i = 255$°C reported on here and previously [128], to quantify these microstructural features. The authors reported an increase in volume fraction of precipitates with constant average radius of about 1 nm with increasing neutron fluence [52]. Specifically, the volume fraction increased from 0.005–0.09 vol.% for neutron fluence of $0.7 - 8.7 \times 10^{19}$ n/cm^2 in JFL, and 0.21–0.5 vol.% for neutron fluence of $0.7 - 9.8 \times 10^{19}$ n/cm^2 for JRQ. Considering only the precipitate-pinned dislocation theory, this would imply that the model predicts $\Delta\beta$ should be lower in JRQ compared to JFL, since JRQ has a higher volume fraction of copper rich precipitates, since the precipitate-pinned dislocation theory predicts $\Delta\beta \propto 1/N^{1/3}$. The model predictions using only the precipitate pinned dislocation contribution to β are shown in Figure 39, using SANS results as inputs into Equation 29. Here, $\Delta\beta$ is normalized by the predicted β for JRQ irradiated to 0.7×10^{19} n/cm^2, and note this low neutron fluence sample (and the corresponding one for the JFL material) was not available for NLU measurements. However, experimental evidence in Figure 35 shows the *opposite* trend when comparing the two different RPV materials - $\Delta\beta$ is larger for JRQ. Differences between the two materials such as vacancy-type features not detected by SANS, dislocation density, grain structure (which would influence general dislocation pinning effects by grain boundaries), point defects and other defects, and a different N_{cr} could all contribute to this discrepancy. This again suggests that

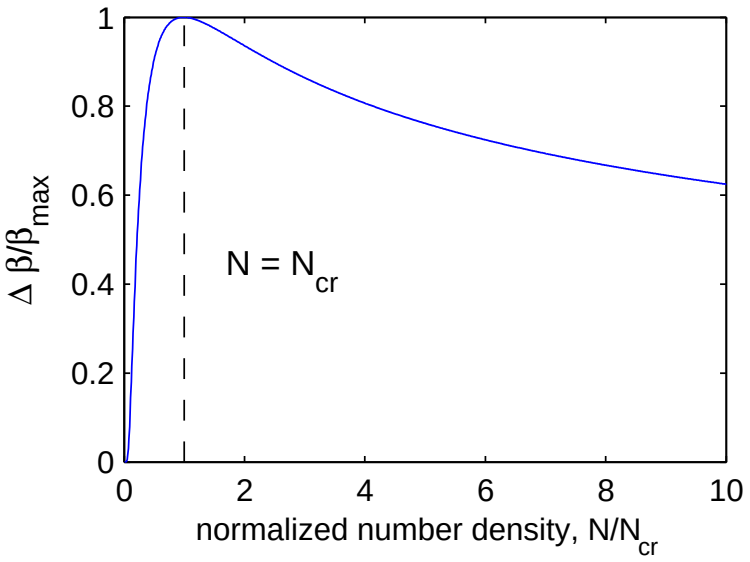

Figure 38: Predicted trend of $\Delta\beta$ (normalized by β_{max}) as a function of number density of precipitates, normalized by N_{cr}, assuming trend is dominated by precipitate-pinned dislocations (i.e. second term in Equation 61).

there are other microstructural features that contribute to the total $\Delta\beta$, and more microstructural characterizations are needed to explain this.

Microstructural changes over increasing neutron fluence are dependent on many other factors such as neutron flux, irradiation temperature, and material composition, and the effects of one irradiation parameter depends on other variables. For example, a rapid increase, followed by saturation, followed by slow coarsening and a decrease in number density of precipitates, was predicted by models and confirmed experimentally for 0.3% Cu RPV steels irradiated at low neutron flux and an irradiation temperature of 290°C [47]. As another example, it has been shown that an increase in the nickel content in irradiated RPV material correlates to an increase in both average radius and number density of copper-rich precipitates [46]. Further, changes in the irradiation temperature, particularly in the range of about 250°C–300°C in the high-flux regime of test reactors [156], as well as the neutron flux has been shown to strongly affect how the microstructure evolves over increasing neutron fluence [47, 48, 84]. The following sections provide a discussion on other possible

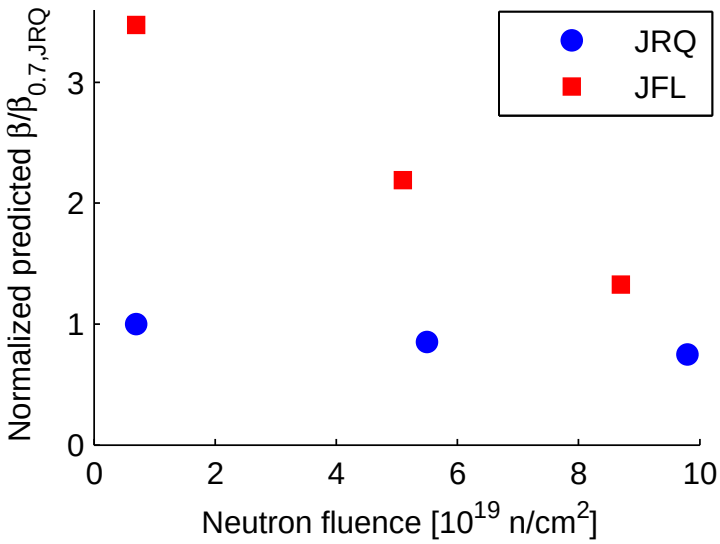

Figure 39: Predicted $\Delta\beta$ using SANS inputs of precipitate volume fractions and average radius for JRQ and JFL samples irradiated at 255°C, using only precipitate pinned dislocation model. $\Delta\beta$ is normalized by the predicted β for JRQ irradiated to 0.7×10^{19} n/cm^2, and note this low neutron fluence sample (and the corresponding one of JFL material) was not available for NLU measurements.

contributions of microstructural features to β, in terms of reported microstructural evolutions over the relevant irradiation conditions in the current study, and in light of the newly developed analytical models presented in Chapter 4.

8.2 Effects of Neutron Flux

The effect of higher fluxes typical of test reactors depends on the combination of copper content, irradiation temperature, and neutron fluence [47, 65]. It has been shown that in low Cu steels, higher flux typical of test reactors can produce increased hardening at higher fluence due to an increased amount of unstable matrix defects (UMDs). In RPV steels with greater than 0.1% Cu, these UMDs act as sinks to delay precipitation from radiation-enhanced diffusion [47], and thus delay or reduce hardening. This flux-dependent regime has been estimated to begin at fluxes above about 5×10^{11} n/(cm^2-s) at $T_i = 290$°C [48]. It has been shown that the dose rate effect of delaying precipitation increases with increasing alloy content, particularly

with increasing Ni and Mn content. Higher solute content causes a higher amount of radiation-induced defects to be trapped by solutes, which increases the rate of recombination of defects [48], thus delaying precipitation. In contrast, in low Cu steels, higher flux typical of test reactors can produce increased hardening at higher fluence due to an increased amount of matrix defects. It is likely that these flux-related effects occur and cause different effects in the trend of $\Delta\beta$ in the lower temperature samples of irradiated JRQ and JFL at $T_i = 255°C$.

Recall that the JFL samples contained 0.01% Cu (low-copper steel), and the JRQ samples contained 0.14% Cu (medium-copper steel). It has been shown that the dominating hardening mechanisms in low-copper steels are other defects and matrix features such as point defect clusters and manganese-nickel precipitates [46,47,65]. It is plausible that these defects, as well as UMDs as suggested in [47,51], have formed in the high fluence samples of the low-Cu JFL material, creating more pinning points for dislocations and thus causing a decrease in β, which would align with the experimental results.

8.3 Effects of Composition

In low-Cu materials, the dominant hardening mechanism is matrix features such as vacancy complexes [46, 47, 51]. The effects on β of these features would more closely approximate the vacancy contribution than the precipitate contribution. In these materials, where the number density of copper-rich precipitates is significantly low, one might expect a stronger contribution to β compared to that of a medium-Cu material with significantly higher number density of copper-rich precipitates, as previously mentioned. However, this is unlikely the case, since other matrix features, in addition to possible UMDs suggested previously, are likely present in the low-Cu material. These features would: (1) provide *additional* pinning points to dislocations that are already pinned, which will decrease the dislocation pinning length and thus

decrease the magnitude of β (if the number of pinning points is greater than N_{cr}), and (2) would result in a lower local stress field compared to the precipitates, as evident in ratio of misfit stresses in Equation 110. In the current experimental results, β is likely influenced by these features in the irradiated low-Cu JFL samples. The change in β is likely due to a combination of precipitates (as previously measured by SANS [52], which were shown to be an order of magnitude lower in number density and volume fraction than in the irradiated medium-Cu JRQ) and other dislocation pinning points such as vacancy-solute clusters. Other microstructural characterizations, such as positron annihilation spectroscopy could quantify the vacancy-type features in the irradiatied JFL samples, and be used as inputs into the two-feature pinning model described in Section 4.6.4.

8.4 Effects of Irradiation Temperature

Irradiation hardening due to matrix features (namely vacancy-solute cluster complexes) has been shown to increase with decreasing irradiation temperature, since matrix features are more thermally stable at lower temperatures [47, 84]. A lower irradiation temperature has also been shown to increase both the hardening due to CRPs and number density of precipitates N_p, while decreasing the radius of the precipitates in the range of T_i = 270–310°C [46]. While counter-intuitive, this is due to higher Cu solubility at increasing temperatures, which decreases the nucleation rate of copper-rich precipitates and thus decreases N_p. The larger radius of precipitates at higher irradiation temperatures is perhaps not counter-intuitive, but it has been suggested that these larger precipitates could potentially have a decreased hardening efficiency [46].

This indicates that there could be a smaller number density of precipitates in the JRQ at 290°C compared to JRQ at 255°C at the common neutron fluence of 5×10^{19} n/cm^2. Therefore, it can be assumed that the critical number density of

precipitates, N_{cr}, has not yet been reached in the JRQ $T_i = 290°C$ samples and thus β is expected to generally increase with increasing N, since $N < N_{cr}$ in this case. This can potentially explain the differences in $\Delta\beta$ in JRQ at roughly 5×10^{19} n/cm^2 for $T_i = 290°C$ ($\Delta\beta = +18\%$) and $T_i = 255°C$ ($\Delta\beta = +97\%$). However, it should be noted that high flux could counteract the effect of higher temperatures, since this combination of high flux and higher temperature would decrease the recombination rate of defects, potentially creating more nucleation sites for CRPs. Small angle neutron scattering (SANS) measurements on JRQ irradiated at 290°C could address these points.

8.5 Effects of Phosphorous in JRQ on $\Delta\beta$

The JRQ material contains 0.017 wt.% P, which has been shown to be a sufficient amount of P to influence the irradiated microstructure. Atom probe tomography data has shown that irradiation can cause phosphorous segregation to dislocations, which can contribute to irradiation-induced hardening [46, 86]. In Section 4.5, it was shown that interstitials segregated to dislocations can produce a change in magnitude of the acoustic nonlinearity. It is of particular interest to point out that the effect of dislocations trapped by interstitial rows and pinned by precipitates can become quite significant above a certain critical number density of precipitates, as shown in Figures 11 and **??** in Section 4.6.2. If 100% of dislocations are trapped by interstitial rows, then this critical number density of precipitates was calculated to be about 1.2×10^{23} m^{-3}. The number density of precipitates in the irradiated JRQ material investigated in this work is well above this critical value - as shown in Table 11, the number density was calculated to be between $8 - 12 \times 10^{23}$ m^{-3} for JRQ irradiated at 255°C. At these high number densities, it is likely that any phosphorous segregation to dislocations will produce a significant nonlinear response in terms of increasing the magnitude of β. As shown in Figure 11, even with a volume fraction of trapped

dislocations of 0.1, dislocation-interstitial-precipitate interactions will dominate the precipitate-pinned dislocation response above number densities of about 7×10^{23} m^{-3}, which is lower than the number density of precipitates in JRQ irradiated at 255°C to 5.4×10^{19} n/cm^2.

If we assume that only 1% of dislocations are trapped by interstitial rows, then the nonlinearity parameter β due to the dislocation-interstitial-precipitate effect will be 23% larger at the medium neutron fluence level and 106% larger at the higher fluence than the purely precipitate-pinned dislocation case. This estimation assumes that the segregation of P does not change over increasing neutron fluence. Note that a quantitative analysis of P segregation to dislocations has not yet been realized in the literature, so a quantitative analysis of the effect of P segregation to dislocations to the nonlinear ultrasonic measurements is not possible at this time. Further microstructural characterizations are needed to further explore this effect. The direct effect of P on β could also be explored by irradiating a material with similar composition to JRQ but without phosphorous, and compare the measured change in nonlinearity to the same material but with some added P content, irradiated under the same conditions.

If more microstructural information was known on JFL and JRQ, it might be possible to estimate the volume fraction of dislocations trapped by interstitials. For example, if the number of vacancy-type pinning points in JFL and JRQ was known, the change in β due to defect-pinning of dislocations could be calculated. We can further assume there is no phosphorous segregation to dislocations in JFL due to its extremely low P content compared to JRQ. So by determining the discrepancy between the measured $\Delta\beta$ in JRQ and the expected $\Delta\beta$ due to defect-pinned dislocations, an estimation of the volume fraction of trapped dislocations could be determined. If this were confirmed (which is possible using positron annihilation spectroscopy, since

positrons are sensitive to vacancy-type defects), then nonlinear ultrasonic measurements could even be used as a means of quantifying the P segregation to dislocations during irradiation.

8.6 Post-irradiation Annealing

Post-irradiation annealing (PIA) has been shown to recover some of the irradiation-induced embrittlement in RPV steels [47, 86, 88, 96]. Nanstad et al. [88] conducted Charpy impact testing on the JRQ samples investigated in the current work, and showed almost full recovery of the irradiation-induced ductile-brittle transition temperature shift from the annealing treatment. In a follow-up study, atom probe tomography (APT) experiments showed a decrease in number density of copper-rich precipitates of about an order of magnitude [86]. The remaining precipitates in the microstructure were significantly larger, and were only observed near grain boundaries. Follow-up characterizations are needed to fully quantify the changes in number density and size of precipitates in the PIA state, but the APT results showed that annealing caused most of the copper to dissolve in the matrix, while the remaining copper in precipitates grew and coarsened. This effect of PIA has been shown in other studies, for example with VVER–440 weld material interrogated with APT and positron annihilation spectroscopy (PAS) [83, 97], and with SANS measurements of high-copper RPV weld materials [83].

To isolate contributions to β from annealing effects on the irradiated microstructure, an unirradiated JRQ sample was annealed with the same schedule as the post-irradiation annealing (460°C/18h). A slight increase in β of 7% was measured in the unirradiated and annealed sample, compared to the purely unirradiated sample. These results are shown in Figure 40 [115], in comparison with the change in β due to annealing in the irradiated samples, where a clear decrease of 23–26% was seen from irradiated to annealed state. Since no (or at least very few) precipitates are expected

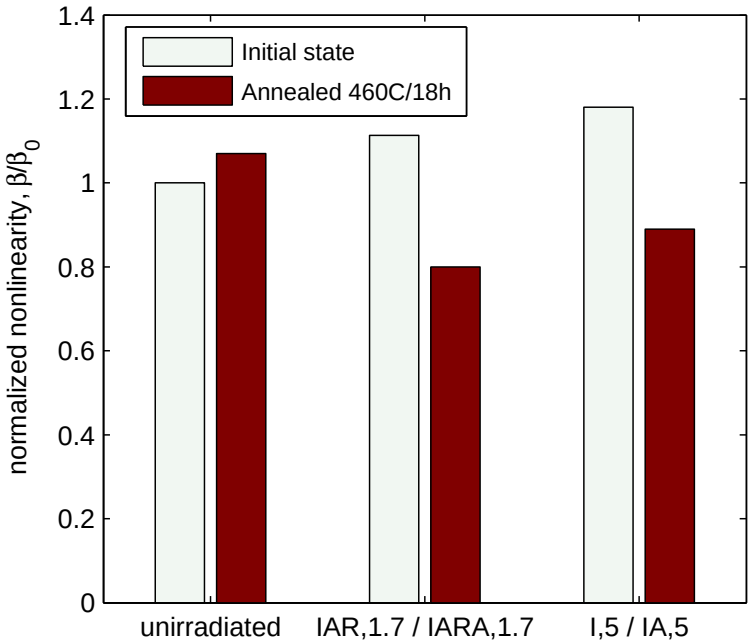

Figure 40: Dependence of β on annealed microstructure for unirradiated JRQ and irradiated JRQ ($T_i = 290°\text{C}$).

to be present in the unirradiated sample, the results clearly show that the change in β from PIA is due to changes specific to the irradiated microstructure.

The number density of precipitates in I,5 and IAR,1.7 samples should be below N_{cr} as defined in Section 4.4. Therefore, as precipitates are removed from the microstructure, N should still be below N_{cr}, and so β should generally decrease as indicated by Equation 61 and Figure 38. Experimental evidence clearly shows this decrease in β. It is also possible that the coarsened precipitates remaining in the annealed microstructure have become incoherent with the matrix. The stress surrounding incoherent precipitates is significantly less than coherent precipitates, such that the precipitate-pinned dislocation model no longer applies.

8.7 Re-irradiation Effects

It has been shown that microstructural evolution during re-irradiation following PIA follows a different path than a purely irradiated microstructure [86, 97]. Nanstad et al. [86] conducted atom probe tomography investigations on the current samples, and

they reported that re-irradiation does cause copper-rich precipitates to form with a number density similar to that in the irradiated only condition, but with a smaller radius. If only considering the precipitate-pinned dislocation contribution to the nonlinearity parameter, the measured β should scale by $(r_{IAR}/r_I)^3$ when comparing a purely irradiated sample to an irradiated – annealed – re-irradiated sample to the same total fluence. Here, r_{IAR} is the radius of precipitates in the IAR condition, and r_I is the radius of precipitates in the irradiated condition.

Note that the samples at the lower neutron fluence levels for JRQ at $T_i = 290°C$ were given an annealing treatment when 50% of the target fluence was reached. This annealing was shown to recover a significant portion of the change in the ductile-brittle transition temperature due to irradiation [86, 88]. So it is possible that a more representative measure of neutron fluence in terms of microstructural features is only the amount of neutron fluence received during the re-irradiation. In other words, 0.25×10^{19} n/cm^2 (instead of 0.5×10^{19} n/cm^2) might be a more representative fluence for sample IAR,0.5, and 0.85×10^{19} n/cm^2 (instead of 1.7×10^{19} n/cm^2) might be a more representative fluence for sample IAR,1.7.

However, re-irradiation following post-irradiation annealing has been shown in some cases to follow a different path for microstructural evolution compared to changes due to the initial irradiation [97]. For example, Kuramoto and co-authors [97] investigated re-irradiation effects in VVER-440 type weld material, and concluded from APT and PAS studies that matrix defects are the primary hardening mechanism in the re-irradiated state. So, it is possible that matrix defects contribute to β in IAR samples measured in the current study. It has been shown that defects such as vacancies can act in the same way as precipitates in terms of pinning points to dislocations [15]. It is also possible that these matrix defects respond as a different mechanism for contributing to the nonlinearity parameter. Further studies are needed to fully realize the effects on β from microstructural evolution during re-irradiation.

8.8 Implications of Surrogate Material on Irradiation Detection

The purpose of the 17-4PH thermally aged material investigation in Chapter 6 was to isolate the precipitate contribution to β in radiation damage. Both materials produce copper precipitates during thermal aging, and copper precipitates are known to be strongly linked to the radiation-induced embrittlement in RPV steels. Note that thermally-induced copper precipitation has previously been studied with nonlinear ultrasound in ASTM A710 steel to gain insight into radiation effects on nonlinearity [14]. In the 17-4PH material, Rayleigh waves could detect a decrease in β with increasing heat treatment time, while longitudinal waves were unable to detect any change in β due to heat treatment. As discussed in Section 6.3.1, this implies that the propagation distance was insufficient for the generated second harmonic wave due to the material nonlinearity to dominate the diffracting second harmonic wave excited due to instrumentation nonlinearity. Note that the irradiated JRQ and JFL samples studied in this work were the same geometry as the thermally aged 17-4PH samples for longitudinal wave measurements, so the wave propagation distance was the same. Further, the same experimental set-up (transducers, amplifier, etc.) was used for both the irradiated and thermally aged sample sets. Results from irradiation showed a clear increase (followed by a decrease in JRQ and JFL $T_i = 255°\text{C}$) due to irradiation. So, there is clearly a larger change in nonlinearity due to irradiation than thermally aged 17-4PH material.

A few aspects of the 17-4PH material make it difficult to compare to the irradiated microstructure of low-alloy steel. The precipitates in the 17-4PH heat treated samples are much smaller than in the radiation-damaged microstructure of low-alloy steels. APT results showed that the Cu precipitates, which might more accurately referred to as clusters, were in early stages of nucleation, with a diameter of less than 1 nm, so a radius of less than 0.5 nm. This is half (or less than half) the size of the precipitates

measured in irradiated low-alloy steel - about 1nm in both the JRQ and JFL samples irradiated at $T_i = 255°C$ studied in this work.

Further, the dislocation density of the martensitic 17-4PH has been reported to be around 4×10^{15} m^{-2}, even after thermal aging at temperatures lower than 500°C [146]. The dislocation density in the low alloy JRQ and JFL studied in this work are likely at least an order of magnitude lower than in the 17-4PH. For example, the dislocation density section of JRQ was investigated by neutron powder diffraction in Section 7.5, but it was found that the dislocation density was at or below the resolution limit of the instrument, which was around 1×10^{14} m^{-2}. This seems to be a good estimate, since previously reported TEM measurements of dislocation density in an as-received sample of JRQ was measured to be 1.7×10^{14} m^{-2} [60]. This difference in dislocation density implies that the critical number of precipitates needed to pin all dislocations would be significantly higher., i.e. N_{cr} in the model shown in Figure 38.

The main implications of the surrogate sample study is that measured changes in β in the irradiated material are not necessarily dominated by the precipitate-pinned dislocations, due to no detectable change in β with the same experimental set-up (longitudinal waves) in the thermally aged 17-4PH material. The differences in dislocation density and precipitate size between thermally aged 17-4PH and irradiated JRQ and JFL make it difficult to draw a definite conclusion on the relative strength of precipitate-pinned dislocations on β in the irradiated material. Note that a comparison of number density of precipitates in thermally aged 17-4PH and the irradiated JRQ and JFL cannot be made at this time, though further APT measurements or SANS studies on the 17-4PH samples could address this. It is possible that with longer heat treatment time or a higher heat treatment temperature, precipitates of similar size to the irradiated JRQ and JFL materials could be induced in the 17-4PH samples. However, utilizing another surrogate material with similar dislocation

density and that produces copper precipitates more representative of the radiation-induced copper-rich precipitates, such as an Fe-Cu alloy with at least 0.8 wt.% Cu, would allow more definite conclusions to be drawn.

8.9 Implications on Monitoring Radiation-Induced Embrittlement

Ultimately, developing a method to determine and monitor the embrittlement of the RPV in terms of the ductile-brittle transition temperature is of primary interest [84]. Physically-motivated empirical models based on a large database of RPV surveillance specimens have been developed to predict the macroscopic fracture resistance property of DBTT based on neutron fluence, flux, original material state and composition [84]. However, the nonlinear ultrasonic parameter β is sensitive to microstructural parameters such as size and volume fraction of defects. Experiments and modelling have shown that the increase in yield stress is related to the change in transition temperature shifts, as shown in Equation 36, and models for relating yield stress increases to defect parameters have been developed and were presented in Equations 37, 38, and 39.

The total change in yield stress is a function of obstacle-hardening parameters:

$$\Delta\sigma_y = \Delta\sigma_y \left(r_i, N_i, G_i, r_j, N_j, \gamma_j\right) \tag{126}$$

where r_i, N_i, and G_i are, respectively, the radius, number density, and shear stress of microstructural features that contribute to strengthening by the Russell-Brown model (Equation 38 [93]), and r_j, N_j, and γ_j are, respectively, the radius, number density, and barrier strength of microstructural features that contribute to strengthening by the Martin model (Equation 39 [94]).

The acoustic nonlinearity parameter could thus be potentially used as a tool to indirectly monitor the yield strength and transition temperature shift of irradiated steel. While it is difficult to assess given the current limited data sets presented in

this thesis, it is likely that such a predictive model will be most effective if only *one or two microstructural features dominate the embrittlement* - i.e. one term dominates in the total change in yield stress in Equation 37. For example, in JRQ, copper-rich precipitates likely dominate the radiation-induced embrittlement. Assuming a constant radius of copper-rich precipitates with increasing fluence, which was shown in SANS measurements of the lower T_i JRQ samples used in this work [52], constant dislocation density and composition of precipitates (such that the misfit parameter and stiffness of the precipitate remains constant), the change in β due to precipitate-pinned dislocations over increasing neutron fluence can be written as:

$$\Delta\beta \approx C_\beta \frac{\exp\left(-B/N\right)}{N^{1/3}} \tag{127}$$

where C_β contains the constant parameters that are (crudely) assumed to remain unchanged during irradiation:

$$C_\beta \approx 307 \frac{\Omega R^3 C_{11}^2}{G^2 b^2} \left[\frac{3B_p}{3B_p + 4G}\right] |\delta| \overline{r_p}^3 \Lambda \tag{128}$$

The change in yield stress can be written as:

$$\Delta\sigma_y \approx C_\sigma N^{1/2} \tag{129}$$

where C_σ contains the constant parameters that are (crudely) assumed to remain unchanged during irradiation:

$$C_\sigma = \frac{RGb}{1.77} \left(4/3\pi r_p\right)^{1/2} \left[1 - \left(\frac{G_p \log(r_p/r_{ic})}{G \log(r_{oc}/r_{ic})} + \frac{\log(r_{oc}/r_p)}{\log(r_{oc}/r_{ic})}\right)^2\right]^{3/4} \tag{130}$$

The change in acoustic nonlinearity can then be written in terms of the change in yield stress:

$$\Delta\beta \approx C_\beta \exp\left[-B\left(C_\sigma/\Delta\sigma_y\right)^{1/2}\right] \left(\frac{C_\sigma}{\Delta\sigma_y}\right)^{1/6} \tag{131}$$

This relation can be used with experimental results of measured β and measured $\Delta\sigma_y$ to estimate values of B, the so-called precipitate configurational entropy, during

radiation damage. Note that parameters embedded in C_β such as dislocation density and precipitate modulus (depending on composition) are not well characterized, and a predictive model would likely require fitting of this parameter in the function in Equation 131. If there are enough data points of measured β over increasing neutron fluence for the same material, flux, and irradiation temperature, this data could be used to determine with, for example, a least-squares fitting procedure, values for B and C_β for the material. The two JRQ sample sets investigated here only had two or three sample conditions, and in the JRQ $T_i = 290°\text{C}$ sample set, two irradiated samples had received an annealing treatment when 50% of the target neutron fluence was reached. The effect of annealing and subsequent re-irradiation on the microstructural features, and thus changes in yield stress, are still not fully quantitatively understood. Clearly, these sample sets are no where near sufficient to determine a predictive model for increase in yield stress during irradiation using measurements of β. However, with a more comprehensive and well-characterized sample set, this data could be used with this predictive model to determine B and C_β. In this way, β could be used to measure changes in yield strength of irradiated material.

CHAPTER IX

CONCLUSIONS AND FUTURE OUTLOOK

9.1 Summary of Results

In this thesis, the nonlinear ultrasonic method of second harmonic generation is used to monitor microstructural changes over different conditions of radiation damage in reactor pressure vessel steels. Analytical models are derived that describe changes to the magnitude of β from different microstructural features that are caused by neutron radiation in steel, specifically the interaction of interstitials segregated to and trapping dislocations, as well as an expansion on previously-derived dislocation pinning models. A thermally aged surrogate sample set is used to experimentally isolate the precipitate-pinned dislocation contribution to β. Results are interpreted based on analytical models of nonlinear wave propagation and interaction with the radiation-induced microstructural features, and extensively on existing microstructural characterizations and models of irradiated the low-alloy RPV steel.

Experimental results of measured changes in β in irradiated low-alloy steels show that nonlinear ultrasound is sensitive to radiation damage in terms of changes in neutron fluence, flux, temperature, and material composition. Specifically, β increased over increasing neutron fluence up to a critical level, and then decreased - this trend was consistent in the two different materials studied (JRQ and JFL). In JRQ irradiated at $T_i = 255°$C, β increased by 97% from the unirradiated state to the medium fluence level (5.4×10^{19} n/cm^2), and then decreased to the high fluence level (9.8×10^{19} n/cm^2), but still with a β that was 61% higher than the unirradiated state. In JFL irradiated at $T_i = 255°$C, β increased by 65% from the unirradiated state to the medium fluence level (5.1×10^{19} n/cm^2), and then decreased to the high fluence level

(8.6×10^{19} n/cm^2), but still with a β that was 4% higher than the unirradiated state. This increasing trend of β with increasing neutron fluence of about 5×10^{19} n/cm^2 was also measured in JRQ samples irradiated at $T_i = 290$°C, although there was a larger increase in β for JRQ irradiated at the lower irradiation temperature. The higher irradiation temperature caused a delay in onset of copper precipitation, so fewer copper precipitates are present in these samples than the lower irradiation temperature. Post-irradiation annealing caused a clear decrease in β of about 25% for samples irradiated to two different total neutron fluence levels (1.7×10^{19} n/cm^2 and 5.0×10^{19} n/cm^2), due to a large decrease in number density of precipitates and coarsening of the remaining precipitates during the annealing. Analytical models comparing the vacancy-pinned dislocation contribution to β to the precipitate-pinned contribution to β was consistent with the larger increase in β for the medium-Cu material (JRQ) compared to the low-Cu material (JFL), due to the fact that vacancy features dominate the irradiated microstructure of low-Cu steels. Analytical models showed that the trend of β due to pinned dislocations qualitatively agrees with experimental results, in terms of dislocation pinning before and after a critical number density of precipitates for precipitate-pinned dislocations. The model describing interstitial trapping of dislocations showed that this contribution to β can dominate the response if a second critical number density of precipitates is reached or exceeded. Results show that even if 1% of dislocations are trapped by interstitials, there will be a significant nonlinear response at the number density of precipitates formed in the irradiated JRQ material. Experimental verification of this effect has yet to be realized, since only qualitative methods such as APT have been used to characterize interstitial segregation to dislocations. However, since radiation damage has shown to cause segregation of solutes such as phosphorous and manganese to dislocations, it is possible this effect of interstitial trapping of dislocations is present in the microstructure of the irradiated JRQ, and that the NLU measurements are sensitive to

this effect.

A surrogate sample set of thermally aged 17-4PH material showed a clear decrease in β using Rayleigh waves, with increasing aging times, which caused an increase in copper precipitation. This study was aimed at deconvolving the precipitate-pinned dislocation contribution to β in the irradiated material, and results showed a sensitivity of β to this effect. However, a concrete conclusion could not be drawn since the microstructural changes in the thermally aged 17-4PH were too different than the irradiated low-alloy steel, in terms of precipitate size and dislocation density.

9.2 Recommendations for Future Work

The current work analyzes measured changes in β due to radiation-induced microstructural changes in low-alloy steel. Two separate materials, two irradiation temperatures, slight differences in neutron flux, and a variety of neutron fluence levels are investigated. However, this study represents a small subset of parameters compared to magnitude and breadth of conditions in irradiated reactor pressure steel components. Determining further sensitivity of nonlinear ultrasound to irradiated material in terms of higher fluence, lower flux, other material compositions, would be an extremely useful next step. This could also enable the development of a model to predict the increase in σ_y using measurements of β, as suggested in Section 8.9.

Further deconvolution of the different contributions of microstructural features to β is needed in order to use this nonlinear ultrasonic method as a life prediction or monitoring tool for radiation damage and embrittlement. In this work, the copper precipitate contribution of β is effectively isolated in the 17-4PH thermally aged material, however precipitates in this case are larger than those induced by neutron irradiation. Precipitates in thermally aged Fe-Cu alloys are known to be of similar size to those produced in radiation damage, so a study on an Fe-Cu alloy with copper content of at least > 0.8 wt.% would further confirm the copper precipitate

contribution to β from radiation damage. Another advantage of using an Fe-Cu surrogate sample set is that mathematical and computational models are available that can predict copper precipitation, e.g. [93, 157, 158]. This is very important for the interpretation and clarification of the CRP contribution to β.

It is possible to isolate vacancy and point defects, as well as dislocation loops, using ion irradiation. The main challenge of ion irradiation in terms of nonlinear ultrasonic measurements is the penetration depth – light ions only penetrate up to a few 10s of microns of the material surface but do not produce much damage, and heavy ions only penetrate a depth of sub-microns to a few microns, though the damage can potentially be significant. The damage profile with depth is also not constant, so there will be a distribution of damage through the depth of the ion-irradiated material. There are potentially unwanted compositional effects as well, for example if an element is used for ion implantation that is not a constituent of the material. Further, the cross-sectional area of the ion irradiation is limited by instrumentation, and likely only a few squared centimeters. Rayleigh waves would be best suited for this application, but even in this case, the penetration depth of the ion irradiation damage is estimated to be less than 3% of the wavelength of a 5 MHz Rayleigh wave propagating through steel (recall that Rayleigh waves propagate only within a depth of one wavelength of the surface of the material). This means that in order to measure only a few percent change in β, the ion irradiation damage would have to induce changes in β of at least twice the base nonlinearity of the material. So, either higher frequency Rayleigh waves could be utilized for this type of experiment, or a very high dose would need to be applied to the material. Further, ion irradiation produces some microstructural changes in steel that are comparable to neutron radiation-induced changes, but there will likely be other effects not present in the neutron irradiated material. It is clear that much further investigation and experimental design would be necessary before ion irradiation damage could be used to deconvolve neutron irradiation effects on β.

Other longer-term effects that should be considered are those that would arise during inspection of real components. For example, there is a distribution of neutron flux (and thus neutron fluence) through the thickness of the RPV wall. Another consideration is that RPVs typically operate under pressure of 7-14 MPa. If NLU measurements are taken in-situ, this static pressure will influence the magnitude of β. Measurements should be made on irradiated steel under these loading conditions to simulate a more realistic structure. So, real components will have a combination of damage that will further complicate inspection. Investigations on the influence on β due to a combination of damage, such as irradiation and stress corrosion cracking, would be useful. Further, the RPV is around 24cm thick (compared to the 1cm thickness of the Charpy samples used for NLU measurements), and has a stainless steel cladding on one side. So, inspection of real RPV components would require significant modifications to the current NLU techniques.

Combining nonlinear ultrasonic measurements with other NDE techniques could provide a fuller description of the microstructural changes in irradiated RPV material. For example, measurements of magnetic properties such as Barkenhousen noise (BN) and hysteresis loop configuration, such as was made on Fe-Cu surrogate material [142], have been shown to be sensitive to copper precipitates. These measurements have also shown success in irradiated material, e.g. [101].

9.3 Significance and Impact

This thesis provides extensive evidence of the sensitivity of the nonlinear ultrasonic method of second harmonic generation to irradiation damage in RPV steels. Since the acoustic nonlinearity parameter, β, was shown to be sensitive to changes in neutron fluence, material composition, and irradiation temperature, it has the potential to be developed into an NDE technique for monitoring radiation-induced microstructural

changes in RPV steels over irradiation damage. Further development and improvement of the technique could ultimately result in providing inputs into life extension decisions of nuclear reactors, resulting in safe operation and cost savings from unnecessary reactor shut-downs. This work also motivates using NLU for monitoring radiation damage in other key components in the reactor, and potentially in other materials currently being developed for the next generation of nuclear reactors. The next generations of nuclear reactors, referred to as Generation III+ and Generation IV, include designs such as the high temperature gas-cooled reactors, the sodium-cooled-fast reactor, the supercritical-water-cooled reactor, and will operate more efficiently in terms of fuel usage, reduce waste produced, have a more modular design, and will have enhanced safety features (such as inherent safety features). More information can be found in [159]. These reactors will involve operation at much higher temperatures and under different environments, so they will require different and potentially new materials to withstand and operate in these environments. NLU monitoring of radiation damage in such materials could be combined with other efforts investigating ultrasonic instrumentation (specifically, ultrasonic transducers) operation under extreme conditions (e.g. [112]) to investigate the applicability of using NLU for NDE of these components.

APPENDIX A

DIFFRACTION CORRECTION

Since the on-axis diffraction of the linear and nonlinear propagating wave depends on propagation distance, sample thickness will influence the amplitude of the measured first and second harmonic waves. To investigate the influence of diffraction effects on the measured acoustic nonlinearity parameter, the diffraction models introduced in Section 5.2.3.2 are used to calculate the diffraction correction on the acoustic nonlinearity parameter, $|D_\beta|$ for wave propagation equal to the thickness of samples measured in this work. The diffraction correction, $|D_\beta|$, and the influence on the resulting normalized parameter β/β_0 are given in Table 13 for JRQ $T_i = 290°$C samples, and in Table 14 for JRQ and JFL $T_i = 255°$C samples. The value $|D_\beta|/|D_\beta|_0$, where $|D_\beta|_0$ is the diffraction correction of the baseline or unirradiated sample, represents the change in β/β_0 due to variations in sample thickness. The change in β due to this thickness variation and thus due to diffraction is less than 0.6% for all sample sets investigated in this work. Therefore, diffraction effects were considered negligible.

Table 13: Diffraction correction (linear and nonlinear diffraction) for JRQ $T_i = 290°C$ samples.

Condition	Sample #	Thickness (mm)	$\lvert D_\beta \rvert$	$\lvert D_\beta \rvert / \lvert D_\beta \rvert_0$
U	1	9.902	0.9151	1
IAR,0.5	1	10.0205	0.9202	1.0056
	2	10.0195	0.9201	1.0055
IAR,1.7	1	10.021	0.9202	1.0056
	2	10.018	0.9201	1.0054
IARA,1.7	1	10.016	0.9200	1.0054
	2	10.0185	0.9201	1.0055
I,5	1	10.0105	0.9197	1.0050
	2	10.016	0.9200	1.0054
IA,5	1	10.0008	0.9196	1.0049
	2	9.9975	0.9192	1.0045

Table 14: Diffraction correction (linear and nonlinear diffraction) for JRQ and JFL $T_i = 255°C$ samples.

Condition	Sample #	Thickness (mm)	$\lvert D_\beta \rvert$	$\lvert D_\beta \rvert / \lvert D_\beta \rvert_0$
JRQ, U	1	9.997	1.0140	1
	2	9.982	1.0143	1.0003
	3	9.992	1.0141	1.0001
JRQ, I,5.4	1	9.916	1.0158	1.0018
	2	9.959	1.0149	1.0009
	3	9.857	1.0170	1.0030
JRQ, I,9.8	1	9.865	1.0169	1.0029
	2	9.892	1.0163	1.0023
	3	9.832	1.0175	1.0035
JFL, U	1	9.957	1.0149	1.0009
	2	9.977	1.0144	1.0004
	3	9.995	1.0140	1
JFL, I,5.1	1	9.904	1.0161	1.0021
	2	9.879	1.0166	1.0026
	3	9.819	1.0178	1.0037
JFL, I,8.6	1	9.938	1.0153	1.0013
	2	9.930	1.0155	1.0015
	3	9.961	1.0148	1.0008

APPENDIX B

SOURCES OF MEASUREMENT VARIATION

Three sources of measurement variation were investigated to gain insight into the variations of the measurements shown in Figure 34: (1) surface roughness effects, (2) the measurement fixture, and (3) clamping force variation due to sample thickness variation. Characterizations of all these effects are presented in this appendix, but it was found that the variation in surface roughness caused most of the variation in results shown in Figure 34. So, surface roughness effects on β were used to adjust the error bars to account for these effects in Figure 34.

B.1 Surface Roughness Effects

Surface roughness of samples caused both an increase in β and a variation in β. To quantitatively investigate how surface roughness increased β, nonlinear ultrasonic measurements were made on unirradiated samples at decreasing levels of surface roughness. Measurements of β and the area-average surface area roughness, Sa, were measured after each polishing increment. Surface roughness measurements were made using a laser confocal microscope (Olympus LEXT 3D Material Confocal Microscope). Three-dimensional images of the sample surface-area roughness after increments in polish level are shown in Figures 41-42, showing the surface tomography profile. These images are shown for the as-is surface, and then hand polished to 150, 240, and 400 grit polish paper. These results show that β varies inversely with Sa, as shown in Figure 43a. With these results, measurements of β for samples polished to different grit levels can be compared by accounting for the increase in β caused by Sa at that polish level. In this way, results of β over fluence level were adjusted, as

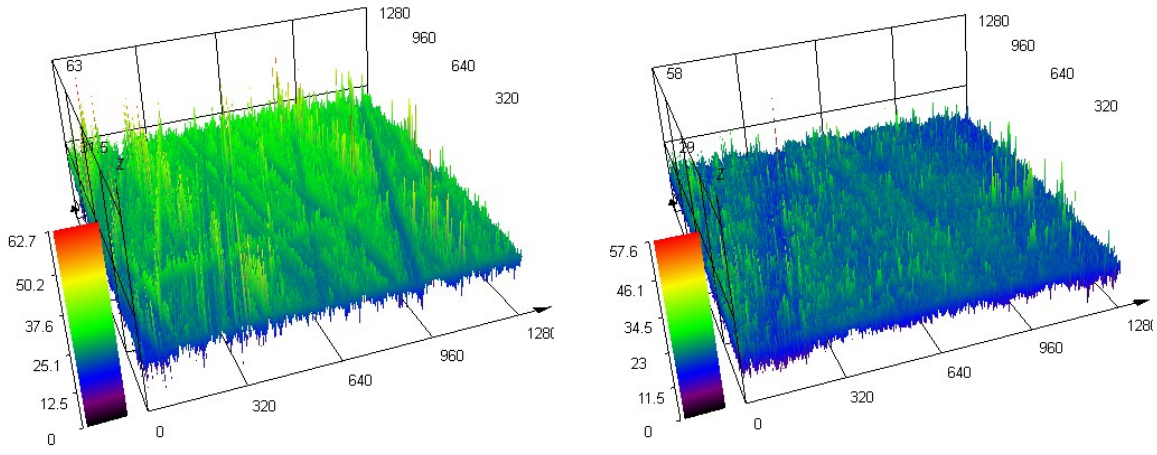

(a) (b)

Figure 41: Laser confocal microscope images of (a) the as-is Charpy sample surface, and (b) polished surface to 150 grit polish paper.

shown in Figure 34.

To quantitatively investigate effects of *variation* from sample surface roughness, β was measured on ten unirradiated steel samples that were previously machine-polished to 600 grit. Samples were then hand polished to 2000 grit with a small amount of oil lubricant, and measurements were repeated. The variation in measurements among samples dropped to 3.27% for JFL and 4.57% for JRQ. Results normalized to the average β for each material and polish level are shown in Figure 43b. Results for β over fluence were adjusted to account for this variation due to surface roughness.

B.2 Variation from Measurement Fixture

The fixture described in Section 5.2.3.2 was used to measure the acoustic nonlinearity parameter in both the irradiated and surrogate material with longitudinal waves. The fixture was transported to Helmholtz-Zentrum Dresden-Rossendorf (HZDR) laboratory in Dresden, Germany for measurements on JRQ and JFL at $T_i = 255°C$, and to Oak Ridge National Laboratory for the measurements on JRQ at $T_i = 290°C$. These

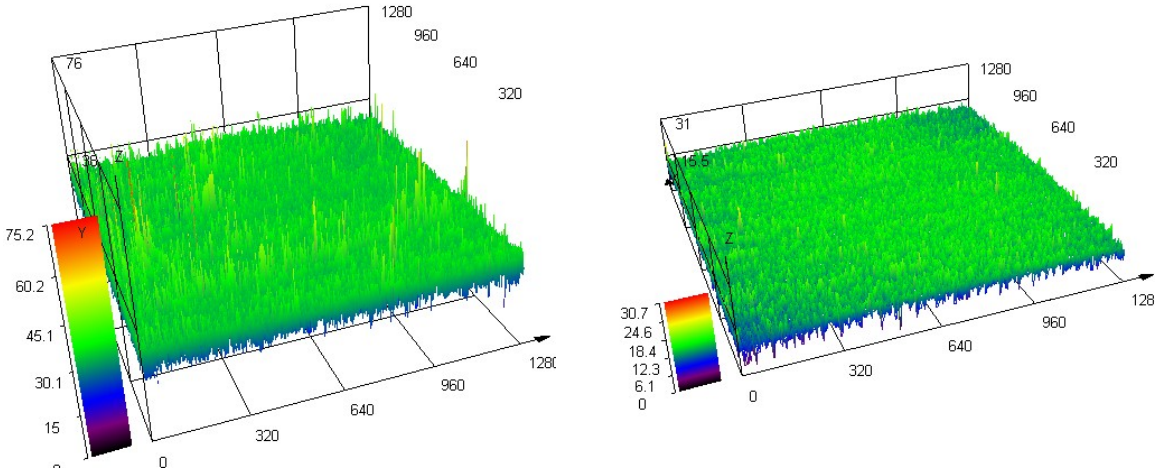

(a) (b)

Figure 42: Laser confocal microscope images of the (a) polished surface to 240 grit polish paper, and (b) polished surface to 400 grit polish paper.

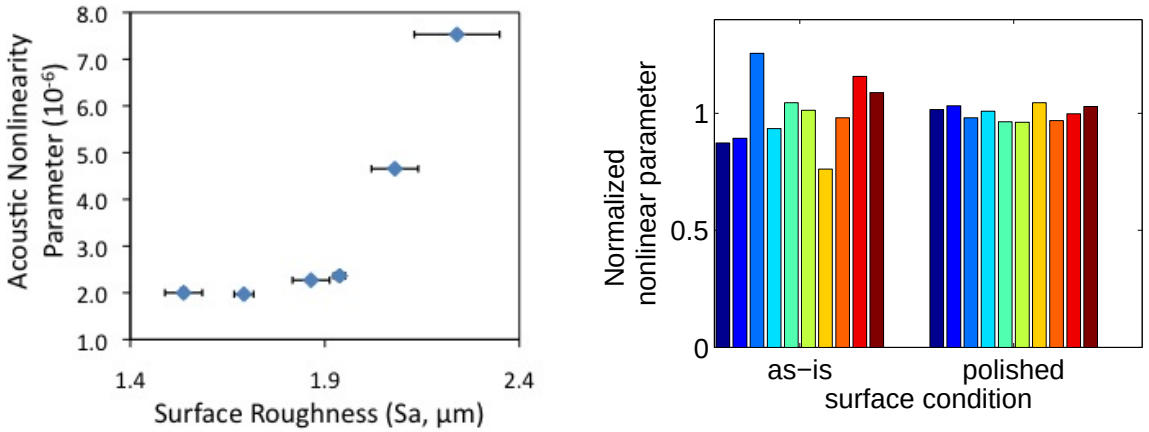

(a) (b)

Figure 43: (a) Dependence of β on surface roughness for JRQ and JFL unirradiated samples, and (b) normalized β for unirradiated samples (polished to 600 grit) and after polish to 2000 grit.

experiments were set up by staff certified to handle the radioactive samples at each laboratory. Thus, these experiments provided a good means of evaluating the performance of the fixture. It was found that there was a maximum of 5% variation between different measurements on the same sample, which is small compared to variation due to microstructural variations and surface roughness that cause up to 30% variation in these measurements. Thus, the fixture provides repeatable measurements.

B.3 Clamping Force Variations

Due to the design of the fixture, there is a greater clamping force on thicker samples and less clamping force on thinner samples. This can easily be adjusted by the operator to obtain exactly the same clamping force for different measurements, but for sensitive samples such as irradiated samples, small adjustments for slight thickness variations can be time-consuming. To isolate and quantitatively evaluate effects of thickness variation among samples on β measurements, measurements were made on one sample while the length of one toggle clamp in the fixture was incremented (to simulate samples of different thicknesses). Measurements of β over changes in toggle clamp length are shown in Figure 5 (right), and are referenced to the length of the toggle clamp used in actual measurements. The upper and lower bounds for the toggle clamp length were selected as the points just before the toggle clamps could not fully close since the force was too great and just after the toggle clamps did not reach the transducers to clamp them to the sample. Generally, acoustic nonlinearity varies inversely with increasing clamping pressure and levels off to a constant value, and this trend is generally consistent with previous experimental studies on how contact pressure influences the acoustic nonlinearity parameter [160]. Variations in β are within 5% for toggle clamp length (and thus sample thickness) variation of 0.8mm. To accommodate samples with more variation in thickness, toggle clamp length can be manipulated to provide the same clamping force. However, samples in this study

varied up to only 0.13mm in thickness, so variations in clamping force had only a small effect (up to 5% variation) in measured acoustic nonlinearity.

APPENDIX C

LINEAR ULTRASONIC MEASUREMENTS

Measurements of longitudinal wave velocity and the attenuation coefficient were made on the JRQ and JFL samples irradiated at $T_i = 255°C$ to compare the sensitivity of the acoustic nonlinearity parameter to irradiation damage to linear methods of ultrasonic inspection. Wave velocity changes are linked to changes in second-order elastic constants or density of the material, since the longitudinal wave velocity is defined as:

$$c_L = \sqrt{\frac{\lambda + 2\mu}{\rho}} \quad . \tag{132}$$

The attenuation coefficient can be related to the material microstructure in terms of grain structure, dislocations, and inhomogeneities [161].

C.1 Measurement Procedure

These measurements used broadband 10 MHz transducers aligned on either side of the Charpy sample, in the same configuration as shown in Figure 14a. Transducer 1 measured the reflection coefficient of the coupling at the interface of transducer 2, and transducer 2 measured the attenuation coefficient using a broadband pulse. These measurements were made using a technique that corrected for the irreproducible coupling conditions between the transducer and sample surface [161]. A fixture similar to the fixture used in the NLU experiments was designed so the coupling conditions on one transducer were not affected by removing or remounting the other transducer. This enabled a measurement of the reflection coefficient at the transducer-sample interface. If $S(f)_{free}$ is the spectra of the signal measured with transducer 1 without

transducer 2 mounted, and $S(f)$ is the spectra of the signal measurement with transducer 1 with transducer 2 mounted, the reflection coefficient, R, for the coupling at transducer 2 is [161]:

$$R = \frac{S(f)}{S(f)_{free}} \quad . \tag{133}$$

When transducer 2 is not mounted, the surface of the sample is a free surface and therefore the reflection coefficient at that surface is known to be 1. The attenuation measurement with transducer 2 can then be corrected for the coupling conditions between the transducer and sample. The final expression for the attenuation coefficient, α, is

$$\alpha(f) = \frac{1}{2z}\left[\ln\left(\frac{S_{1,2}(f)}{S_{2,2}(f)}\right) - \ln\left(\frac{D(f,2z)}{D(f,4z)}\right) + \ln\left(|R|\right)\right] \tag{134}$$

where z is the thickness of the sample, $S_{1,2}$ is the spectra of the first reflection of the signal measured by transducer 2 in double-echo setup, $S_{2,2}$ is the spectra of the second reflection of the signal measured by transducer 2 in double-echo setup, $D(f,2z)$ is the diffraction correction for the signal for the first reflection (when the wave has propagated two thicknesses in distance), $D(f,4z)$ is the diffraction correction for the signal for the second reflection when the wave has propagated four thicknesses in distance. The details of this derivation is given in [161]. Velocity measurements are made in conjunction with the attenuation measurements the same signals are used. The time-of-flight between successive peaks of reflections is used to calculate the wave velocity of the longitudinal wave. An example time signal of the two successive reflections used for the longitudinal wave velocity measurements is shown in Figure 44.

C.2 Results

The measured attenuation coefficients are shown in Figure 46, and the wave velocity is shown in Figure 45. These plots show measurements on both JFL and JRQ materials in the unirradiated state, and the medium and high fluence levels. For the attenuation

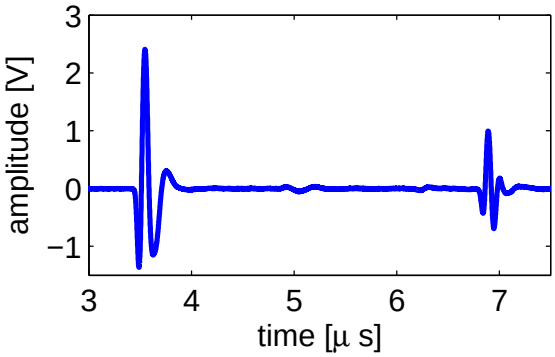

Figure 44: Example time signal of the two successive reflections used for the longitudinal wave velocity measurements.

measurements, the data for the unirradiated state was averaged over 2 samples, and data for the irradiated samples were averaged over 3 samples (except sample set jrq98 - the reflection coefficient measurement for the third sample was too low for most frequencies). The JFL samples show only a small decrease in attenuation above 12 MHz for the irradiated samples compared to unirradiated. The JRQ samples show a clear decrease over the entire frequency range interrogated from unirradiated to medium fluence, and then a slight increase from medium to high fluence. In the velocity measurement results, the data point for the unirradiated samples is averaged over two samples, and the data points for the irradiated samples are averaged over three samples. The results show small changes in velocity over fluence e.g. 1.04% from unirradiated to 5.1×10^{19} n/cm^2 (for the JFL samples), and the error is large compared to these changes.

These results show that the velocity measurements are not sensitive to radiation damage this was expected since neither the second-order elastic constants nor the density are expected to change due to radiation damage. Measurements of attenuation show that the attenuation parameter is somewhat sensitive to radiation damage in JRQ but not JFL, except at very high frequencies. There are crucial drawbacks to attenuation measurements. One drawback is how cumbersome the measurements are to make. To characterize the coupling and thus measure the reflection coefficient,

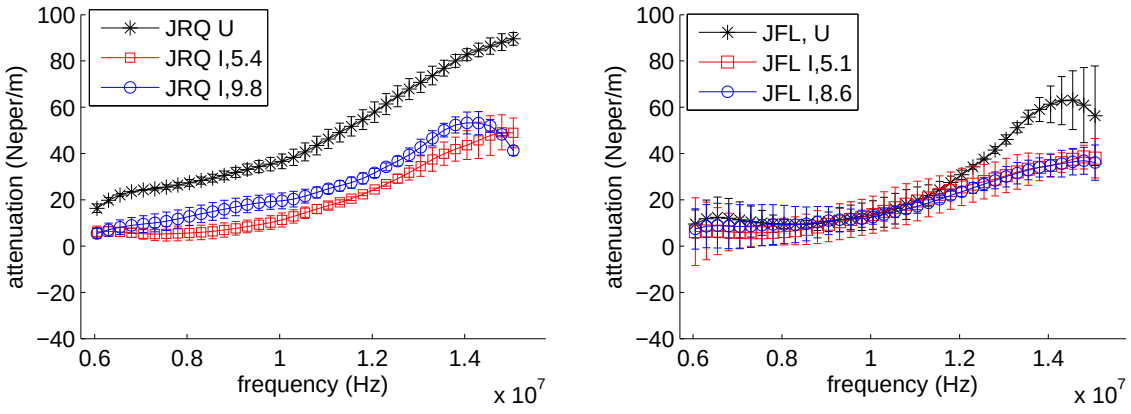

(a) (b)

Figure 45: Measurements of attenuation coefficient over frequency range for (a) JRQ, and (b) JFL, for unirradiated and irradiated samples.

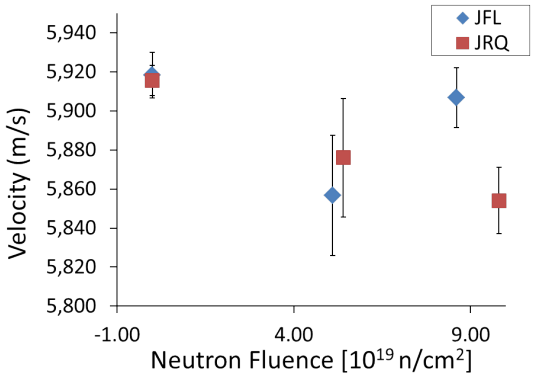

Figure 46: Longitudinal wave velocity measured in JRQ and JFL unirradiated and irradiated samples.

one transducer needs to be mounted and removed without disturbing the coupling conditions of the other this is practically very difficult. When making these measurements in the lab with technicians handling the transducer setup, measurements had to be repeated many times because the coupling condition on the fixed transducer was disturbed (this could be seen by a decrease in signal strength when the other transducer was removed). The other drawback is that the attenuation coefficient is also influenced by grain sizes and scattering from other sources than microstructural features. This appendix shows that nonlinear ultrasound has greater sensitivity to radiation damage than linear ultrasonic inspection methods. Furthermore, nonlinear ultrasonic experiments were more feasible to make by a non-expert technician and on radioactive samples.

REFERENCES

[1] Breazeale, M. A. and Thompson, D. O., "Finite-amplitude ultrasonic waves in aluminum," *Applied Physics Letters*, Vol. 3, No. 5, 1963, pp. 77–78.

[2] Breazeale, M. A. and Ford, J., "Ultrasonic studies of the nonlinear behavior of solids," *Journal of Applied Physics*, Vol. 36, No. 11, 1965, pp. 3486–3490.

[3] Hikata, A., Chick, B. B., and Elbaum, C., "Dislocation contribution to the second harmonic generation of ultrasonic waves," *Journal of Applied Physics*, Vol. 36, No. 1, 1965, pp. 229–236.

[4] Hikata, A., Sewell, F. A., and Elbaum, C., "Generation of Ultrasonic Second and Third Harmonics due to Dislocations. II," *Physical Review*, Vol. 151, No. 2, 1966, pp. 442–449.

[5] Cantrell, J. H., "Crystalline structure and symmetry dependence of acoustic nonlinearity parameters," *Journal of Applied Physics*, Vol. 76, 1994, pp. 3372.

[6] Nazarov, V. E. and Sutin, A. M., "Nonlinear elastic constants of solids with cracks," *Journal of the Acoustical Society of America*, Vol. 102, 1997, pp. 3349–3354.

[7] Cantrell, J. H. and Yost, W. T., "Determination of precipitate nucleation and growth rates from ultrasonic harmonic generation," *Applied Physics Letters*, Vol. 77, No. 13, 2000, pp. 1952–1954.

[8] Cantrell, J. H. and Yost, W. T., "Nonlinear ultrasonic characterization of fatigue microstructures," *International Journal of Fatigue*, Vol. 23, 2001, pp. S487–S490.

[9] Norris, A. N., "Finite-Amplitude Waves in Solids," *Nonlinear Acoustics*, edited by M. F. Hamilton and D. T. Blackstock, Academic Press, 1998, pp. 263–277.

[10] Shui, Y. and Solodov, I. Y., "Nonlinear properties of Rayleigh and Stoneley waves in solids," *Journal of Applied Physics*, Vol. 64, No. 11, 1988, pp. 6155–6165.

[11] de Lima, W. J. N. and Hamilton, M. F., "Finite-amplitude waves in isotropic elastic plates," *Journal of Sound and Vibration*, Vol. 265, No. 4, 2003, pp. 819–839.

[12] Cantrell, J. H., "Fundamentals and Applications of Nonlinear Ultrasonic Nondestructive Evaluation," *Ultrasonic Nondestructive Evaluation*, edited by T. Kundu, CRC Press LLC, 2004.

[13] Cantrell, J. H. and Zhang, X.-G., "Nonlinear acoustic response from precipitate-matrix misfit in a dislocation network," *Journal of Applied Physics*, Vol. 84, No. 10, 1998, pp. 5469–5472.

[14] Hurley, D. C., Balzar, D., and Purtscher, P. T., "Nonlinear ultrasonic assessment of precipitation hardening in ASTM A710 steel," *Journal of Materials Research*, Vol. 15, No. 9, 2000, pp. 2036–2042.

[15] Cantrell, J. H., "Quantitative assessment of fatigue damage accumulation in wavy slip metals from acoustic harmonic generation," *Philosophical Magazine*, Vol. 86, No. 11, April 2006, pp. 1539–1554.

[16] Thiele, S., *Air-coupled detection of Rayleigh surface waves to asses material nonlinearity due to precipitation in alloy steel*, Master's thesis, Georgia Institute of Technology, 2013.

[17] Eringen, A. C., *Mechanics of Continua*, Robert E. Krieger Publishing Company, Huntington, NY, 1980.

[18] Martin, J. W., *Precipitation Hardening*, Permagon Press, Oxford, 1968.

[19] Cantrell, J. H., "Substructural organization, dislocation plasticity and harmonic generation in cyclically stressed wavy slip metals," *Proceedings of the Royal Society of London, Series A (Mathematical, Physical and Engineering Sciences)*, Vol. 460, No. 2043, 2004, pp. 757–780.

[20] Hull, D. and Bacon, D. J., *Introduction to Dislocations*, Butterworth Heinemann, Oxford, 4th ed., 2001.

[21] Barnard, D. J., Dace, G. E., and Buck, O., "Acoustic harmonic generation due to thermal embrittlement of Inconel 718," *Journal of Nondestructive Evaluation*, Vol. 16, No. 2, 1997, pp. 67–75.

[22] Blackshire, J. L., Sathish, S., Na, J. K., and Frouin, J., "Nonlinear laser ultrasonic measurements of localized fatigue damage," *Review of Progress in Quantitative Nondestructive Evaluation*, edited by D. O. Thompson and D. E. Chimenti, Vol. 22, AIP, New York, 2003, pp. 1479–1488.

[23] Deng, M. and Pei, J., "Assessment of accumulated fatigue damage in solid plates using nonlinear Lamb wave approach," *Applied Physics Letters*, Vol. 90, No. 12, 2007, pp. 121902–121903.

[24] Frouin, J., Sathish, S., Matikas, T. E., and Na, J. K., "Ultrasonic linear and nonlinear behavior of fatigued Ti-6Al-4V," *Journal of Materials Research*, Vol. 14, No. 4, 1998, pp. 1295–1298.

[25] Kim, J.-Y., Jacobs, L. J., Qu, J., and Littles, J. W., "Experimental characterization of fatigue damage in a nickel-base superalloy using nonlinear ultrasonic waves," *Journal of the Acoustical Society of America*, Vol. 120, No. 3, 2006, pp. 1266–1273.

[26] Herrmann, J., Kim, J.-Y., Jacobs, L. J., Qu, J., Littles, J. W., and Savage, M. F., "Assessment of material damage in a nickel-base superalloy using nonlinear Rayleigh surface waves," *Journal of Applied Physics*, Vol. 99, 2006, pp. 124913.

[27] Pruell, C., Kim, J.-Y., Qu, J., and Jacobs, L. J., "Evaluation of fatigue damage using nonlinear guided waves," *Smart Materials and Structures*, Vol. 18, No. 3, 2009, pp. 035003 (7 pp.).

[28] Walker, S. V., Kim, J.-Y., Qu, J., and Jacobs, L. J., "Fatigue damage evaluation in A36 steel using nonlinear Rayleigh surface waves," *NDT & E International*, Vol. 48, June 2012, pp. 10–15.

[29] Viswanath, A., Rao, B. P. C., Mahadevan, S., Parameswaran, P., Jayakumar, T., and Raj, B., "Nondestructive assessment of tensile properties of cold worked AISI type 304 stainless steel using nonlinear ultrasonic technique," *Journal of Materials Processing Technology*, Vol. 211, No. 3, March 2011, pp. 538–544.

[30] Liu, M., Kim, J.-Y., Jacobs, L. J., and Qu, J., "Experimental study of nonlinear Rayleigh wave propagation in shot-peened aluminum plates - Feasibility of measuring residual stress," *NDT&E International*, Vol. 44, 2011, pp. 67–74.

[31] Hurley, D. C., Balzar, D., Purtscher, P. T., and Hollman, K. W., "Nonlinear ultrasonic parameter in quenched martensitic steels," *Journal of Applied Physics*, Vol. 83, No. 9, 1998, pp. 4584–4588.

[32] Yost, W. T. and Cantrell, J. H., "The effects of fatigue on acoustic nonlinearity in aluminum alloys," *IEEE Ultrasonics Symposium*, 1992, pp. 947–955.

[33] Cantrell, J. H. and Yost, W. T., "Effect of precipitate coherency strains on acoustic harmonic generation," *Journal of Applied Physics*, Vol. 81, No. 7, 1997, pp. 2957–2962.

[34] Baby, S., Kowmudi, B. N., Omprakash, C. M., Satyanarayana, D. V. V., Balasubramaniam, K., and Kumar, V., "Creep damage assessment in titanium alloy using a nonlinear ultrasonic technique," *Scripta Materialia*, Vol. 59, 2008, pp. 818–821.

[35] Xiang, Y., Deng, M., Xuan, F.-Z., and Liu, C.-J., "Cumulative second-harmonic analysis of ultrasonic Lamb waves for ageing behavior study of modified-HP austenite steel," *Ultrasonics*, Vol. 51, No. 8, Dec. 2011, pp. 974–981.

[36] Kim, C. S., Park, I.-K., and Jhang, K.-Y., "Nonlinear ultrasonic characterization of thermal degradation in ferritic 2.25Cr-1Mo steel," *NDT&E International*, Vol. 42, April 2009, pp. 204–209.

[37] Viswanath, A., Rao, B. P. C., Mahadevan, S., Jayakumar, T., and Baldev, R., "Microstructural characterization of M250 grade maraging steel using nonlinear ultrasonic technique," *Journal of Materials Science*, Vol. 45, No. 24, 2010, pp. 6719–6726.

[38] Ruiz, A., Ortiz, N., Medina, A., Kim, J.-Y., and Jacobs, L., "Application of ultrasonic methods for early detection of thermal damage in 2205 duplex stainless steel," *NDT & E International*, Vol. 54, March 2013, pp. 19–26.

[39] U. S. Nuclear Regulatory Committee, "Student's Corner - Nuclear Reactors," http://www.nrc.gov/reading-rm/basic-ref/students/animated-pwr.html, Date Accessed: November 8, 2012, 2012.

[40] Odette, G. and Lucas, G. E., "An Integrated Approach to Evaluating the Fracture Toughness of Irradiated Nuclear Reactor Pressure Vessels," *Journal of Nondestructive Evaluation*, Vol. 15, No. 3/4, 1996, pp. 137–150.

[41] Odette, G., Lucas, G. E., and Klingensmith, D., "On the Effect of Neutron Flux and Composition on Hardening of Reactor Pressure Vessel Steels and Model Alloys," *Materials Research Society Symposium Proceedings*, Vol. 650, 2001, pp. R6.4.1–R6.4.6.

[42] "Life Beyond 60 Workshop Summary Report," Tech. rep., NRC/DOE, 2008.

[43] Smith, C., Nanstad, R. K., Clayto, D., Matlack, K., Ramuhalli, P., and Light, G., "Roadmap for Nondestructive Evaluation of Reactor Pressure Vessel Research and Development by the Light Water Reactor Sustainability Program," Tech. Rep. ORNL/TM-2012/380, Oak Ridge National Laboratory, Oak Ridge, Tennessee, 2012.

[44] Stoller, R. E., Odette, G., and Wirth, B. D., "Primary damage formation in bcc iron," *Journal of Nuclear Materials*, Vol. 251, 1997, pp. 49–60.

[45] Was, G. S., *Fundamentals of Radiation Materials Science*, Springer, 2007.

[46] Eason, E., Odette, G., Nanstad, R. K., and Yamamoto, T., "A Physically Based Correlation of Irradiation-Induced Transition Temperature Shifts for RPV Steels," Tech. Rep. ORNL/TM-2006/530, U.S. Nuclear Regulatory Commission, 2006.

[47] Odette, G. and Lucas, G. E., "Recent progress in understanding reactor pressure vessel steel embrittlement," *Radiation Effects and Defects in Solids*, Vol. 144, 1998, pp. 189–231.

[48] Odette, G., Yamamoto, T., and Klingensmith, D., "On the effect of dose rate on irradiation hardening of RPV steels," *Philosophical Magazine*, Vol. 85, No. 4-7, Jan. 2005, pp. 779–797.

[49] Williams, T. J. and Ellis, D., "A Mechanistically-Based Model of Irradiation Damage in Low Alloy Steel Submerged Arc Welds," *Effects of Radiation on Materials: 20th International Symposium, ASTM STP 1405*, edited by S. T. Rosinski, M. L. Grossbeck, T. R. Allen, and A. S. Kumar, Vol. 2, American Society for Testing Materials, West Conshohocken, PA, 2001, p. 8.

[50] Odette, G., "On the dominant mechanism of irradiation embrittlement of reactor pressure vessel steels," *Scripta Metallurgica*, Vol. 17, No. 10, Oct. 1983, pp. 1183–1188.

[51] Odette, G. and Wirth, B. D., "A computational microscopy study of nanostructural evolution in irradiated pressure vessel steels," *Journal of Nuclear Materials*, Vol. 251, Nov. 1997, pp. 157–171.

[52] Ulbricht, A., Bohmert, J., and Viehrig, H.-W., "Microstructural and Mechanical Characterization of Radiation Effects in Model Reactor Pressure Vessel Steels," *Journal of ASTM International*, Vol. 2, No. 10, 2005, pp. 1–14.

[53] Gurovich, B. A., Kuleshova, E. A., Nikolaev, Y. A., and Shtrombakh, Y. I., "Assessment of relative contributions from different mechanisms to radiation embrittlement of reactor pressure vessel steels," *Journal of Nuclear Materials*, Vol. 246, 1997, pp. 91–120.

[54] Meslin, E., Lambrecht, M., Hernández-Mayoral, M., Bergner, F., Malerba, L., Pareige, P., Radiguet, B., Barbu, A., Gómez-Briceño, D., Ulbricht, A., and Almazouzi, a., "Characterization of neutron-irradiated ferritic model alloys and a RPV steel from combined APT, SANS, TEM and PAS analyses," *Journal of Nuclear Materials*, Vol. 406, No. 1, Nov. 2010, pp. 73–83.

[55] Brauer, G. and Eichhorn, F., "Considerations about irradiation-induced precipitates in Soviet type reactor pressure vessel steels," *Nuclear Engineering and Design*, Vol. 143, Sept. 1993, pp. 301–307.

[56] Odette, G., Lucas, G. E., Klingensmith, D., Wirth, B. D., and Gragg, D., "The Effects of Composition and Heat Treatment on Hardening and Embrittlement of Reactor Pressure Vessel Steels," Tech. Rep. NUREG/CR-6778, U.S. Nuclear Regulatory Commission, 2003.

[57] Miller, M., Chernobaeva, A. A., Shtrombakh, Y. I., Russell, K., Nanstad, R. K., Erak, D. Y., and Zabusov, O., "Evolution of the nanostructure of VVER-1000 RPV materials under neutron irradiation and post irradiation annealing," *Journal of Nuclear Materials*, Vol. 385, 2009, pp. 615–622.

[58] Cumblidge, S. E., Motta, A. T., Catchen, G. L., Brauer, G., and Böhmert, J., "Evidence for neutron irradiation-induced metallic precipitates in model alloys and pressure-vessel weld steel," *Journal of Nuclear Materials*, Vol. 320, No. 3, 2003, pp. 245–257.

[59] Miller, M., Pareige, P., and Burke, M. G., "Understanding Pressure Vessel Steels: An Atom Probe Perspective," *Materials Characterization*, Vol. 44, 2000, pp. 235–254.

[60] Kocik, J., Keilova, E., Cizek, J., and Prochazka, I., "TEM and PAS study of neutron irradiated VVER-type RPV steels," *Journal of Nuclear Materials*, Vol. 303, 2002, pp. 52–64.

[61] Brauer, G., Liszkay, L., Molnar, B., and Krause, R., "Microstructural aspects of neutron embrittlement of reactor pressure vessel steels - A view from positron annihilation spectroscopy," *Nuclear Engineering and Design*, Vol. 127, May 1991, pp. 47–68.

[62] Wolfer, W. G. and Glasgow, B. B., "Dislocation evolution in metals during irradiation," *Acta Metallica*, Vol. 33, No. 11, 1985, pp. 1997–2004.

[63] Soneda, N., Dohi, K., Nishida, K., Nomoto, A., Tomimatsu, M., and Matsuzawa, H., "Microstructural Characterization of RPV Materials Irradiated to High Fluences at High Flux," *Journal of ASTM International*, Vol. 6, No. 7, 2009, pp. 1–16.

[64] Odette, G. and Nanstad, R. K., "Predictive reactor pressure vessel steel irradiation embrittlement models: Issues and opportunities," *JOM*, Vol. 61, No. 7, July 2009, pp. 17–23.

[65] Stoller, R. E., "The Effect of Neutron Flux on Radiation-Induced Embrittlement in Reactor Pressure Vessel Steels," *Effects of Radiation on Materials: 21st International Symposium, ASTM STP 1447*, edited by M. L. Grossbeck, T. R. Allen, R. G. Lott, and A. S. Kumar, ASTM International, West Conshohocken, PA, 2004.

[66] Buswell, J., Phythian, W. J., Mcelroy, R. J., Dumbill, S., Ray, P. H. N., Mace, J., and Sinclair, R. N., "Irradiation-induced microstructural changes , and hardening mechanisms, in model PWR reactor pressure vessel steels," *Journal of Nuclear Materials*, Vol. 225, 1995, pp. 196–214.

[67] Malerba, L., Caro, A., and Wallenius, J., "Multiscale modelling of radiation damage and phase transformations: The challenge of FeCr alloys," *Journal of Nuclear Materials*, Vol. 382, 2008, pp. 112–125.

[68] Miller, M., Russell, K., Sokolov, M. A., and Nanstad, R. K., "APT characterization of irradiated high nickel RPV steels," *Journal of Nuclear Materials*, Vol. 361, No. 2-3, April 2007, pp. 248–261.

[69] Bruemmer, S., Simonen, E., Scott, P., Andresen, P., Was, G., and Nelson, J., "Radiation-induced material changes and susceptibility to intergranular failure of light-water-reactor core internals," *Journal of Nuclear Materials*, Vol. 274, No. 3, Sept. 1999, pp. 299–314.

[70] Brauer, G., Puska, M. J., Sob, M., and Korhonen, T., "Positron affinity for precipitates in reactor pressure vessel steels," *Nuclear Engineering and Design*, Vol. 158, 1995, pp. 149–156.

[71] Glade, S. C., Wirth, B. D., Asoka-Kumar, P., Sterne, P. A., and Odette, G., "Positron Annihilation Spectroscopy of Nanostructural Features in Model Reactor Pressure Vessel Steels," *Materials Science Forum*, Vol. 445-446, 2004, pp. 87–89.

[72] Pokor, C., Brechet, Y., Dubuisson, P., Massoud, J.-P., and Barbu, A., "Irradiation damage in 304 and 316 stainless steels: experimental investigation and modeling. Part I: Evolution of the microstructure," *Journal of Nuclear Materials*, Vol. 326, 2004, pp. 19–29.

[73] Yoshida, N., Xu, Q., Watanabe, H., Muroga, T., and Kiritani, M., "Low dose fission neutron irradiation on Pand Ti-modified austenitic alloys with improved temperature control," *Fifth International Conference on Fusion Reactor Materials (ICFRM-5)*, 1992, pp. 1114–1118.

[74] Miller, M. and Russell, K., "Embrittlement of RPV steels: An atom probe tomography perspective," *Journal of Nuclear Materials*, Vol. 371, No. 1-3, Sept. 2007, pp. 145–160.

[75] Becquart, C., Barbu, A., Bocquet, J., Caturla, M., Domain, C., Fu, C.-C., Golubov, S., Hou, M., Malerba, L., Ortiz, C., Souidi, a., and Stoller, R. E., "Modeling the long-term evolution of the primary damage in ferritic alloys using coarse-grained methods," *Journal of Nuclear Materials*, Vol. 406, No. 1, Nov. 2010, pp. 39–54.

[76] Domain, C., Becquart, C., and Malerba, L., "Simulation of radiation damage in Fe alloys: an object kinetic Monte Carlo approach," *Journal of Nuclear Materials*, Vol. 335, No. 1, Oct. 2004, pp. 121–145.

[77] Monasterio, P., Wirth, B. D., and Odette, G., "Kinetic Monte Carlo modeling of cascade aging and damage accumulation in FeCu alloys," *Journal of Nuclear Materials*, Vol. 361, No. 2-3, April 2007, pp. 127–140.

[78] Duparc, A. H., Moingeon, C., Smetniansky-de Grande, N., and Barbu, A., "Microstructure modelling of ferritic alloys under high flux 1 MeV electron irradiations," *Journal of Nuclear Materials*, Vol. 302, No. 2-3, April 2002, pp. 143–155.

[79] Nagai, Y., Tang, Z., Hassegawa, M., Kanai, T., and Saneyasu, M., "Irradiation-induced Cu aggregations in Fe: An origin of embrittlement of reactor pressure vessel steels," *Physical Review B*, Vol. 63, No. 13, March 2001, pp. 134110.

[80] Barashev, A. V. and Arokiam, A. C., "Monte Carlo modelling of Cu atom diffusion in alpha-Fe via the vacancy mechanism," *Philosophical Magazine Letters*, Vol. 86, No. 5, May 2006, pp. 321–332.

[81] Lambrecht, M., Malerba, L., and Almazouzi, a., "Influence of different chemical elements on irradiation-induced hardening embrittlement of RPV steels," *Journal of Nuclear Materials*, Vol. 378, No. 3, Sept. 2008, pp. 282–290.

[82] Miller, M., Nanstad, R. K., Sokolov, M. A., and Russell, K., "The effects of irradiation, annealing and reirradiation on RPV steels," *Journal of Nuclear Materials*, Vol. 351, No. 1-3, June 2006, pp. 216–222.

[83] Sokolov, M. A., Spooner, S., Odette, G., and Wirth, B. D., "SANS study of high-copper RPV welds in irradiated and annealed conditions," *Effects of Radiation on Materials: 18th International Symposium, ASTM STP 1325*, edited by R. K. Nanstad, M. L. Hamilton, F. A. Garner, and A. S. Kumar, ASTM International, West Conshohocken, PA, 1999, pp. 333–345.

[84] Eason, E., Odette, G., Nanstad, R. K., and Yamamoto, T., "A Physically Based Correlation of Irradiation-Induced Transition Temperature Shifts for RPV Steels," *Journal of Nuclear Materials*, Vol. 433, No. 1-3, Feb. 2013, pp. 240–254.

[85] Was, G. S., Hash, M., and Odette, G., "Hardening and microstructure evolution in proton-irradiated model and commercial pressure-vessel steels," *Philosophical Magazine*, Vol. 85, No. 4-7, Jan. 2005, pp. 703–722.

[86] Nanstad, R. K., Niffenegger, M., Kalkhof, R. D., Miller, M., Sokolov, M. A., and Tipping, P., "Fracture Toughness, Thermo-Electric Power, and Atom Probe Investigations of JRQ Steel in I, IA, IAR, and IARA Conditions," *Journal of ASTM International*, Vol. 2, No. 9, 2005, pp. 1–17.

[87] Zurbuchen, C., Viehrig, H.-W., and Weiss, F.-P., "Master Curve and Unified Curve applicability to highly neutron irradiated Western type reactor pressure vessel steels," *Nuclear Engineering and Design*, Vol. 239, 2009, pp. 1246–1253.

[88] Nanstad, R. K., Tipping, P., Kalkhof, R., and Sokolov, M. A., "Irradiation and Post-Annealing Reirradiation Effects on Fracture Toughness of RPV Steel Heat JRQ," *The Effects of Radiation on Materials: 21st International Symposium, ASTM STP 1447*, edited by M. Grossbeck, T. Allen, R. Lott, and A. Kumar, ASTM International, West Conshohochen, PA, 2004, pp. 149–163.

[89] Kang, K. S. and Kupca, L., "Pressurized Thermal Sock in Nuclear Power Plants: Good Practices for Assessment," Tech. Rep. IAEA-TECDOC-1627, International Atomic Energy Agency, Vienna, Austria, 2010.

[90] Odette, G., Lomborzo, P. M., and Wullaert, R. A., "Relationship between irradiation hardening and embrittlement of pressure vessel steels," *Effects of Radiation on Materials: Twelfth International Symposium, ASTM STP 870*, edited by F. A. Garner and J. S. Perrin, American Society for Testing and Materials, Philadelphia, PA, 1985, pp. 840–860.

[91] Eason, E., Wright, J., and Odette, G., "Improved Embrittlement Correlations for Reactor Pressure Vessel Steels," Tech. Rep. NUREG/CR-6551, U.S. Nuclear Regulatory Committee, Washington, DC, 1998.

[92] Odette, G., "Neutron Irradiation Effects in Reactor Pressure Vessel Steels and Weldments," Tech. Rep. IAEA-IWG-LMNPP-98/3, Vienna, Austria, 1998.

[93] Russell, K. C. and Brown, L. M., "A dispersion strengthening model based on differeing elastic moduli applied to the iron-copper system," *Acta Materialia*, Vol. 20, 1972, pp. 969–974.

[94] Martin, J. W., *Micromechanisms of Particle-Hardened Alloys*, Cambridge University Press, 1980.

[95] "Title 10, Code of Federal Regulations, Parts 0 to 199," U.S. Government Printing Office, Jan. 1987.

[96] Eason, E., Wright, J., Nelson, E., Odette, G., and Mader, E. V., "Embrittlement recovery due to annealing of reactor pressure vessel steels," *Nuclear Engineering and Design*, Vol. 179, No. 3, Feb. 1998, pp. 257–265.

[97] Kuramoto, A., Toyama, T., Nagai, Y., Inoue, K., Nozawa, Y., Hasegawa, M., and Valo, M., "Microstructural changes in a Russian-type reactor weld material after neutron irradiation, post-irradiation annealing and re-irradiation studied by atom probe tomography and positron annihilation spectroscopy," *Acta Materialia*, Vol. 61, No. 14, Aug. 2013, pp. 5236–5246.

[98] Ulbricht, A., Altstadt, E., Bergner, F., Viehrig, H.-W., and Keiderling, U., "Small-angle neutron scattering investigation of as-irradiated, annealed and reirradiated reactor pressure vessel weld material of decommissioned reactor," *Journal of Nuclear Materials*, Vol. 416, No. 1-2, Sept. 2011, pp. 111–116.

[99] Pareige, P., Radiguet, B., Suvorov, A., Kozodaev, M., Krasikov, E., Zabusov, O., and Massoud, J. P., "Three-dimensional atom probe study of irradiated, annealed and re-irradiated VVER 440 weld metals," *Surface and Interface Analysis*, Vol. 36, No. 56, May 2004, pp. 581–584.

[100] Kobayashi, S., Kikuchi, H., Takahashi, S., Kamada, Y., Ara, K., Yamamoto, T., Klingensmith, D., and Odette, G., "Neutron irradiation effects on magnetic minor hysteresis loops in nuclear reactor pressure vessel steels," *Philosophical Magazine*, Vol. 88, No. 12, April 2008, pp. 1791–1800.

[101] Kobayashi, S., Yamamoto, T., Klingensmith, D., Odette, G., Kikuchi, H., and Kamada, Y., "Magnetic evaluation of irradiation hardening in A533B reactor pressure vessel steels: Magnetic hysteresis measurements and the model analysis," *Journal of Nuclear Materials*, Vol. 422, No. 1-3, March 2012, pp. 158–162.

[102] Stubbins, J. F., Shong, W.-J., Giacobbe, M., Ougouag, A. M., and Williams, J. G., "Pressure Vessel Steel Embrittlement Monitoring by Magnetic Properties Measurements," *Small Specimen Test Techniques Applied to Nuclear Reactor Vessel Thermal Annealing and Plant Life Extension, ASTM STP 1204*, edited by W. R. Corwin, F. M. Haggag, and W. L. Server, American Society for Testing and Materials, Philadelphia, PA, 1993, pp. 5–15.

[103] Devine, M. K., Jiles, D. C., Liaw, P. K., Rishel, R. D., and Drinon, D. S., "Magnetic property changes in various structural steels due to irradiation," *Review of Progress in Quantitative Nondestructive Evaluation*, edited by D. O. Thompson and D. E. Chimenti, Vol. 12, Plenum Press, New York, 1993, pp. 1815–1822.

[104] Park, D.-G., Hong, J.-H., Kim, I.-S., and Kim, H. C., "Evaluation of thermal recovery of neutron-irradiated SA508-3 steel using magnetic property measurements," *Journal of Materials Science*, Vol. 32, 1997, pp. 6141–6146.

[105] Park, D. G., Kim, C. G., Kim, H. C., Hong, J. H., and Kim, I. S., "Effect of neutron irradiation on magnetic properties in the low alloy Ni-Mo steel SA508-3," *Journal of Applied Physics*, Vol. 81, No. 8, 1997, pp. 4125.

[106] Niffenegger, M., Reichlin, K., and Kalkhof, D., "Application of the Seebeck effect for the monitoring of neutron embrittlement and low-cycle fatigue in nuclear reactor technology," *Transactions of the 17th International Conference on Structural Mechanics in Reactor Technology (SMiRT 17)*, Prague, Czech Republic, 2003, pp. 1–8.

[107] Acosta, B. and Sevini, F., "Evaluation of irradiation damage effect by applying electric properties based techniques," *Nuclear Engineering and Design*, Vol. 229, No. 2-3, April 2004, pp. 165–173.

[108] Etoh, J., Sagisaka, M., Matsunaga, T., Isobe, Y., Garner, F., Freyer, P., Huang, Y., Wiezorek, J., and Okita, T., "Development of a nondestructive inspection method for irradiation-induced microstructural evolution of thick 304 stainless steel blocks," *Journal of Nuclear Materials*, Vol. 440, No. 1-3, Sept. 2013, pp. 500–507.

[109] Phani, K., Sanyal, D., and a.K. Sengupta, "Estimation of elastic properties of nuclear fuel material using longitudinal ultrasonic velocity A new approach," *Journal of Nuclear Materials*, Vol. 366, No. 1-2, June 2007, pp. 129–136.

[110] Hiser, A. L. and R. E. Green, "Preliminary results on ultrasonic attenuation detection of neutron irradiation embrittlement of nuclear reactor steel," *Material Research Society Symposium*, Vol. 503, Materials Research Society, 1998, pp. 175–182.

[111] Hiser, A. L., "Toughness and embrittlement of RPV steels using ultrasonic measurements," *Proceedings of ICONE12, 12th International Conference on Nuclear Engineering*, ASME, 2004, pp. 29–38.

[112] Daw, J., Tittmann, B., Reinhardt, B., Kohse, G., Ramuhalli, P., Montgomery, R., Chien, H.-t., Villard, J.-f., Palmer, J., Rempe, J., Montgomery, R., Chien, H.-T., Villard, J.-F., Palmer, J., and Rempe, J., "Irradiation Testing of Ultrasonic Transducers Irradiation Testing of Ultrasonic Transducers," *2013 Conference on Advancements in Nuclear Instrumentation, Measurements Methods (ANIMMA 2013)*, Vol. June 23-27, Idaho National Laboratory, Marseille, France, 2013.

[113] Wirth, B. D., Odette, G., Maroudas, D., and Lucas, G. E., "Dislocation loop structure , energy and mobility of self-interstitial atom clusters in bcc iron," *Journal of Nuclear Materials*, Vol. 276, 2000, pp. 33–40.

[114] Qu, J. and Cherkaoui, M., *Fundamentals of Micromechanics of Solids*, John Wiley & Sons, Inc., Hoboken, NJ, 2006.

[115] Matlack, K. H., Kim, J.-Y., Wall, J. J., Qu, J., Jacobs, L. J., and Sokolov, M. A., "Sensitivity of ultrasonic nonlinearity to irradiated, annealed, and re-irradiated microstructure changes in RPV steels," *Journal of Nuclear Materials*, Vol. 448, 2014, pp. 26–32.

[116] Liu, C., Odette, G., Wirth, B. D., and Lucas, G. E., "A lattice Monte Carlo structures in irradiated simulation pressure of nanophase compositions and vessel Fe-Cu-Ni-Mn-Si steels," *Materials Science and Engineering: A*, Vol. 238, 1997, pp. 202–209.

[117] Breazeale, M. A. and Philip, J., "Determination of third-order elastic constants from ultrasonic harmonic generation measurements," *Physical Acoustics Volume XVII*, edited by W. P. Mason and R. N. Thurston, Academic Press, New York, vol. 17 ed., 1984, pp. 1–60.

[118] Adler, E. L., Bridoux, E., Coussot, G., and Dieulesaint, E., "Harmonic Generation of Acoustic Surface Waves in Bi12GeO20 and LiNbO3," *IEEE Transactions on Sonics and Ultrasonics*, Vol. 20, No. 1, 1973, pp. 13–16.

[119] Hurley, D. C., "Nonlinear propagation of narrow-band Rayleigh waves excited by a comb transducer," *Journal of the Acoustical Society of America*, Vol. 106, No. 4, 1999, pp. 1782–1788.

[120] Barnard, D. J., Brasche, L. J. H., Raulerson, D., and Degtyar, A. D., "Monitoring Fatigue Damage Accumulation with Rayleigh Wave Harmonic Generation Measurements," *Review of Progress in Quantitative Nondestructive Evaluation*, edited by D. O. Thompson and D. E. Chimenti, Vol. 22, AIP, New York, 2003, pp. 1393–1400.

[121] Bermes, C., Kim, J.-Y., Qu, J., and Jacobs, L. J., "Experimental characterization of material nonlinearity using Lamb waves," *Applied Physics Letters*, Vol. 90, No. 2, 2007, pp. 021901.

[122] Matlack, K. H., Kim, J.-Y., Jacobs, L. J., and Qu, J., "Experimental characterization of efficient second harmonic generation of Lamb wave modes in a nonlinear elastic isotropic plate," *Journal of Applied Physics*, Vol. 109, No. 1, 2011, pp. 014905.

[123] Hurley, D. C. and Fortunko, C. M., "Determination of the nonlinear ultrasonic parameter β using a Michelson interferometer," *Measurement Science Technology*, Vol. 8, 1997, pp. 634–642.

[124] Sun, L., Kulkarni, S. S., Achenbach, J. D., and Krishnaswamy, S., "Technique to minimize couplant-effect in acoustic nonlinearity measurements," *The Journal of the Acoustical Society of America*, Vol. 120, No. 5, 2006, pp. 2500–2505.

[125] Dace, G. E., Thompson, R. B., and Buck, O., "Measurement of the acoustic harmonic generation for materials characterization using contact transducers," *Review of Progress in Quantitative Nondestructive Evaluation*, edited by D. Thompson and D. E. Chimenti, Vol. 11, Plenium Press, New York, 1992, pp. 2069–2076.

[126] Ogi, H., Hirao, M., and Aoki, S., "Noncontact monitoring of surface-wave nonlinearity for predicting the remaining life of fatigued steels," *Journal of Applied Physics*, Vol. 90, No. 1, 2001, pp. 438–442.

[127] Müller, M. F., Kim, J.-Y., Qu, J., and Jacobs, L. J., "Characteristics of second harmonic generation of Lamb waves in nonlinear elastic plates." *The Journal of the Acoustical Society of America*, Vol. 127, No. 4, April 2010, pp. 2141–52.

[128] Matlack, K. H., Wall, J. J., Kim, J.-Y., Qu, J., and Jacobs, L. J., "Nonlinear Ultrasound to Monitor Radiation Damage in Structural Steel," *6th European Workshop on Structural Health Monitoring*, 2012, pp. 1–8.

[129] Matlack, K. H., Wall, J. J., Kim, J.-Y., Qu, J., Jacobs, L. J., and Viehrig, H.-W., "Evaluation of radiation damage using nonlinear ultrasound," *Journal of Applied Physics*, Vol. 111, No. 5, 2012, pp. 054911.

[130] Rogers, P. H. and Van Buren, A. L., "An exact expression for the Lommel diffraction correction integral," *Journal of the Acoustical Society of America*, Vol. 55, No. 4, 1974, pp. 724–728.

[131] Shull, D. J., Kim, E. E., Hamilton, M. F., and Zabolotskaya, E. A., "Diffraction effects in nonlinear Rayleigh wave beams," *Journal of the Acoustical Society of America*, Vol. 97, No. 4, 1995, pp. 2126–2137.

[132] Ingenito, F. and Williams, A. O., "Calculation of second-harmonic generation in a piston beam," *Journal of the Acoustical Society of America*, Vol. 49, 1971, pp. 319–328.

[133] Thiele, S., Kim, J.-y., Qu, J., and Jacobs, L. J., "Air-Coupled Detection of Nonlinear Rayleigh Surface Waves to Assess Material Nonlinearity," *Ultrasonics*, 2013.

[134] Lara, N. O., Ruiz, A., Rubio, C., Ambriz, R. R., and Medina, A., "Nondestructive assessing of the aging effects in 2205 duplex stainless steel using thermoelectric power," *NDT & E International*, Vol. 44, No. 5, Sept. 2011, pp. 463–468.

[135] Rana, R., Singh, S., and Mohanty, O., "Thermoelectric power studies of copper precipitation in a new interstitial-free steel," *Scripta Materialia*, Vol. 55, No. 12, Dec. 2006, pp. 1107–1110.

[136] Hu, J. and Nagy, P. B., "On the role of interface imperfections in thermoelectric nondestructive materials characterization," *Applied Physics Letters*, Vol. 73, No. 4, 1998, pp. 467.

[137] Worrall, G., Buswell, J., English, C., Hetherington, M., and Smith, G., "A study of the precipitation of copper particles in a ferrite matrix," *Journal of Nuclear Materials*, Vol. 148, No. 1, March 1987, pp. 107–114.

[138] Nagai, Y., Hasegawa, M., Tang, Z., Hempel, a., Yubuta, K., Shimamura, T., Kawazoe, Y., Kawai, a., and Kano, F., "Positron confinement in ultrafine embedded particles: Quantum-dot-like state in an Fe-Cu alloy," *Physical Review B*, Vol. 61, No. 10, March 2000, pp. 6574–6578.

[139] He, S. M., van Dijk, N. H., Paladugu, M., Schut, H., Kohlbrecher, J., Tichelaar, F. D., and van der Zwaag, S., "In situ determination of aging precipitation in deformed Fe-Cu and Fe-Cu-B-N alloys by time-resolved small-angle neutron scattering," *Physical Review B*, Vol. 82, No. 17, Nov. 2010, pp. 174111.

[140] Deschamps, A., Militzer, M., and Poole, W. J., "Precipitation Kinetics and Strengthening of a Fe0. 8wt%Cu Alloy," *ISIJ International*, Vol. 41, No. 2, 2001, pp. 196–205.

[141] Nagai, Y., Tang, Z., and Hasegawa, M., "Chemical analysis of precipitates in metallic alloys using coincidence Doppler broadening of positron annihilation radiation," *Radiation Physics and Chemistry*, Vol. 58, No. 5-6, June 2000, pp. 737–742.

[142] Park, D.-G., Ryu, K. S., Kobayashi, S., Takahashi, S., and Cheong, Y. M., "Change in magnetic properties of a cold rolled and thermally aged FeCu alloy," *Journal of Applied Physics*, Vol. 107, No. 9, 2010, pp. 09A330.

[143] Deschamps, A., Militzer, M., and Poole, W. J., "Comparison of Precipitation Kinetics and Strengthening in an Fe-0.8%Cu Alloy and a 0.8% Cu-containing Low-carbon Steel," *ISIJ International*, Vol. 43, No. 11, 2003, pp. 1826–1832.

[144] Osamura, K., Okuda, H., Asano, K., Furusaka, M., Kishida, K., Kurosawa, F., and Uemori, R., "SANS study of phase decomposition in Fe-Cu Alloy with Ni and Mn addition," *ISIJ International*, Vol. 34, No. 4, 1994, pp. 346–354.

[145] Perez, M., Perrard, F., Massardier, V., Kleber, X., Deschamps, a., de Monestrol, H., Pareige, P., and Covarel, G., "Low-temperature solubility of copper in iron: experimental study using thermoelectric power, small angle X-ray scattering and tomographic atom probe," *Philosophical Magazine*, Vol. 85, No. 20, July 2005, pp. 2197–2210.

[146] Christien, F., Telling, M., and Knight, K., "Neutron diffraction in situ monitoring of the dislocation density during martensitic transformation in a stainless steel," *Scripta Materialia*, Vol. 68, No. 7, April 2013, pp. 506–509.

[147] Bhattacharya, D., Jayakumar, T., Moorthy, V., Vaidyanathan, S., and Raj, B., "Characterization of microstructures in 17-4-PH stainless steel by magnetic Barkhausen noise analysis," *NDT & E International*, Vol. 26, No. 3, June 1993, pp. 141–148.

[148] Murayama, M., Katayama, Y., and Hono, K., "Microstructural Evolution in a 17-4 PH Stainless Steel after Aging at 400C," *Metallurgical and Materials Transactions A*, Vol. 30A, 1999, pp. 345–353.

[149] Viswanathan, U. K., Nayar, P. K. K., and Krishnan, R., "Kinetics of precipitation in 17-4 PH stainless steel," *Materials Science and Technology*, Vol. 5, No. April, 1989, pp. 346–349.

[150] Hsiao, C. N., Chiou, C. S., and Yang, J. R., "Aging reactions in a 17-4 PH stainless steel," *Materials Chemistry and Physics*, Vol. 74, No. 2, March 2002, pp. 134–142.

[151] Mirzadeh, H. and Najafizadeh, a., "Aging kinetics of 17-4 PH stainless steel," *Materials Chemistry and Physics*, Vol. 116, No. 1, July 2009, pp. 119–124.

[152] Ping, D., Ohnuma, M., Hirakawa, Y., Kadoya, Y., and Hono, K., "Microstructural evolution in 13Cr8Ni2.5Mo2Al martensitic precipitation-hardened stainless steel," *Materials Science and Engineering: A*, Vol. 394, No. 1-2, March 2005, pp. 285–295.

[153] IAEA, "Integrity of reactor pressure vessels in nuclear power plants: assessment of irradiation embrittlement effects in reactor pressure vessel steels," Tech. Rep. IAEA NUCLEAR ENERGY SERIES No. NP-T-3.11, Vienna, Austria, 2009.

[154] Krawitz, A. D., *Introduction to Diffraction in Materials Science and Engineering*, John Wiley & Sons, New York, NY, 2001.

[155] Ribárik, G., *Modeling of diffraction patterns properties*, Ph.d. thesis, Eötvös University, Budapest, 2008.

[156] Stoller, R. E., "Modeling the influence of irradiation temperature and displacement rate on hardening due to point defect clusters in ferritic steels," *Effects of Radiation on Materials: 16th International Symposium, ASTM STP1175*, edited by A. S. Kumar, D. S. Gelles, R. K. Nanstad, and E. A. Little, ASTM International, Philadelphia, PA, 1993, pp. 394–423.

[157] Schmauder, S. and Binkele, P., "Atomistic computer simulation of the formation of Cu-precipitates in steels," *Computational Materials Science*, Vol. 24, No. 1-2, May 2002, pp. 42–53.

[158] Bacon, D. J. and Osetsky, Y., "Mechanisms of hardening due to copper precipitates in α-iron," *Philosophical Magazine*, Vol. 89, No. 34-36, Dec. 2009, pp. 3333–3349.

[159] "The Generation IV International Forum: Generation IV Systems," Available Online: https://www.gen-4.org/gif/jcms/c_40465/generation-iv-systems [Accessed Feb. 7, 2014], 2014.

[160] Buck, O., Morris, W. L., and Richardson, J. M., "Acoustic harmonic generation at unbonded interfaces and fatigue cracks," *Applied Physics Letters*, Vol. 33, No. 5, 1978, pp. 371–373.

[161] Treiber, M., Kim, J.-Y., Jacobs, L. J., and Qu, J., "Correction for partial reflection in ultrasonic attenuation measurements using contact transducers," *The Journal of the Acoustical Society of America*, Vol. 125, No. 5, May 2009, pp. 2946–53.